UiO : Department of Geosciences
University of Oslo

Marine Vibrators: Synthetic Data Study

Sander Wågønes Losnedahl

Master's Thesis, Spring 2019

Abstract

The traditional airgun source has for a long time been the preferred type of source in marine seismic data acquisition due to its high impulsive pressure output. However, this impulsive energy has recently been of concern with regards to the health of marine life. Therefore, restrictions have been put in place such that airgun surveying is prohibited in areas where marine life may be sensitive to high pressure levels. An example of such an area is the Great Australian Bight where seismic survey applications have been rejected several times. Another example is the Lofoten area located on the coast in the northern part of Norway facing the Norwegian Sea. Seismic exploration is not allowed in this area because of the concern that the pressure created from the seismic airgun may harm the fisheries which is the main industry of the region. An alternative seismic source is the marine vibrator which aims to spread the pressure output over time thus creating a non-impulsive wavefield that is not as harmful to marine life. The output of such a source is more manageable than that of the airgun and the generation of low-frequencies without bubble pulse contamination is an additional benefit. These are the motivations behind the revival of the marine vibrator. This thesis work will first derive the fundamental equations describing such a non-impulsive wavefield generated by a marine vibrator. Furthermore, this thesis work will investigate what happens when motion is introduced into the non-impulsive source wavefield by deriving the aforementioned equations with respect to motion. These equations represents the source signature of a marine vibrator and will be used to generate synthetic data. Further processing and imaging will be employed in an attempt to better isolate the effects of motion on the data and the limits of resolution of the marine vibrator source will be investigated. Finally, controlled marine vibrator data will be compared with corresponding airgun data in order to establish the validity of the marine vibrator.

Contents

Acknowledgements

I would like to extend my sincere appreciation to Prof. Leiv-J. Gelius, Dr. Okwudili Orji, Dr. Walter Söllner and Dr. Endrias Asgedom for their excellent supervision and support during the making of this master's thesis. A special thanks is given to PGS, Oslo office for their support and hospitality to me as a student as well as their generous sharing of resources and software.

Chapter 1

Introduction

1.1 A brief history of seismic sources

The first successful attempts of seismic exploration started in the early 1920s. No developed seismic source existed at that time so the scientist had to employ explosive charges both for land and marine surveys. These explosives created an impulsive seismic wavelet perfect for basic reflection seismic and additionally, were relatively easy to handle.
However, the explosive charges had a severe flaw regarding bubble pulses in marine surveys since no digital filtering were available at that time. The solution was to detonate the explosives at very shallow depths to avoid the bubble pulses entirely which resulted in loosing much of the impulsive energy.
Early versions of the airgun and seismic vibrator were developed in the 1950s and 1960s and they soon outperformed the explosive charges in both quality and cost. It seemed that the airgun was preferred over the vibrator as it resembled the old explosive charge where the technology was already available. A typical airgun is shown in figure 1.1 (top) and the output from multiple airguns (airgun array) are shown in figure 1.1 (bottom).

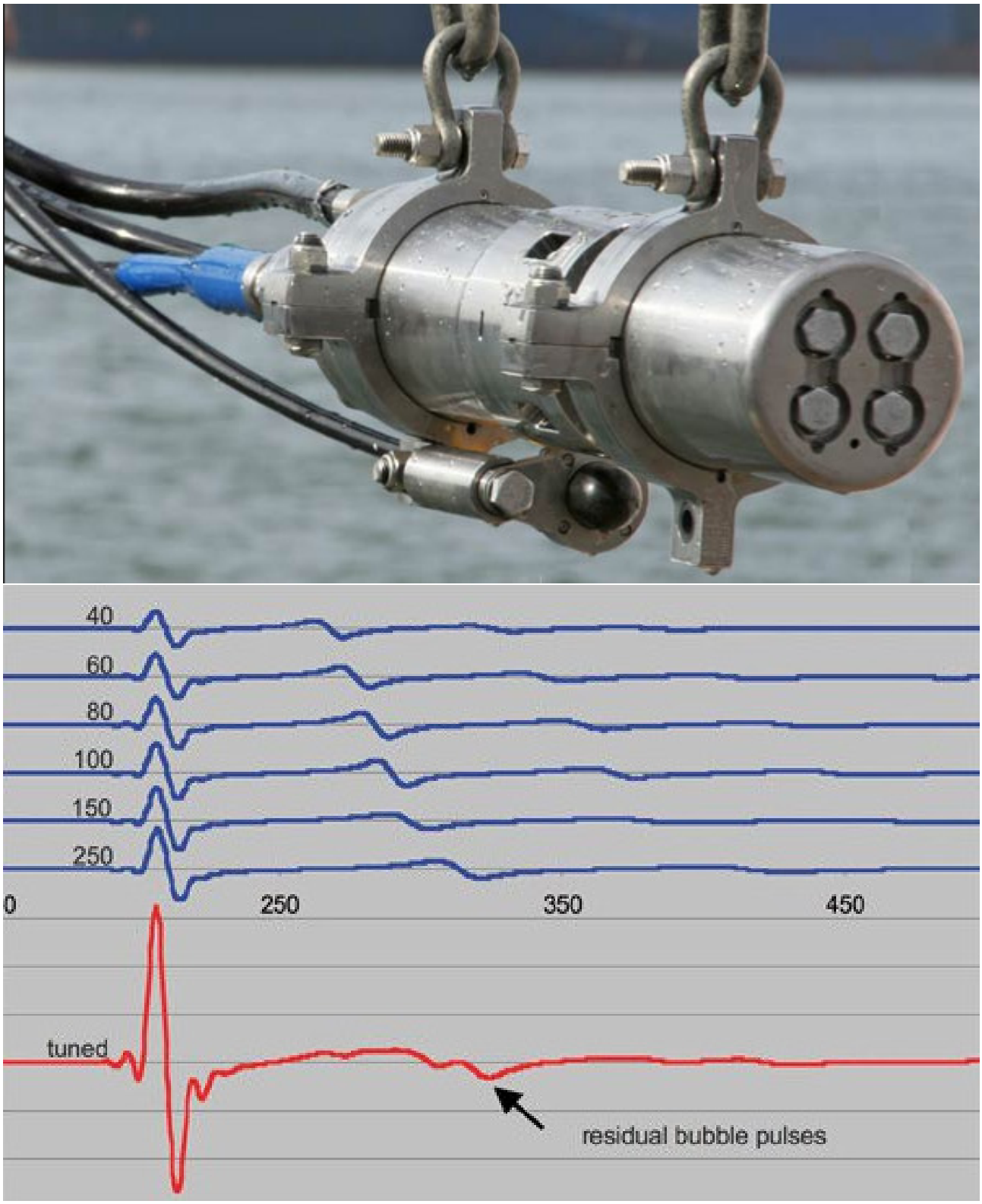

Figure 1.1: Example of what an airgun could look like (top) and what the output from multiple airguns could look like (bottom) (Emma Technologies) (Western Geco, 2010).

Basically, an airgun is a container with a fixed volume V able to hold overpressured air P which is released almost instantaneously creating an impulsive pressure wave in the

surrounding acoustic medium. As in the case of the explosive charge, the airgun creates a bubble that oscillates with a period T and is described by the modified Rayleigh-Willis formula (Parkes & Hatton, 1986)

$$T = k\frac{P^{\frac{1}{3}}V^{\frac{1}{3}}}{P_{hyd}^{\frac{5}{6}}} \qquad (1.1)$$
$$P_{hyd} = P_{atm} + \rho g D$$

where k is a unit dependent constant, ρ is the density of water, g is the gravitational constant, P_{hyd} is the hydro-static pressure from the overlying water column with P_{atm} being the atmospheric pressure and D the depth of the airgun. From equation 1.1, one may alternatively solve for the frequency f. Taking the inverse of equation 1.1 yields a term for the frequency ($f = 1/T$)

$$f = \frac{P_{hyd}^{\frac{5}{6}}}{kP^{\frac{1}{3}}V^{\frac{1}{3}}} \qquad (1.2)$$

Equation 1.2 shows that more low frequencies are created when the volume of the container and/or the pressure output from the container increases. To obtain frequencies within the seismic bandwidth ($< 500Hz$), one typically adjusts the pressure within the container since increasing the volume itself is not very cost efficient. Increasing the contained pressure increases the strength of the signal and consequently the signal to noise ratio (S/N). This is because the power of the ambient noise stays the same while the power of the signal increases. These bubble pulses are expanding and collapsing in a low frequency fashion creating low frequency radiation. This low-frequency radiation causes notches in the low-frequency part of the airgun source signature. Therefore, many airguns of different variations and depths are often clustered together in an attempt to remove the effects of the bubble pulse and to increase the strength of the impulse. However, the notches created from the bubble are not completely removed and still influence the low-frequency part of the airgun source signature (Landrø & Amundsen, 2014). The low frequencies are in many cases discarded when processing seismic data.

1.2 Airguns and the environment

The pressure wave emitted from a typical airgun array may damage the environment, especially the health of marine mammals (International Association of Geophysical Contractors, 2002). Some mammals, particularly large baleen whales, may suffer auditory damage by lower frequencies within the seismic bandwidth ($< 900Hz$). These mammals, having adapted their hearing to such low frequencies, may suffer both temporary and permanent hearing damage since much of the seismic energy typically lies below 500Hz. (International Association of Geophysical Contractors, 2002).

For a large baleen whale to suffer any hearing damage from a seismic vessel, it would have to stay within a 20° cone of a marine airgun source (the optimal angle of pressure emission) for a longer period of time, which is unlikely (International Association of Geophysical Contractors, 2002).

What pressure levels cause hearing damage are very species specific so if a pressure level is damaging to one species, it can not be extrapolated to another (International Association of Geophysical Contractors, 2002). It is noteworthy that the science behind most of marine mammal hearing are just extrapolation of terrestrial mammal hearing (International Association of Geophysical Contractors, 2002).

Marine mammals that suffer permanent or even temporary hearing damage from an airgun array source may change their behavioral patterns. This may change how these marine mammals breed and may over a longer period of time harm the species population. The science is very limited in this field of study, but political precautions are likely to be taken if marine seismic acquisition is to take place in areas where some marine mammal populations can be scarce or vulnerable.

1.3 Marine seismic vibrators

This thesis will focus on one type of environmentally friendly marine seismic source, the marine seismic vibrator, and more specifically, the modular marine vibrator which consists of vibrating plates emitting a pressure wave within a certain bandwidth. Unlike the

airgun, a seismic vibrator does not create an impulse, but aims to emit a signal with the same energy as an airgun array but spread over a longer period of time. Usually the frequency vary over the interval of emission, known as a sweep. There are three highly advantageous aspects of the marine vibrator:

1. The release of energy is much more manageable due to full control over the rate of vibration of the plates.

2. Lower peak source strength due to the spread of energy over time, lowering the risk of potentially damaging marine mammals.

3. It is possible to reach very low frequencies $(2 - 6Hz)$ which is useful in several types of inversions.

Both the amount of energy released and the direction of release can be controlled to a high degree. The direction of emission is called directivity and is achieved by having several different vibrating plates lined up and controlled in such a way that they would constructively interfere in the vertical direction, and destructively interfere in the radial direction.

Land surveys have been utilizing vibrator sources for a long time, but adapting the technology to marine surveys has proven to be a difficult task. One problem is the difference in how the surveys are typically executed. Source and receivers in a land survey are placed on the surface (figure 1.2), effectively removing all ghosts from the signal. In a marine survey however, both the source and receivers are usually placed beneath the sea surface giving rise to source and receiver ghosts. These ghosts are further amplified due to the high reflection coefficients of the water/air interface (sea surface) and the sea bottom.

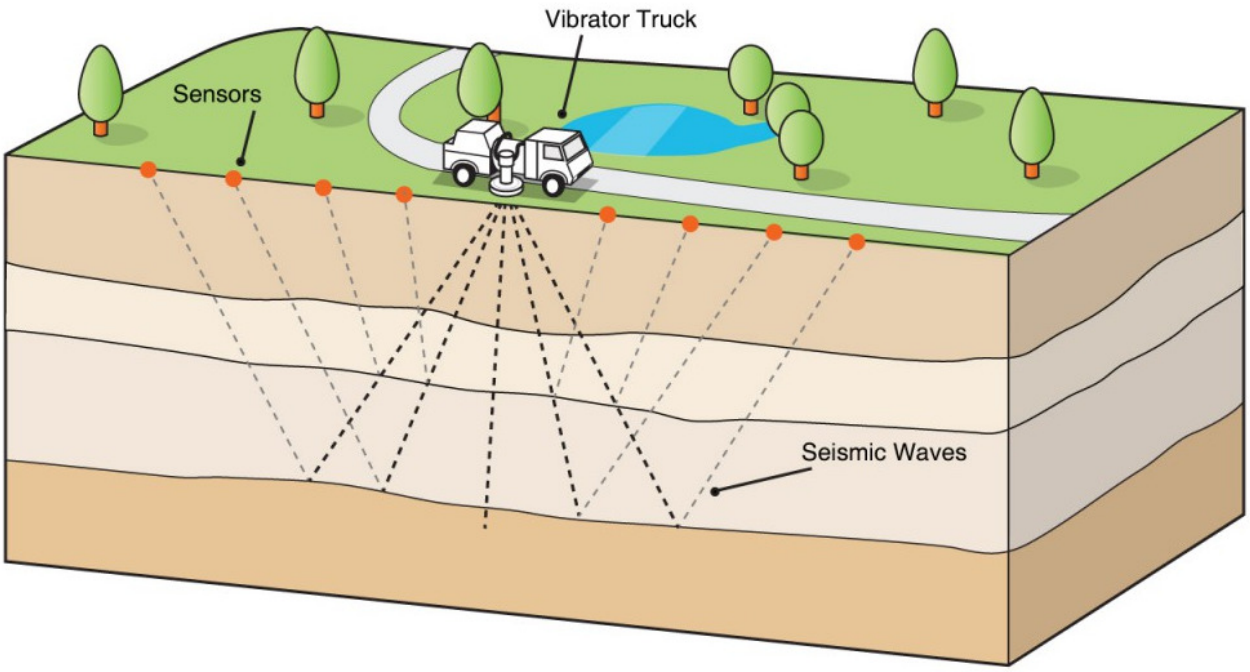

Figure 1.2: Land survey where the vibrating source is attached to a truck. Receivers are placed in a line with equal spacing away from the truck (Innoseis, 2018).

Another difference is that both the source and receivers are towed behind a ship in a marine survey. In a land survey, both the source and receivers are stationary during recording (figure 1.2). A moving receiver distorts the measurement, but a moving source distorts the wave field itself (Hampson & Jakubowicz, 1995). Vibrating sources in motion causes a phase shift of the wavefield due to the Doppler effect. In addition to a phase shift, the moving source also slants the signal which must be corrected for (Hampson & Jakubowicz, 1995). These effects will be investigated further in this work.

A large advantage of having moving source and receivers is that the survey can cover a larger area within a given time compared to a land survey. In addition, the truck can not access areas with a difficult terrain, meaning other methods of acquisition must be used. This will never be a problem in marine acquisition since there is no terrain to consider.

Many companies have seen the potential of the seismic marine vibrator and are currently developing various kinds of vibrators. Examples of such companies are PGS, Western Geco, CGG and BP. Some companies have joined forces to investigate the feasability of

the marine vibrator source. An example of this would be the MV-JIP (Marine Vibrator Joint Industry Program) which is sponsored by Shell, Exxon and Total.

1.4 MV-IPN

The MV-JIP, or Marine Vibrator Joint Industry Program, is a collaborative effort supported by Shell, Exxon and Total and aims to develop a market competitive and environmentally friendly seismic marine vibrator source for both commercial and military use. The MV-JIP has developed multiple vibrator sources, but only the MV-IPN (Marine Vibrator Integrated Projector Node) will be covered in this thesis.

The MV-IPN uses magnetic fluxes created by electrical currents to rapidly drive pistons back and forth creating displacements in the surrounding medium (Roy et. al., 2018). The vibrator is shown in figure 1.3.

Figure 1.3: The MV-IPN in full power testing (Feltham et. al., 2018).

There are three main housings in the vibrator as can be seen from figure 1.3. The left housing holds all power control equipment, the middle housing holds the actual transducer (the circle in figure 1.3) and the right housing holds the pressure compensation system and control and monitoring equipment (Feltham et. al., 2018). During a test, this particular transducer is able to emit a spectral density level shown in figure 1.4

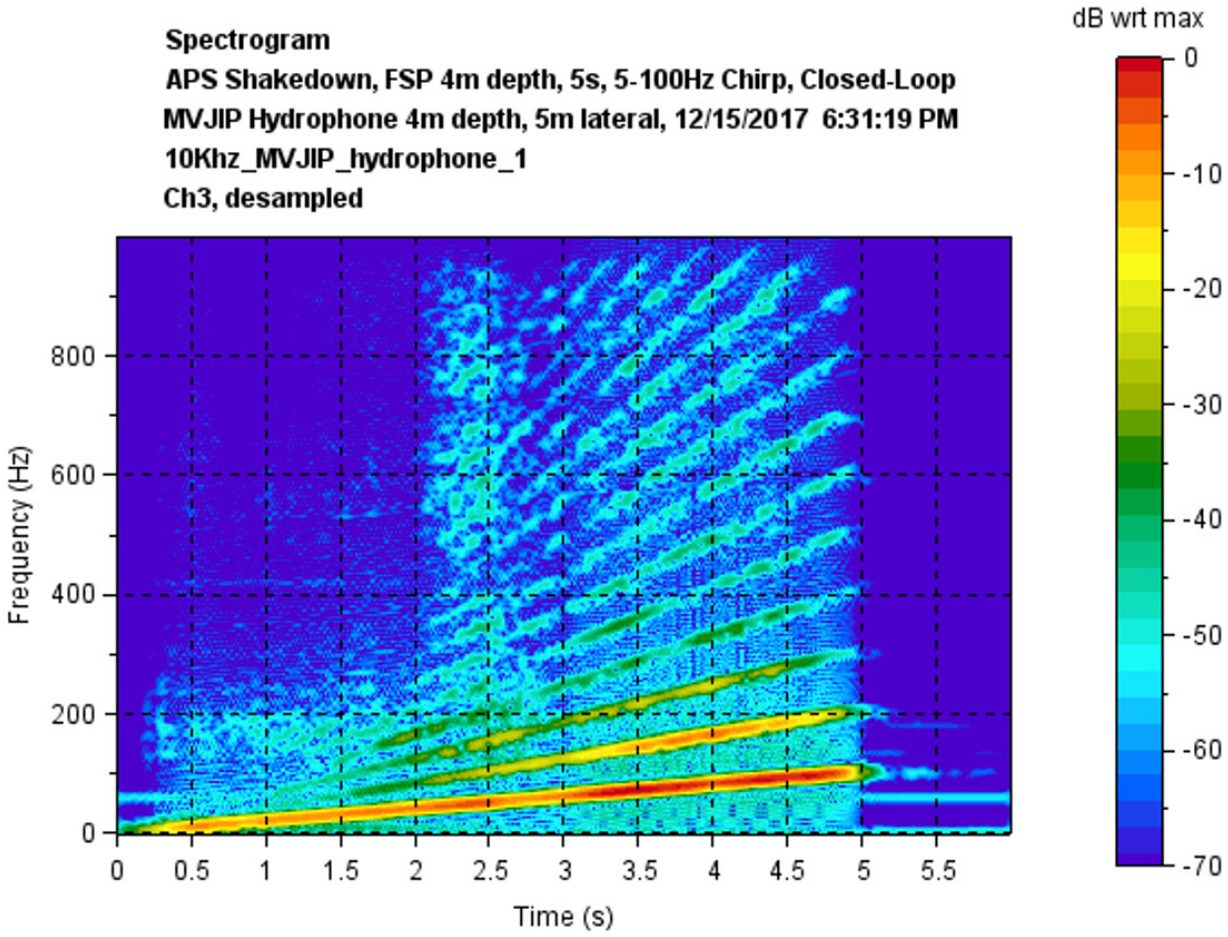

Figure 1.4: Decibel spectrogram of the MV-IPN during testing of sweep from $5-100Hz$ over 5 seconds (Feltham et. al., 2018).

Figure 1.4 shows that harmonic frequencies are occurring. This was later found out to be caused by the spring resonance which should be corrected for before a new test takes place (Feltham et. al., 2018).

These decibel levels proved sufficient for the MV-JIP ($190dB$ re. $1\mu PA/Hz$ @ $1m$ for $5-10Hz$ and $200dB$ re. $1\mu Pa/Hz$ @ $1m$ for $10-100Hz$) to declare the test a success and that the MV-IPN is ready for seismic testing. Such testing is estimated to proceed in 2019 (Feltham et. al., 2018).

1.5 PGS' marine vibrator

PGS is currently working on two different concepts of a seismic marine vibrator. The first one being the Flextensional Marine Vibrator (left in figure 1.5). This type of vibrator

utilizes electric drivers and magnets to oscillate a spring that makes a fiberglass plate vibrate and cause displacements in the surrounding medium. Two of these vibrators are often paired together so that the amplitude output is uniform within $5 - 100Hz$ (PGS, 2017).

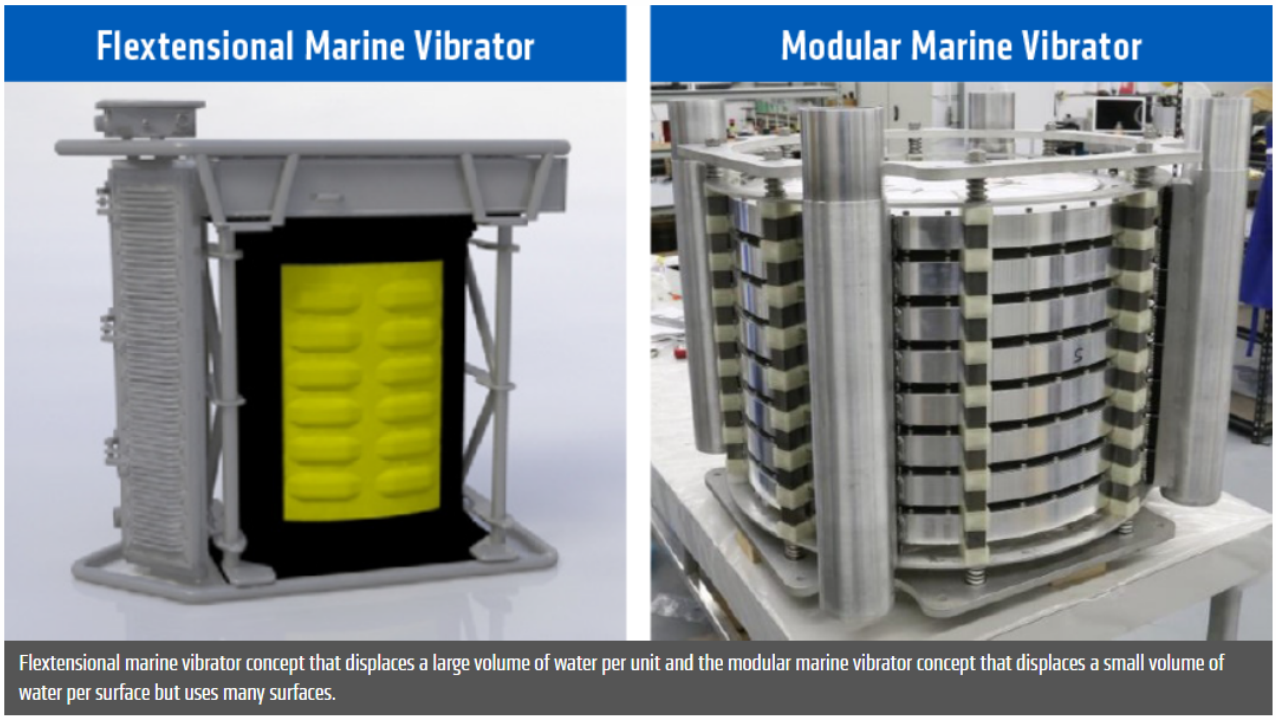

Figure 1.5: The two types of vibrators currently under development at PGS (PGS, 2017).

The second type of marine vibrator is called a Modular Marine Vibrator that also utilizes electrical drivers to move small cylindrical plates (to the right in figure 1.5) to create displacements in the surrounding water. These plates have a smaller surface area than the Flextensional Marine Vibrator, but multiple plates stacked together are able to cause sufficient displacements in the water (PGS, 2017).

1.6 Geokinetics' marine vibrator

Similar to PGS, Geokinetics are also developing a Flextensional marine vibrator called AquaVib. The main advantage of the AquaVib is that the vibrator is tuned for shallow marine acquisition. The vibrator can be placed as shallow as $1m$ below the sea surface while still maintaining its output signal. Shallow waters tend to have fragile ecosystems

which an airgun source may harm. The size of the AquaVib is drastically smaller than any airgun on the market today, making them easier to handle from a logistical point of view (Archer, 2017).

Figure 1.6: The AquaVib in action (Archer, 2017).

Compared to many other marine seismic vibrators, the AquaVib is ready for production and has already entered the market (Archer, 2017). Figure 1.6 gives an overview of the AquaVib in action.

1.7 Previous work in source wavefield modeling and synthetic data generation

Synthetic data generation using a marine vibrator source has previously been done with different models and survey configurations. An example would be the synthetic data

generated by Hampson & Jakubowicz (1995) which consisted of a single diffractor in a medium with constant velocity (Hampson & Jakubowicz, 1995). This article demonstrated what the effects of motion would be on a continuous vibroseis signal and the recorded data using the described model. Hampson & Jakubowicz also presents a method of compensating for such effects. Additionally, the article shows the synthetic data after the appropriate corrections have been made. However, that article does not introduce the modeling of the source signature used in generating the synthetic data.

On the other hand, Kramer et al. (1969) proposed a method of calculating the output from a marine vibrator source using Bernoulli's equation (Kramer et al., 1969). Walker et al. (1996) used this proposed equation to drive a marine vibrator in a real field test which yielded good results (Walker et al., 1996). However, this article did not isolate effects that are native to the marine vibrator.

This thesis will attempt to derive the fundamental equations describing the source signature of a marine vibrator and will use these equations in order to model synthetic data. The source wavefield modeling has of this thesis work was accepted as an extended abstract to the SEG2019 annual meeting. Furthermore, the effects native to a marine vibrator with or without motion will be isolated in order to investigate the feasibility of such a vibrating source.

Chapter 2

Pressure Output from a Marine Seismic Vibrator - Theoretical Model

To model the pressure field generated from a marine seismic vibrator, the motions of the medium have to be derived for an isotropic, non-viscous fluid. The combination of Euler's equation of motion and the constitutive law describe the reaction of an acoustic medium when a wave propagates through. These two equations can then be used to derive the representation theorem which compares two pressure fields within a volume. Through the representation theorem, the far field (also near field) can be found.

2.1 Euler's equation of motion

Euler's equation of motion of an infinitesimal fluid volume can be derived using Newton's second law, or in other words, conservation of momentum. This law states that the total momentum of a closed system ($m\mathbf{v}$) with no external or internal force is preserved regardless of how complicated the system is. If one assumes that (i) pressure gradients are the driving forces and (ii) the convection term can be neglected, the linearized equation of motion takes the form

$$\bigtriangledown p = \rho \frac{\partial \mathbf{v}}{\partial t} \tag{2.1}$$

with p being the pressure, ρ is the density of the medium and $\mathbf{v}$ is the particle velocity. For a complete derivation of the linearized Euler's equation of motion, the reader is referred to Appendices A and B.

2.2 Conservation of mass

Consider again a small infinitesimal fluid volume, but this time apply the consitutive law describing mass balance when a pressure wave propagates through the medium.

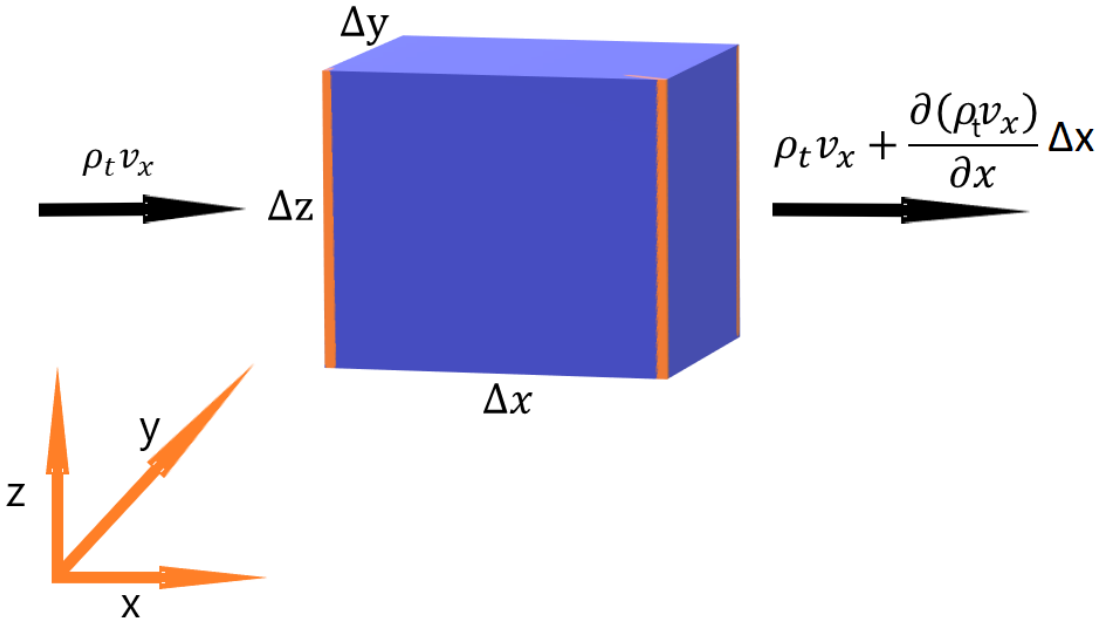

Figure 2.1: Rate of mass flow into and out of the volume in the x-direction.

The volume of this infinitesimal fluid element is $\Delta V = \Delta x \Delta y \Delta z$ and the particle velocity is denoted $\mathbf{v} = \{v_x, v_y, v_z\}$. From figure 2.1 it follows that the net influx of mass resulting from flow in the x-direction is (ρ_t being the total density)

$$[\rho_t v_x - (\rho_t v_x + \frac{\partial(\rho_t v_x)}{\partial x}\Delta x)]\Delta y \Delta z = -\frac{\partial(\rho_t v_x)}{\partial x}\Delta V \tag{2.2}$$

Similar expressions give the net influx for the y and z directions, so that the total influx must be

$$-[\frac{\partial(\rho_t v_x)}{\partial x} + \frac{\partial(\rho_t v_y)}{\partial y} + \frac{\partial(\rho_t v_z)}{\partial z}]\Delta V = - \bigtriangledown \cdot(\rho_t \mathbf{v})\Delta V \tag{2.3}$$

The rate at which the mass increases in the volume can be written formally as

$$[(\frac{\partial \rho_t}{\partial t})\Delta V + \rho_t Q \Delta V] \tag{2.4}$$

where the second term represents an injection term (Q being injected volume flow per unit volume). The net influx must equal the rate of increase

$$\frac{\partial \rho_t}{\partial t} + \bigtriangledown \cdot (\rho_t \mathbf{v}) = -\rho_t Q \tag{2.5}$$

Equation 2.5 can be further expanded to obtain

$$\frac{1}{\rho_t}\frac{\partial \rho_t}{\partial t} + \frac{1}{\rho_t}(\mathbf{v} \cdot \bigtriangledown)\rho_t + \bigtriangledown \cdot \mathbf{v} = -Q \tag{2.6}$$

where the identity $\bigtriangledown \cdot (\rho_t \mathbf{v}) = \rho_t(\bigtriangledown \cdot \mathbf{v}) + \mathbf{v} \cdot \bigtriangledown \rho_t$ has been applied (Salby, 2012). Let ρ_0 represent the equilibrium density (no wave interaction). Then the perturbed density ρ follows from the equation

$$\rho_t = \rho_0 + \rho \tag{2.7}$$

Combination of equations 2.6 and 2.7 gives

$$\frac{1}{\rho_t}\frac{\partial \rho}{\partial t} + \frac{1}{\rho_t}(\mathbf{v} \cdot \bigtriangledown)\rho + \bigtriangledown \cdot \mathbf{v} = -Q \tag{2.8}$$

Assume now a linear relationship between the perturbed density and the wave pressure expressed as $d\rho = \frac{1}{c^2}dp$. Substitution of this expression in equation 2.8 leads to

$$\frac{1}{K}[\frac{\partial p}{\partial t} + (\mathbf{v} \cdot \bigtriangledown)p] + \bigtriangledown \cdot \mathbf{v} = -Q \tag{2.9}$$

with $K = \rho_t c^2$ being the bulk modulus.

In case of the seismic wave, it is demonstrated in Appendix B that equation 2.9 can be further approximated to give its final version

$$\frac{\partial p}{\partial t} = -K \bigtriangledown \cdot \mathbf{v} - KQ = -K \bigtriangledown \cdot \mathbf{v} + K\frac{\partial i_V}{\partial t} \tag{2.10}$$

with i_V being the volume density of volume injection.

2.3 The reciprocity theorem

The temporal Fourier transform of a space and time dependent quantity $f(\mathbf{x}, t)$ is defined as

$$F(\mathbf{x}, \omega) = \int_{-\infty}^{\infty} f(\mathbf{x}, t) e^{(-i\omega t)} dt \tag{2.11}$$

By applying such a Fourier transform to the equation of motion (equation 2.1) and the constitutive law (2.10) gives

$$\bigtriangledown P(\mathbf{x}, \omega) = i\omega\rho \mathbf{V}(\mathbf{x}, \omega) \tag{2.12}$$

$$i\omega P(\mathbf{x}, \omega) = i\omega K i_V - K \bigtriangledown \cdot \mathbf{V}(\mathbf{x}, \omega) \tag{2.13}$$

Equation 2.12 can be modified as

$$\bigtriangledown \cdot (\frac{1}{\rho} \bigtriangledown P(\mathbf{x}, \omega)) = i\omega \bigtriangledown \cdot \mathbf{V}(\mathbf{x}, \omega) \tag{2.14}$$

which in combination with equation 2.13 gives

$$- \bigtriangledown \cdot (\frac{\bigtriangledown P(\mathbf{x}, \omega)}{\rho}) + \frac{\omega^2}{K} P(\mathbf{x}, \omega) = S(\mathbf{x}, \omega) \tag{2.15}$$

where $S = \omega^2 i_V$. We continue investigating the relationship between the two solutions of equation 2.15

$$-\bigtriangledown \cdot (\frac{\bigtriangledown P_1(\mathbf{x},\omega)}{\rho}) + \frac{\omega^2}{K} P_1(\mathbf{x},\omega) = S_1(\mathbf{x},\omega) \tag{2.16}$$

$$-\bigtriangledown \cdot (\frac{\bigtriangledown P_2(\mathbf{x},\omega)}{\rho}) + \frac{\omega^2}{K} P_2(\mathbf{x},\omega) = S_2(\mathbf{x},\omega) \tag{2.17}$$

where $P_1(\mathbf{x},\omega)$ and $P_2(\mathbf{x},\omega)$ are the pressure fields generated from the different source injections. Next, multiply equation 2.16 with $P_2(\mathbf{x},\omega)$ and equation 2.17 with $P_1(\mathbf{x},\omega)$, and subtract one from the other to obtain

$$\begin{aligned} S_2 P_1(\mathbf{x},\omega) - S_1 P_2(\mathbf{x},\omega) = P_2(\mathbf{x},\omega) \bigtriangledown \cdot (\frac{\bigtriangledown P_1(\mathbf{x},\omega)}{\rho}) \\ -(P_1(\mathbf{x},\omega) \bigtriangledown \cdot (\frac{\bigtriangledown P_2(\mathbf{x},\omega)}{\rho}) \end{aligned} \tag{2.18}$$

The above equation determines the relationship between the two pressure fields at any point in the system, but it is also possible to relate the two pressure fields within a given volume V

$$\begin{aligned} \int_V (S_2 P_1(\mathbf{x},\omega) - S_1 P_2(\mathbf{x},\omega)) dV \\ = \int_V (P_2(\mathbf{x},\omega) \bigtriangledown \cdot (\frac{\bigtriangledown P_1(\mathbf{x},\omega)}{\rho}) - (P_1(\mathbf{x},\omega) \bigtriangledown \cdot (\frac{\bigtriangledown P_2(\mathbf{x},\omega)}{\rho})) dV \end{aligned} \tag{2.19}$$

The above equation can be simplified by applying the following product rule for divergence stating that $f_2 \bigtriangledown \cdot (\bigtriangledown f_1) = \bigtriangledown \cdot (f_2 \bigtriangledown f_1) - \bigtriangledown f_1 \bigtriangledown f_2$, where f_1 and f_2 are $P_1(\mathbf{x},\omega)$ and $P_2(\mathbf{x},\omega)$ in this case (Arfken et. al., 2012, A). Equation 2.19 then reduces to

$$\begin{aligned} \int_V S_2 P_1(\mathbf{x},\omega) - S_1 P_2(\mathbf{x},\omega) dV = \int_V [\bigtriangledown \cdot (\frac{P_2(\mathbf{x},\omega) \bigtriangledown P_1(\mathbf{x},\omega)}{\rho}) - \frac{\bigtriangledown P_1(\mathbf{x},\omega) \bigtriangledown P_2(\mathbf{x},\omega)}{\rho}] \\ -[\bigtriangledown \cdot (\frac{P_1(\mathbf{x},\omega) \bigtriangledown P_2(\mathbf{x},\omega)}{\rho}) - \frac{\bigtriangledown P_1(\mathbf{x},\omega) \bigtriangledown P_2(\mathbf{x},\omega)}{\rho}] dV \\ = \frac{1}{\rho} \int_V [\bigtriangledown \cdot (P_2(\mathbf{x},\omega) \bigtriangledown P_1(\mathbf{x},\omega)) - \bigtriangledown \cdot (P_1(\mathbf{x},\omega) \bigtriangledown P_2(\mathbf{x},\omega))] dV \end{aligned} \tag{2.20}$$

By applying the divergence theorem $\int_V \bigtriangledown \cdot f dV = \int_S f \cdot \vec{n} dS$ (Arfken et. al., 2012, A) to

the right hand side of equation 2.20, it transforms to

$$\int_V [S_2 P_1(\mathbf{x},\omega) - S_1 P_2(\mathbf{x},\omega)] dV = \frac{1}{\rho} \int_S [P_2(\mathbf{x},\omega) \bigtriangledown P_1(\mathbf{x},\omega) - P_1(\mathbf{x},\omega) \bigtriangledown P_2(\mathbf{x},\omega)] \cdot \vec{n} dS \tag{2.21}$$

which is the acoustic reciprocity theorem in its most general form.

2.4 The representation theorem

The reciprocity theorem (equation 2.21) gives the relationship between two different wave-field states acting within a volume V with an outer surface S. By carefully defining these states, the pressure at any point within that volume can be calculated for a given problem.

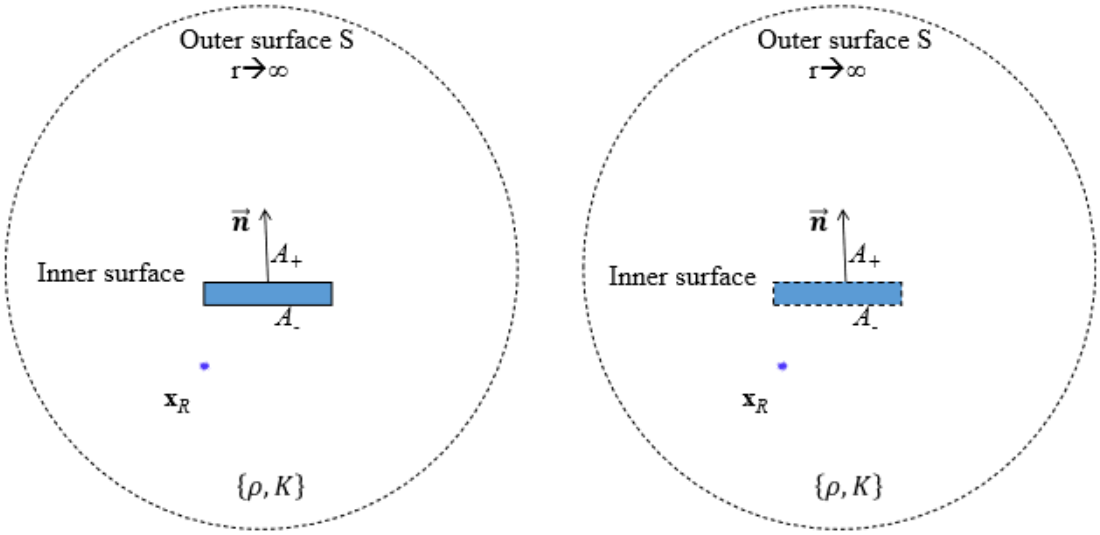

Figure 2.2: Physical state (left) and Green's state (right) where $\mathbf{x}_R$ in the latter acts as a point source (Söllner & Orji, 2017).

In the following, the problem is to solve for the pressure field generated from two closeby vibrating plates (figure 2.2). The first state corresponds to a physical point source $\delta(\mathbf{x})$ that is injected at an arbitrary point $\mathbf{x}$. This type of source generates a pressure field $P(\mathbf{x}_R, \omega)$ recorded at a point $\mathbf{x}_R$ (left in figure 2.2). This will be referred to as the physical state from here on.

The second state corresponds to a point source $\delta(\mathbf{x}-\mathbf{x}_R)$, located at the point $\mathbf{x}_R$ and will be referred to as the Green's state (right in figure 2.2). The sources can be written explicitly as ($S(\omega)$ being the spectrum of a physical source)

$$S_1 = \frac{1}{\rho}\delta(\mathbf{x})S(\omega) \tag{2.22}$$

and

$$S_2 = \frac{1}{\rho}\delta(\mathbf{x}-\mathbf{x}_R) \tag{2.23}$$

The corresponding wavefields are

$$P_1(\mathbf{x},\omega) = P(\mathbf{x},\omega) \tag{2.24}$$

and

$$P_2(\mathbf{x},\omega) = G(\mathbf{x},\mathbf{x}_R,\omega) \tag{2.25}$$

with $G(\mathbf{x},\mathbf{x}_R,\omega)$ representing the Green's function. By substituting equations 2.22 - 2.25 into equation 2.21 the pressure field at point $\mathbf{x}_R$ can be calculated

$$\begin{aligned} &\frac{1}{\rho}\int_V [P(\mathbf{x},\omega)\delta(\mathbf{x}-\mathbf{x}_R) - G(\mathbf{x},\mathbf{x}_R,\omega)\delta(\mathbf{x})S(\omega)]dV \\ =\frac{1}{\rho}\int_S &[G(\mathbf{x},\mathbf{x}_R,\omega) \bigtriangledown P(\mathbf{x},\omega) - P(\mathbf{x},\omega) \bigtriangledown G(\mathbf{x},\mathbf{x}_R,\omega)]\cdot\vec{n}dS \\ &\Rightarrow P(\mathbf{x}_R,\omega) = \int_V G(\mathbf{x},\mathbf{x}_R,\omega)\delta(\mathbf{x})S(\omega)dV \\ &\int_S [G(\mathbf{x},\mathbf{x}_R,\omega) \bigtriangledown P(\mathbf{x},\omega) - P(\mathbf{x},\omega) \bigtriangledown G(\mathbf{x},\mathbf{x}_R,\omega)]\cdot\vec{n}dS \end{aligned} \tag{2.26}$$

The pressure term $P(\mathbf{x}_R,\omega)$ arises from the identity $\int_V P(\mathbf{x},\omega)\delta(\mathbf{x}-\mathbf{x}_R)dV = P(\mathbf{x}_R,\omega)$ (Arfken et. al., 2012, B). Assume that physical point source $\delta(\mathbf{x})$ does not contribute to the pressure field which implies

$$P(\mathbf{x}_R, \omega) = \int_S [G(\mathbf{x}, \mathbf{x}_R, \omega) \bigtriangledown P(\mathbf{x}, \omega) - P(\mathbf{x}, \omega) \bigtriangledown G(\mathbf{x}, \mathbf{x}_R, \omega)] \cdot \vec{n} dS \tag{2.27}$$

The contribution to the surface integral comes from both the outer surface S and the inner surface A. If the Sommerfeld radiation condition (when the radius of the outer surface S goes to infinity) is applied, the contribution to the surface integral from the outer surface S goes to zero (Peters & Stoker, 1954). This means that the only contribution to the surface integral comes from the inner surface A

$$P(\mathbf{x}_R, \omega) = \int_A [G(\mathbf{x}, \mathbf{x}_R, \omega) \bigtriangledown P(\mathbf{x}, \omega) - P(\mathbf{x}, \omega) \bigtriangledown G(\mathbf{x}, \mathbf{x}_R, \omega)] \cdot \vec{n} dA \tag{2.28}$$

Assume now that the inner surface A is actually a vibrating plate with two surfaces with opposite normal vectors, with an infinitesimal distance between them, as shown in figure 2.2. The surface integral in equation 2.28 can then be divided into two different parts, one for each side of the inner surface

$$\begin{aligned} P(\mathbf{x}_R, \omega) = &\int_{A_+} [G(\mathbf{x}, \mathbf{x}_R, \omega) \bigtriangledown P(\mathbf{x}, \omega) - P(\mathbf{x}, \omega) \bigtriangledown G(\mathbf{x}, \mathbf{x}_R, \omega)] \cdot \vec{n} dA_+ \\ &- \int_{A_-} [G(\mathbf{x}, \mathbf{x}_R, \omega) \bigtriangledown P(\mathbf{x}, \omega) - P(\mathbf{x}, \omega) \bigtriangledown G(\mathbf{x}, \mathbf{x}_R, \omega)] \cdot \vec{n} dA_- \end{aligned} \tag{2.29}$$

The subtraction of the second integral arises from the opposite normal vectors. This results in the cancellation of the second term in each surface integral since the Green's function and its gradient and the pressure field are continuous across the plates. However, the pressure gradients are opposite of each other due to the two vibrating plates pushing the surrounding medium in opposite directions. The equation is then reduced to

$$P(\mathbf{x}_R, \omega) = \int_A G(\mathbf{x}, \mathbf{x}_R, \omega) \bigtriangledown [P(\mathbf{x}, \omega)]_{A-}^{A+} \cdot \vec{n} dA \tag{2.30}$$

where the notation $[]_{A-}^{A+}$ denotes the difference in pressure gradient between the upper

and lower inner surface. The pressure term in the above equation can be replaced by an acceleration term ($a(\mathbf{x},\omega) = i\omega V(\mathbf{x},\omega)$) scaled with density from the equation of motion (equation 2.12), yielding

$$P(\mathbf{x}_R,\omega) = \rho \int_A (G(\mathbf{x},\mathbf{x}_R,\omega) \bigtriangledown [a(\mathbf{x},\omega)]_{A-}^{A+} \cdot \vec{n} dA \tag{2.31}$$

The pressure field can be calculated at any point $\mathbf{x}_R$ in a volume if the solution to the Green's function and the difference in acceleration between the two sides of the vibrating plates are known. Since the medium is water, the Green's function has the analytical solution

$$G(\mathbf{x},\mathbf{x}_R,\omega) = \frac{1}{4\pi R} e^{ikR}, R = \mid \mathbf{x} - \mathbf{x}_R \mid \tag{2.32}$$

in the frequency domain, where $k = \frac{\omega}{c}$ is the wave number and R is the distance from source to the point of interest. The time domain equivalent is $\frac{1}{4\pi R}\delta(t - \frac{R}{c})$ (Howell, 2001, A). In Appendix C, fundamental concepts related to sweep design and acceleration response are discussed in detail.

Chapter 3

Modeling the Source Wavefield from a Marine Vibrator

3.1 Sweep design

The pressure wave field generated from a marine vibrator is described by equation 2.31 where both the density of the water column and the Green's function at any point in the system are known. The only missing part is the acceleration term which in general can be described as (no spatial variations along the vibrating plates)

$$a(t) = esin[2\pi(\phi_0 + \phi(t))] \tag{3.1}$$

where e is the envelope function and $\phi(t)$ is the phase function. It is assumed here that the initial phase ϕ_0 is zero. This thesis will focus on a linear upsweep which means that the sweep will start from a low frequency f_0 and increase linearly to a higher frequency f_1 over a period of time T known as the sweep length

$$\begin{aligned} f(t) &= f_0 + bt \\ b &= \frac{f_1 - f_0}{T} \end{aligned} \tag{3.2}$$

Taking the integral of the instantaneous frequency $f(t)$ yields the instantaneous phase function $\phi(t)$

$$\begin{aligned} \phi(t) &= \int_0^t f(t)dt \\ \phi(t) = \int_0^t (f_0 + bt)dt &= \int_0^t (f_0 + (\frac{f_1 - f_0}{T})t)dt \\ \Rightarrow \phi(t) &= [f_0 t + (\frac{f_1 - f_0}{2T})t^2] \end{aligned} \tag{3.3}$$

Substituting $\phi(t)$ into the acceleration equation 3.1 yields

$$a(t) = esin[2\pi(f_0 t + (\frac{f_1 - f_0}{2T})t^2)] \tag{3.4}$$

The phase is now determined by $sin(\phi(t))$, but the strength or amplitude of the signal is determined by the envelope function e. For a linear sweep, putting e as a constant will give rise to flat amplitude spectra of acceleration and pressure due to equation 3.4 and 2.31.

Determining the value of the envelope function analytically can be done for a single point since the distance from that point to the point of measurement is constant. For a single point on a vibrating plate, the integral from equation 2.31 vanishes and the pressure is then just a scaled version of the acceleration. Since the density and the solution to Green's function are known (equation 2.32), the acceleration can then be used as a control-parameter to obtain the pressure output of interest at any given distance (cf. equation 3.5)

$$\begin{aligned} P(\mathbf{x}_R, \omega) &= \rho G(\mathbf{x}, \mathbf{x}_R, \omega) A(\mathbf{x}, \omega)_z \\ \rightarrow A(\mathbf{x}, \omega)_z &= \frac{P(\mathbf{x}_R, \omega)}{\rho G(\mathbf{x}, \mathbf{x}_R, \omega)} \\ &= \frac{10000Pa * \frac{4\pi}{m}}{1000kg/m^3} \\ &= 125.66m/s^2 \end{aligned} \tag{3.5}$$

By then using $125.66m/s^2$ as the envelope function, the pressure output at 1 meter gives $10000Pa$ (or $0.1bar$) and also yields a flat amplitude spectrum of acceleration (cf. discussion in Appendix C).

This has been applied to figure 3.1 and 3.2 to ensure a pressure output of $0.1bar$ at 1 meter

away in the frequency band of $f_0 = 0Hz$ and $f_1 = 20Hz$. Calculating the plate velocity and plate motion numerically is done by taking the Fourier transform of the acceleration and then divide by $i\omega$ to obtain plate velocity ($V(\omega) = A(\omega)/i\omega$), and divide by $-\omega^2$ to obtain plate motion ($U(\omega) = A(\omega)/-\omega^2$).

It is numerically possible to calculate the plate acceleration for an entire stack of plates using $e = 125.66m/s^2$. By using the above relations and equation 2.31 the results shown in figure 3.1 were obtained.

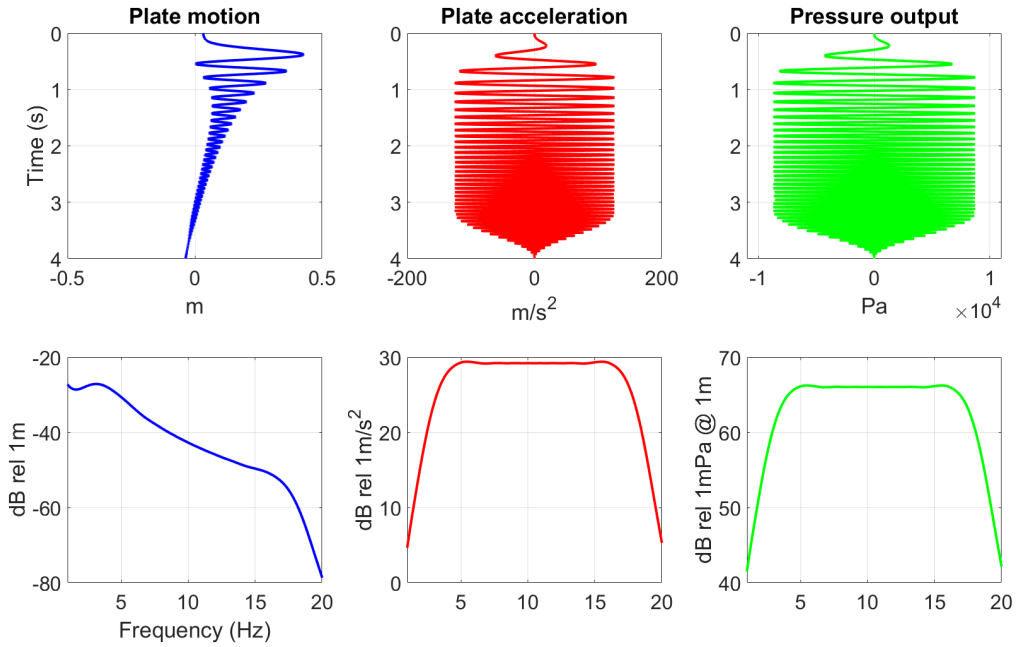

Figure 3.1: The normalized output from 11 plates 1 meter away from the center of the stack of plates.

The pressure output shown in figure 3.1 is the pressure from 11 plates stacked together with $0.2m$ spacing between them measured at 1 meter away from the center of the middle plate. A taper has been applied to the signal to remove the ringing in the amplitude spectra caused by Gibb's phenomenon. However, the pressure is normalized by dividing the total pressure output by the number of points on a single plate and the number of plates (11 in this case). The results should be the amount of pressure output equal to a single point on a vibrating plate

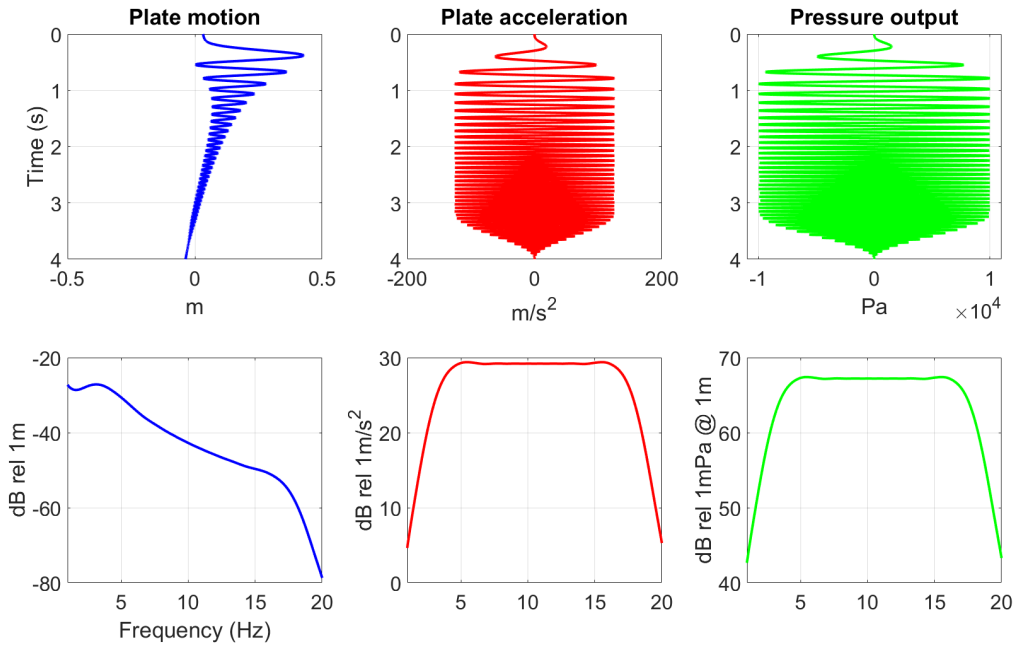

Figure 3.2: The output from a single point 1 meter away from the center of the stack of plates.

When comparing the pressure output in figure 3.1 with the actual pressure output from a single point shown in figure 3.2 one can observe that they are not equal. This is due to the fact that the envelope function was calculated for a single point, meaning that the normalization does not take into account the areal extent of the plates. As the distance from the plates to a point of measure increases, the difference in pressure output should approach zero. This means that by measuring far enough away from the source, the source can be thought of as a point source.

Since the signal is defined as the plate acceleration $a(t)$, the plate motion shown in figures 3.1 and 3.2 comes as a consequence of the envelope function. This means that in order to obtain a flat amplitude spectrum of acceleration, the plate has to behave in a certain manner in practice. It is observed from figures 3.1 and 3.2 that the plate has to move significantly in the beginning of the sweep in order to maintain the flat amplitude of acceleration.

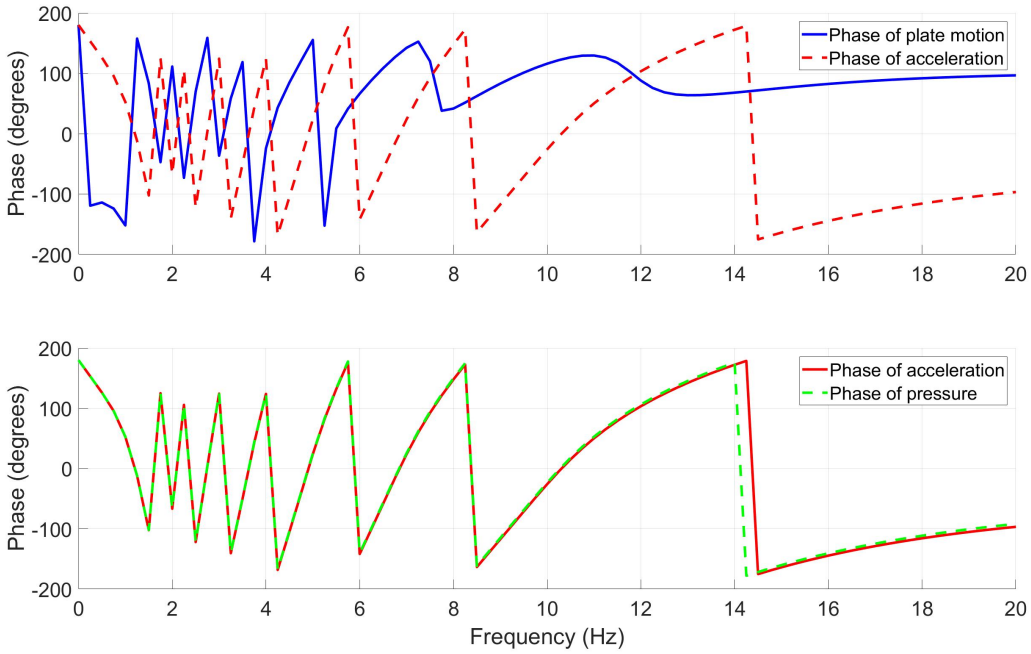

Figure 3.3: Comparative phase spectra plots between plate motion/plate acceleration and plate acceleration/pressure output from figure 3.1.

When comparing the phase of the plate motion and plate acceleration in figure 3.3, one can observe that they are completely out of phase. This is because the plate motion is given by the double time integral (or division by $(i\omega)^2$ in the frequency domain).

The opposite is the case when comparing the phase of plate acceleration and pressure output (figure 3.3). As previously mentioned, the pressure can be though of as a scaled version of plate acceleration when the pressure output is normalized to a single point. The point of measurement for the pressure output is $1m$ away from the plates, which actually causes a slight shift due to the Green's function (equation 2.32). The exponential part of the Green's function determines the phase of the pressure output and it is distance dependent (r). This phase shift is only about $6°$ at $1m$ away from the source.

Figures 3.1 and 3.3 show the characteristics of a generated sweep between 0 and 20Hz recorded close to the source. It will therefore be assumed in this work that this is the true output from a vibrating stack of plates. This assumption does not take into account directivity, but this aspect has already been discussed by Nguyen, (2017). Nevertheless, the frequency band and sweep length as seen in figure 3.1 will now be extended from $0 - 20Hz$ over 4 seconds to $5 - 100Hz$ over 5 seconds. This output will be used as a

notional source signature when modeling synthetic data in the next section.

3.2 Generating stationary synthetic data

Synthetic data can now be modelled by utilizing the notional source signature found in section 3.1. This will be done using the Nucleus+ which is a PGS in house modeling software where the user can freely create many different models with a variety of survey configurations. The survey configuration includes vessel position and velocity, number of sources and receivers, what type of source and the extent of the survey among many other options. Different types of modeling may be used as well, but only finite difference modeling were used in this thesis as this type of modeling can accommodate for motion which will be relevant for later discussions in this thesis work.

The amplitude spectrum of the sweep in section 3.1 has now been extended to range from 5 to 100Hz as a broader frequency band is of interest in case of shallower reservoirs as in the Barents Sea. A basic model consisting of two diffractors within a homogenious medium as seen in figure 3.4 has been employed to investigate resolution aspects.

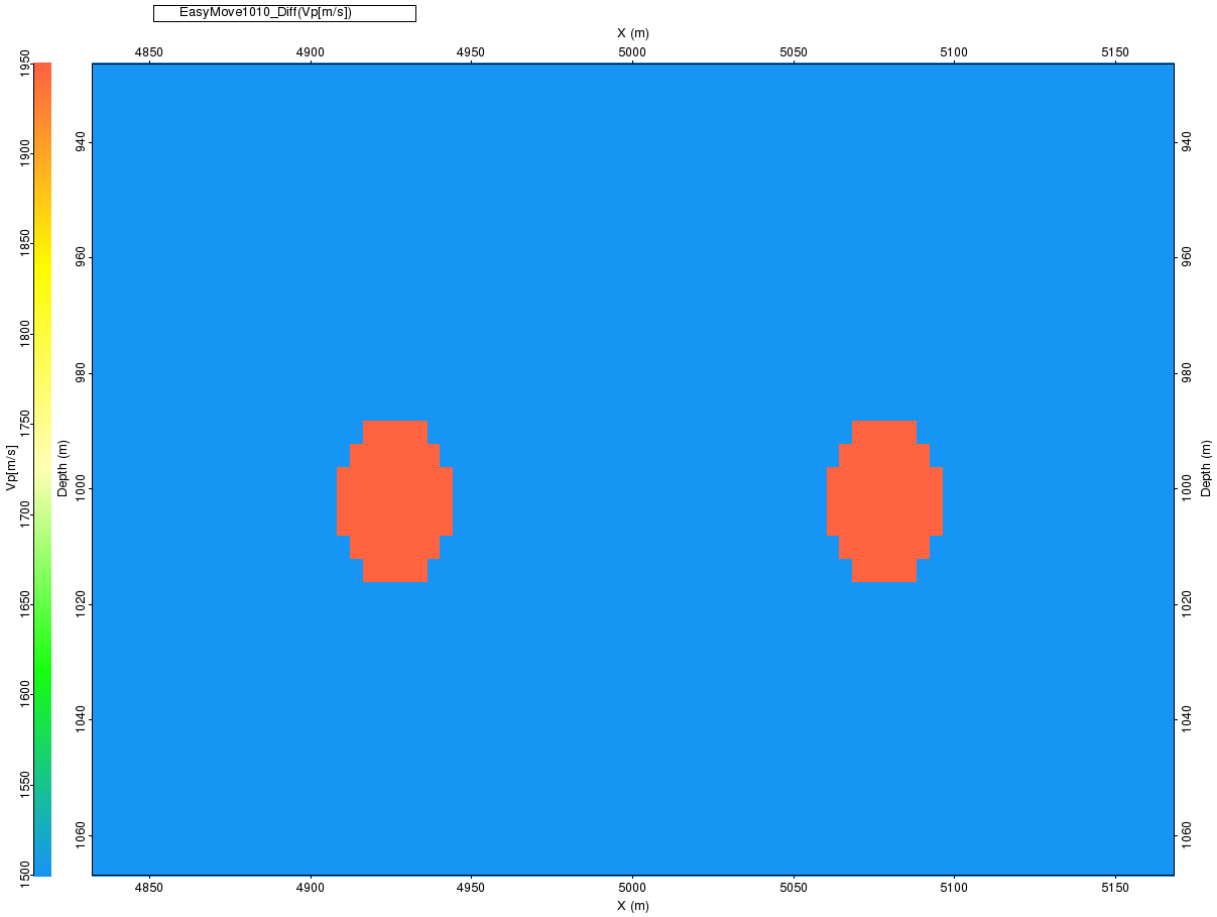

Figure 3.4: A 10000m wide and 4000m deep model consisting of only two diffractors located at 1000m depth, 150m apart. The grid size is 4x4m.

This model was chosen primarily for its simplicity which makes it possible to isolate the effects of a continues wavefield. Having a more complex model would introduce other effects not related to a marine vibrator sweep. Such effects, i.e. multiples, already have well known corrections. Another reason for this choice of model was to check the limit of resolution for a sweep wavelet. The resolution obtained after migration is also investigated for this data set.

3.3 Survey configuration

Initially, the survey configuration will only include 200 stationary sources recorded by a single streamer containing 960 receivers. This configuration is quite simplistic, but allows for a better understanding of the sweep. In addition, deblending and motion correction do not need to be applied with this survey configuration. Figure 3.5 illustrates this survey

configuration.

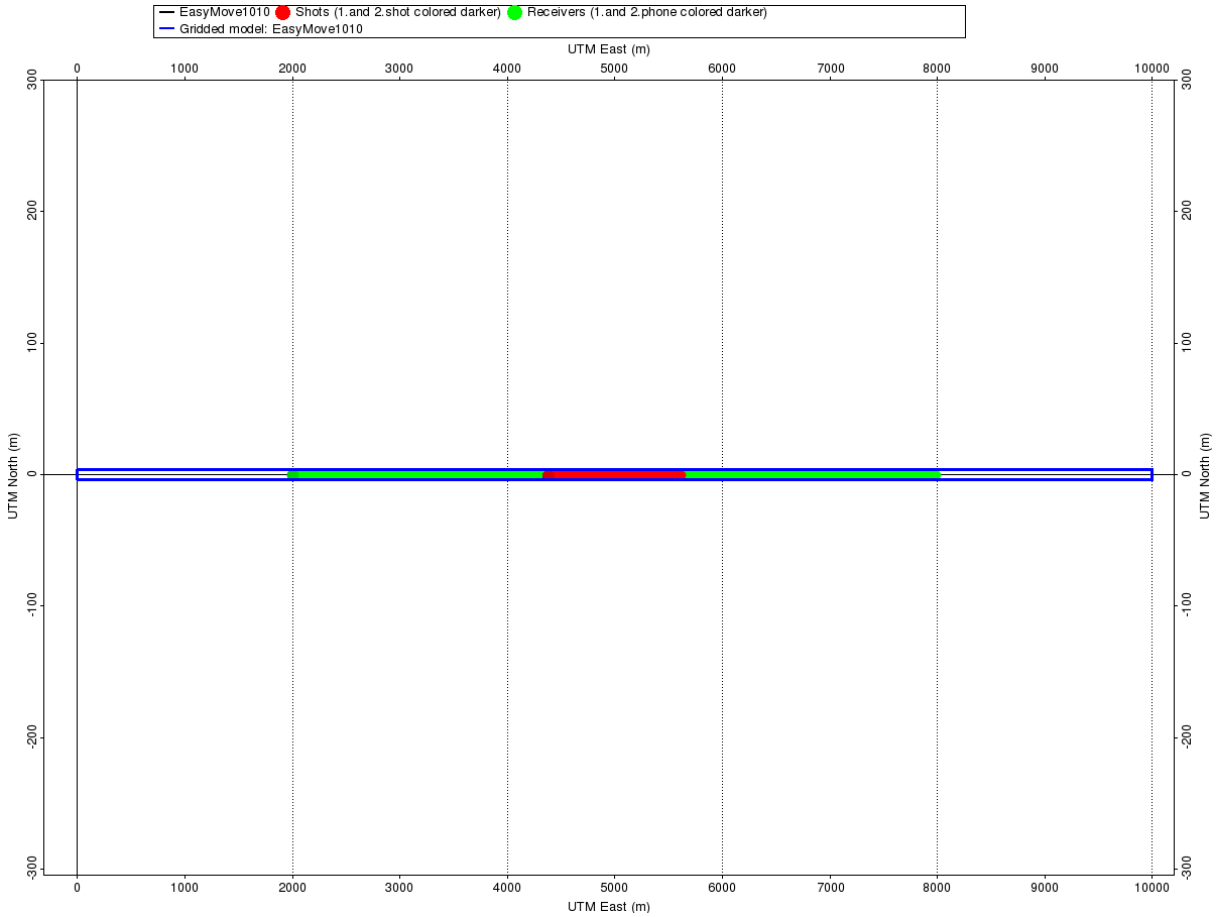

Figure 3.5: Survey configuration of sequentially fired stationary sources (red) and recorded by a streamer (green) over the model (blue).

The red dots in figure 3.5 shows where each shot is located. The source emits the sweep (figure 3.2) sequentially starting from left. When one shot is fired, there is a delay in which the pressure wave field propagates for some time before the next sweep is emitted. The first sweep is emitted at $4375m$ and the last sweep is emitted at $5625m$ relative to origo, for a total of 200 shots spaced $6.25m$ apart covering $1250m$. As mentioned in the previous section, the sweep is now defined between frequencies $f_0 = 5Hz$ and $f_1 = 100Hz$.

The receiver array consist of 960 receivers also spaced $6.25m$ apart covering a total of $6000m$ starting from $2000m$ from origo. The receiver array and the source array were located at a depth of respectively 480m and 490m. This is very unrealistic, but this choice together with the shear size of the model make it possible to neglect the boundary issues of the modeling software. In addition, no sea surface reflections are included in the

modeling as the main purpose is to investigate the effects of a sweep wavelet.

3.4 Raw data

The given model and survey configuration were used to generate a dataset using 2D finite-difference modeling with a $4x4m$ grid size and the raw data generated is displayed in figure 3.6 in case of shot number 100 (mid shot).

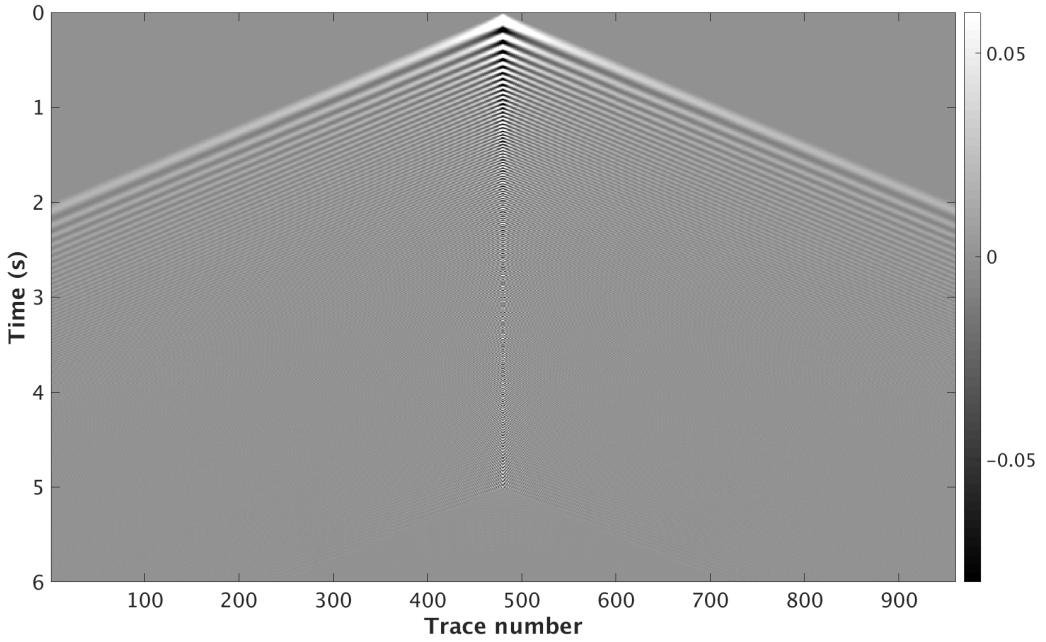

Figure 3.6: Raw data generated from model in figure 3.4 and survey configuration in figure 3.5. This shot gather is taken from shot number 100 from the record.

It can be observed from figure 3.6 that the direct wavefield is not removed from the data as the zero-offset trace has large amplitudes at time = 0. The direct wavefield is of course recorded at later times with increasing offset.

Since this dataset is synthetically generated, it is possible to remove the direct wavefield by simply creating a new dataset, but using a model where the diffractors are removed and then subtracting one dataset from the other. This is obviously not possible with real data, but has been performed here for time saving reasons. Removing the direct wavefield from real data can actually be a challenge as parts of the direct wavefield often blend with primary reflections.

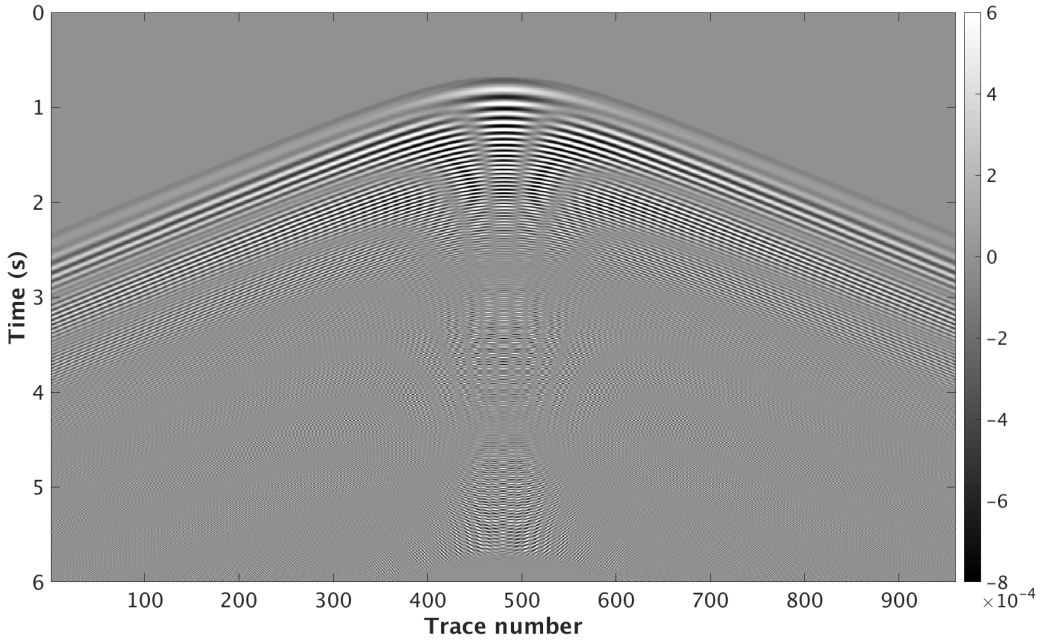

Figure 3.7: Shot gather as shown in figure 3.6 but without the direct wavefield.

It can be observed from figure 3.7 that there is no longer an amplitude present at time t = 0 at zero offset which means the direct wavefield has been removed. By comparing figures 3.6 and 3.7 it is clear that the direct wavefield dominated the raw dataset. What is left of the data must then be the reflected energy from the two diffractors.

The data seen in figure 3.7 is a convolution between the source wavelet and the refletivity series (Todoeschuck & Jensen, 1989). How to remove the phase of the source wavelet from the data will be discussed in the next section.

Chapter 4

Data Processing and Migration

Now that the data has been modeled, it needs to be properly processed in order to obtain an image of the scatteres. The cross-correlation process is now applied to the data in figure 3.7 in order to compress the sweep signal. Furthermore, the cross-correlated data will then be imaged by a finite difference migration which will allow us to obtain an image of the scatterers.

4.1 Cross-correlation

Cross-correlation is a way to compare two signals with each other and identify possible similarities. The mathematical definition in the time domain is as follows (Howell, 2001, B)

$$f \times g(n) = \int_{-\infty}^{\infty} \overline{f(m)} g(m+n) \tag{4.1}$$

where f and g are two different signals, $\overline{f}$ denotes the time reversal of the signal f, $\times$ denotes cross-correlation, m is the length of the signal and n is the "lag" of the cross-correlation process. The process of cross-correlation as seen from its definition (4.1) resembles the convolutional process, but with the first signal being time reversed. The general idea behind the process of cross-correlation in the time domain is sketched in figure 4.1.

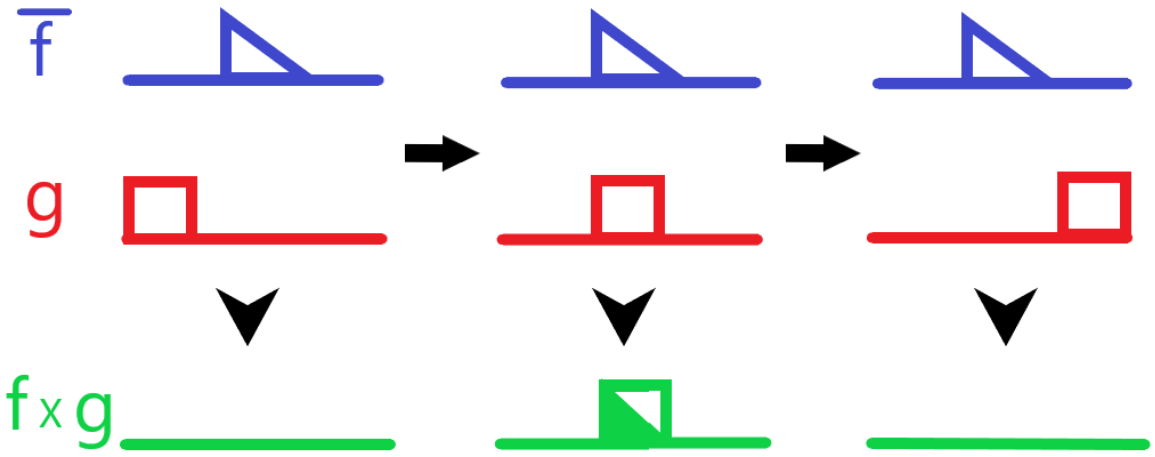

Figure 4.1: Sketch of how cross-correlation is performed in the time domain. The cross-correlation (green) is a step wise multiplication and summation between the flipped signal signal $\overline{f}$ (blue) and a different signal g (red) in the time domain.

As can be seen from figure 4.1, the signal $\overline{f}$ is multiplied with signal g in steps. When moving to the next step, denoted in figure 4.1 as elongated arrows pointing right, the signal g shift to the right. Each step is called a lag and is defined in equation 4.1. One can observe from figure 4.1 that the first and third step yields no product, meaning the signal has no correlation in these steps. On step two however, there are some correlation, marked in figure 4.1 as a filled triangle.

When performing cross-correlation on two identical signals, the operation is called auto-correlation. The auto-correlation has the most significant correlation when the signal is aligned with itself.

A seismic signal is of course much more complex than what is showed in figure 4.1, but the principle is exactly the same. When cross-correlation is performed between the vibroseis data and the source wavelet, the effects of the sweep on the data will be minimized. This is because the recorded seismic trace for a given source receiver $u(\mathbf{x}_g, \mathbf{x}_s, t)$ (synthetic seismic in this thesis) is a convolution between the sweep wavelet $s(t)$ and the reflectivity response $r(\mathbf{x}_g, \mathbf{x}_s, t)$

$$u(\mathbf{x}_g, \mathbf{x}_s, t) = s(t) * r(\mathbf{x}_g, \mathbf{x}_s, t) \tag{4.2}$$

where $*$ denoted the mathematical process of convolution. The reflectivity response

$r(\mathbf{x}_g, \mathbf{x}_s, t)$ represents the data recorded for the same source receiver location in case of an impulsive source (e.g. $S(\omega) = 1$). In the frequency domain, the convolution becomes a multiplication

$$\begin{aligned} U(\mathbf{x}_g, \mathbf{x}_s, f) &= S(f)R(\mathbf{x}_g, \mathbf{x}_s, f) \\ &= A_S e^{i\phi_S} A_R e^{i\phi_R} = (A_S A_R) e^{i(\phi_S + \phi_R)} \end{aligned} \tag{4.3}$$

where the amplitude and phase terms of the sweep and earth's reflectivity response have been introduced. Cross-correlation between the recorded data and the sweep wavelet ($U'(\mathbf{x}_g, \mathbf{x}_s, f)$) is then a multiplication of equation 4.3 with the complex conjugated sweep wavelet (Howell, 2001, A)

$$\begin{aligned} U'(\mathbf{x}_g, \mathbf{x}_s, f) &= (A_S A_R) e^{i(\phi_S + \phi_R)} A_S e^{-i\phi_S} \\ &= (A_S^2 A_R) e^{i\phi_R} \end{aligned} \tag{4.4}$$

From equation 4.4 it is seen that the amplitude of the sweep is squared and the phase of the sweep is removed as a result of the cross-correlation. What is left of the phase in the recorded data is the phase of the earth's reflectivity response.

The result shown in figure 4.2 was obtained when cross-correlation is applied to the data in figure 3.7.

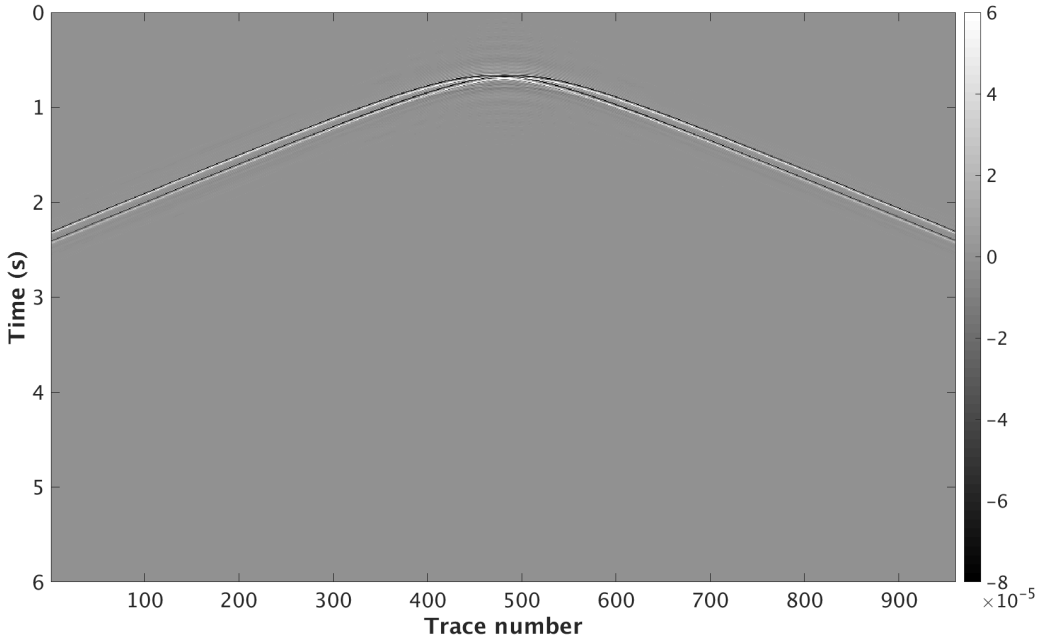

Figure 4.2: Source gather after cross-correlation has been performed (source number 100).

As can be seen from figure 4.2, the phase of the sweep has been successfully removed. To further investigate the quality of the controlled data after cross-correlation, a finite difference migration was employed. This will be topic in the next section.

4.2 Wave equation based finite-difference migration of cross-correlated data

A shot-point driven finite-difference wave equation migration scheme developed by PGS was employed to migrate the cross-correlated data. The algorithm does not only require the data set itself, but also a velocity model and a wavelet for propagation on the finite difference grid. As this is synthetic data, the background velocity model is known. The propagation wavelet needs to be an auto-correlation of the source sweep wavelet. This is because the data now have been cross-correlated with the sweep (cf. equation 4.4).
The single-source acquisition aperture, which is the lateral extent covered by the receivers for a fixed source, will be considered in the further analysis. This migration aperture can again be related to the Rayleigh criterion
The Rayleigh criterion gives an estimate of the size of aperture needed be able to separate and image two points (sources of emission). Figure 4.3 gives a schematics of the general idea.

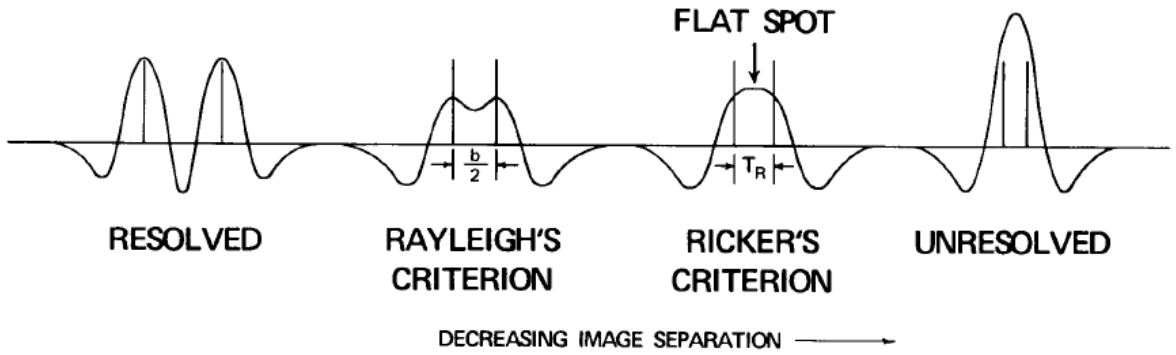

Figure 4.3: The general idea of the Rayleigh criterion where a given aperture will be able to completely resolve (left), barely resolve (middle) or not resolve (right) two events (modified version from Kallweit & Wood, 1982).

These two points can be though of as points of emission recorded by one receiver where d is the distance between the diffractors ($150m$ in our case), L is the vertical distance from the receiver array to the diffractor depth ($510m$ in our case), θ is the average angle between the two diffractors and the receiver considered and x defines the total receiver outlay (aperture) as shown in figure 4.4.

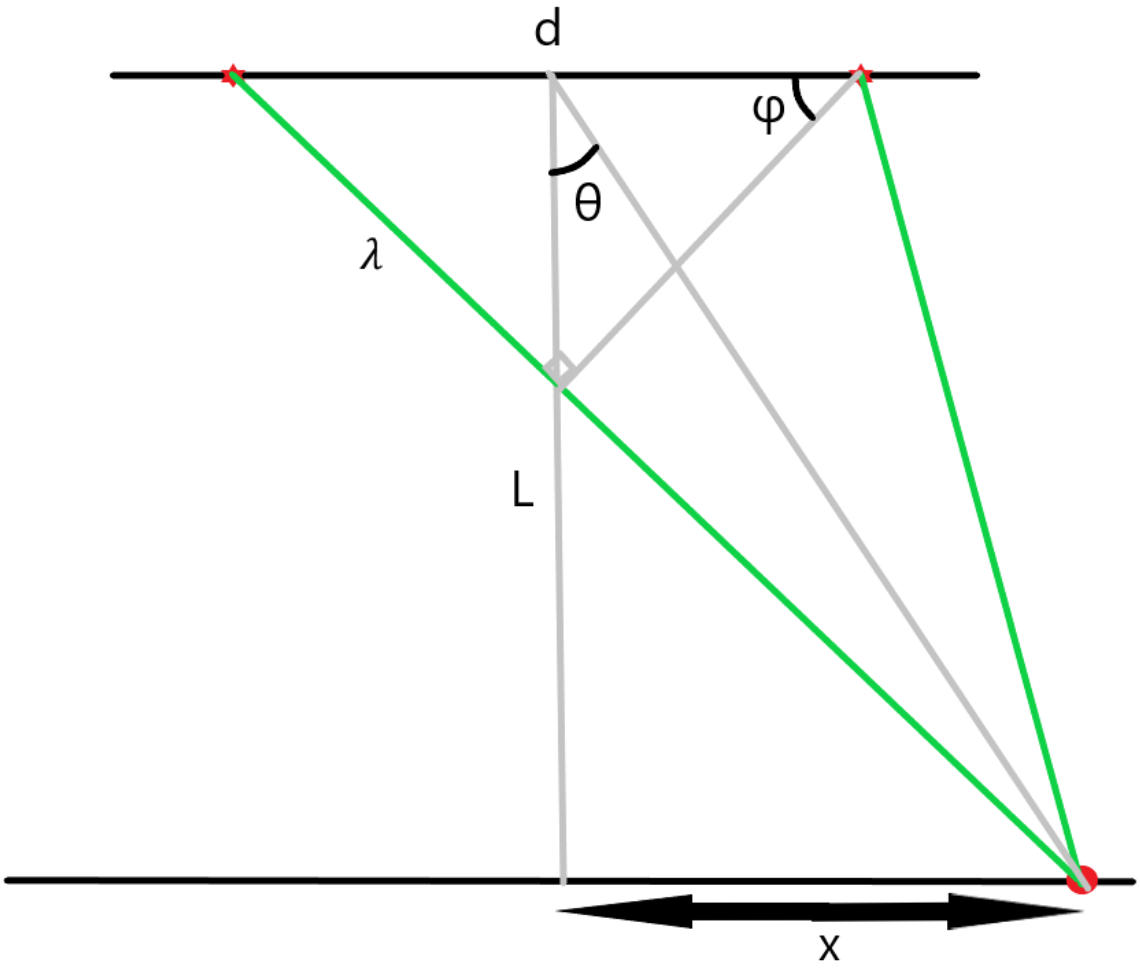

Figure 4.4: Diffractors as two points of emission (stars) recorded at a receiver (circle). Green lines represent shortest distances between respectively the diffractors and the receiver considered.

With some basic trigonometry and the small angle approximation the following relation holds

$$tan(\theta) \approx sin(\theta) = \frac{x}{L} \tag{4.5}$$

The difference in path length from the two scatterers to the outer receiver considered should be an integer number of λ (wavelength) if constructive interference is to occur. This implies that (cf. figure 4.4) that (lowest order)

$$dsin(\phi) \approx dsin(\theta) = \lambda \tag{4.6}$$

which in combination with equation 4.5 gives

$$\begin{aligned} d\frac{x}{L} &= \lambda \\ x = \frac{\lambda L}{d} &= \frac{vL}{fd} \end{aligned} \tag{4.7}$$

where λ has been replaced by $\frac{v}{f}$. Here, v can be though of as a RMS-velocity and f can be considered as a center frequency of the signal. Figure 4.5 summarizes the key parameters of the Rayleigh criterion in case of the single-source geometry.

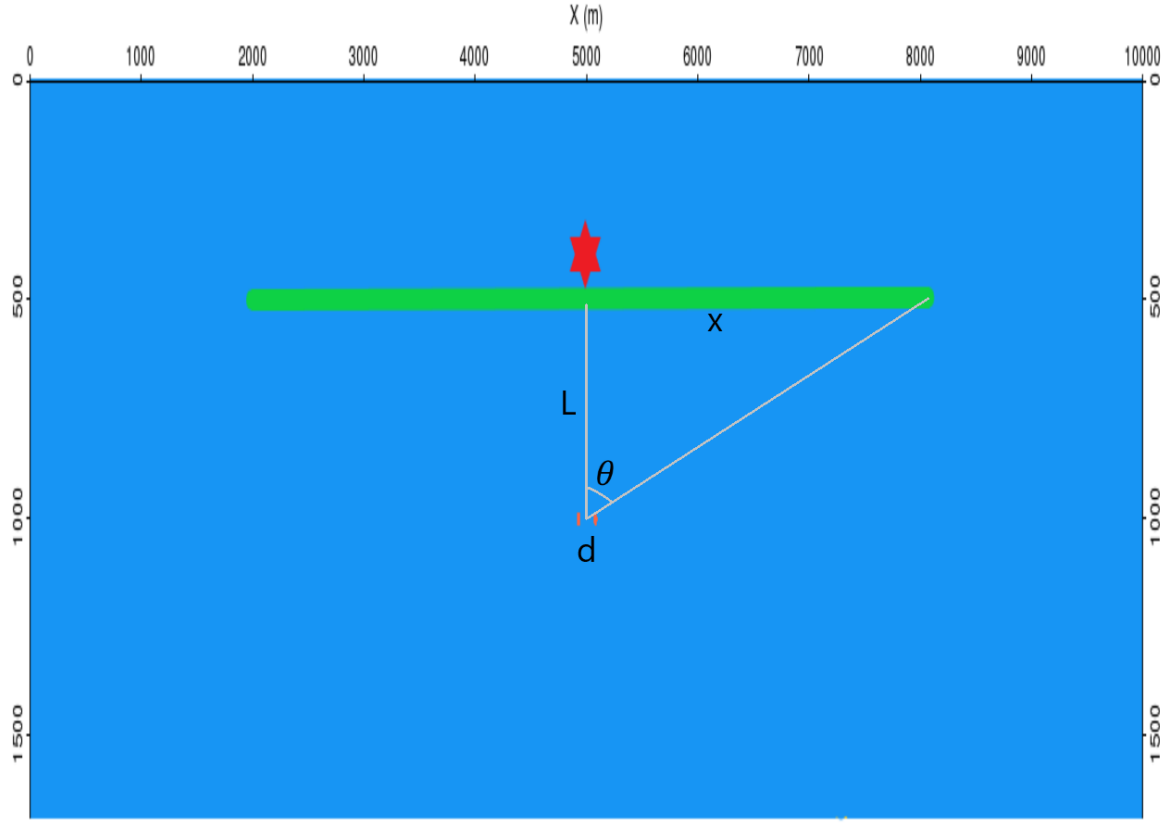

Figure 4.5: Single-source geometry and the Rayleigh criterion related to seismic aperture x and a given angle θ.

Split-spread configuration is considered in this work but since the model is symmetric around the mid shot point (#100), we only need to consider the aperture to be one-sided (single-spread) (x in figure 4.5) in the following resolution analysis.

As can be seen from equation 4.7, the migration aperture is inversely proportional to both the frequency and the distance between the diffractors. However, both depth and RMS-

velocity are proportional to the migration aperture. Increasing the distance between the diffractors or increasing the frequency allows for a lower migration aperture while higher RMS-velocity or large depth increases the migration aperture needed in order to resolve the two scatterers.

It is now possible to estimate a minimum migration aperture needed to resolve both diffractors in the model (figure 3.4). Since our model is homogeneous, the RMS-velocity is just equal to the interval velocity of the water $v_{RMS} = v_i = 1500m/s$. The choice of frequency is more difficult since the amplitude spectrum of the sweep (figure 3.1) is flat. However, since each frequency contribute equally much to the signal, the highest frequency of $100Hz$ can be chosen as it determines the limit of what can be resolved according to equation 4.7. The receivers are located at a depth of $490m$ and diffractors at $1000m$ depth, so L in this case would be $1000m - 490m = 510m$. The distance between the diffractors are $150m$ as seen in figure 3.4. The minimum migration aperture that is needed is therefore

$$x = \frac{vL}{fd} = \frac{1500m/s * 510m}{100Hz * 150m} = 51m \tag{4.8}$$

Figure 4.6 shows migrated sections of the data seen in figure 4.2 using different migration apertures

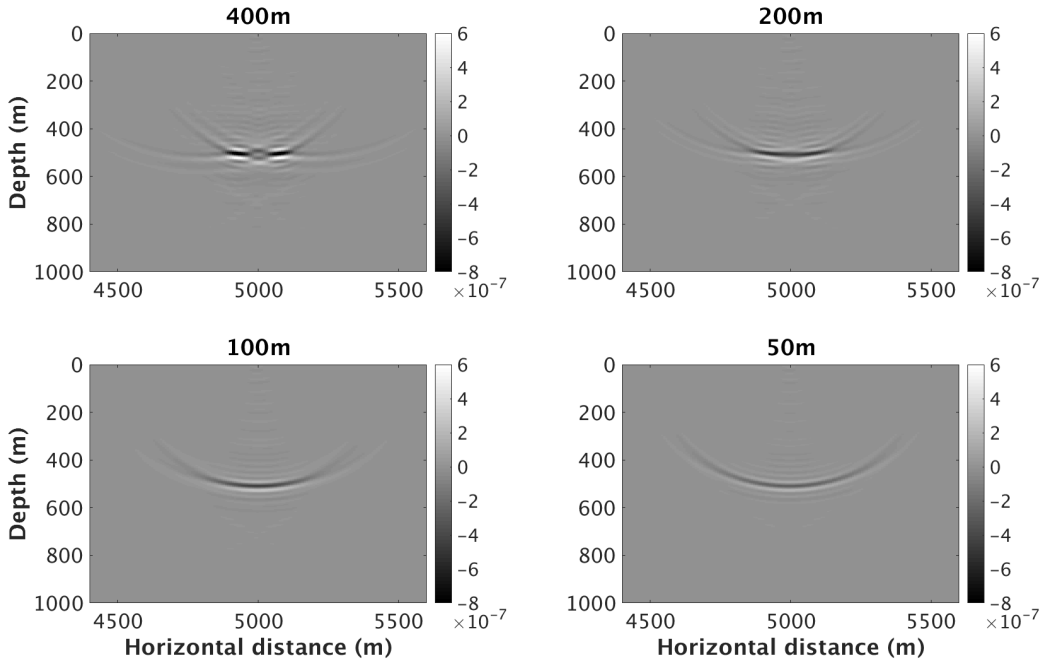

Figure 4.6: Migrated sections using $400m$ (top left), $200m$ (top right), $100m$ (bottom left) and $50m$ (bottom right) migration aperture with only 1 shot (source #100).

Figure 4.6 clearly shows that the two diffractors are resolved for a $400m$ migration aperture. It is however hard to see if the smaller apertures resolve the scatterers. To be able to analyze the horizontal resolution in more detail, an image slice was taken at the approximate depth location of the scatterers for various apertures (cf. figure 4.7).

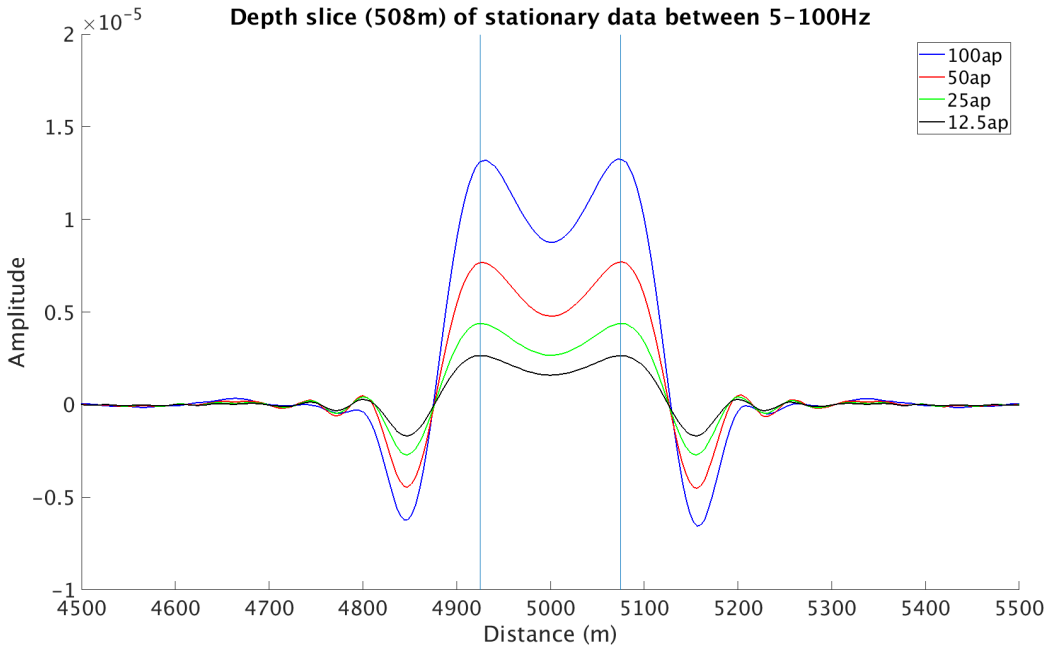

Figure 4.7: Depth slice of migrated data using $100m$, $50m$, $25m$ and $12.5m$ migration aperture. Blue vertical lines indicates actual position of the diffractors.

It can be observed from figure 4.7 that the two diffractors are resolved using both $100m$ and $50m$ apertures. One could also argue that the $25m$ and $12.5m$ depth slices are at least partially resolved for this ideal case. The reason for why these two points are being resolved at these low apertures may be a result of (i) the Rayleigh criterion only being an approximation and/or (ii) the limit of resolution is not strictly limited by the highest frequency in the band. This exercise in resolution was simply to test if the sweep would be able to resolve two point diffractors (which it can). Thus, no further investigation will be considered.

It is obvious that the number of shots also contributes to the horizontal resolution. As evidence for this, the cross-correlated section was migrated using only a $30m$ migration aperture, but with both a single (mid) and all 200 shots as shown in figures 4.8 and 4.9.

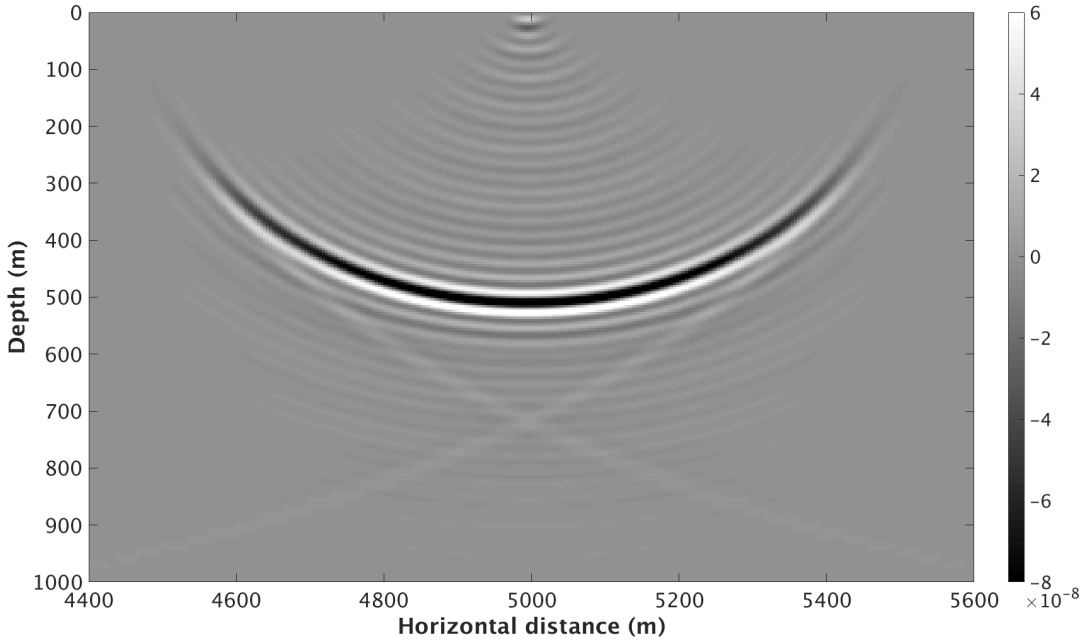

Figure 4.8: Migrated sections using a $30m$ migration aperture with the middle shot.

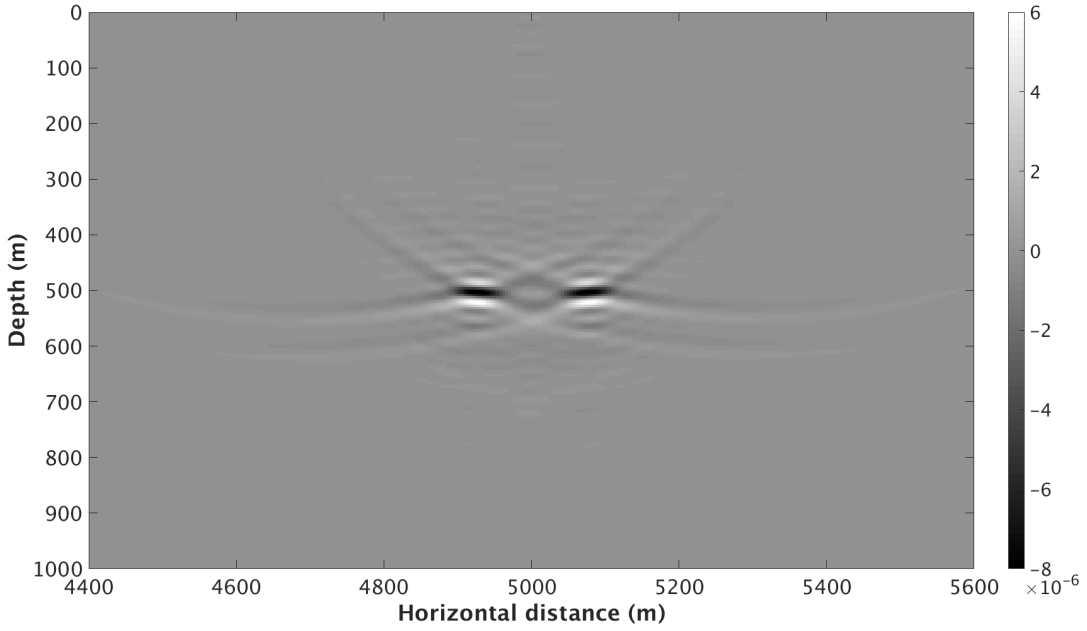

Figure 4.9: Migrated sections using a $30m$ migration aperture with 200 shots.

Figure 4.9 shows that the section migrated using all 200 shots have been able to resolve the two diffractors well. The reason for this is that the first and the last shots in the survey configuration (figure 3.5) gives additional angle information similar to an extended migration aperture even when only a few traces are migrated. This is in contrast to figure

4.8 where the two diffractors are imaged as one reflection event due to lack of angle information.

All the sections shown so far display strong migration smiles. These smiles comes as an effect of the finite-length apertures. To minimize such distortions, longer receiver lines are needed such as those employed in a seismic study. By using the more typical value of a $3000m$ aperture and all 200 shots, the image shown in figure 4.10 was obtained.

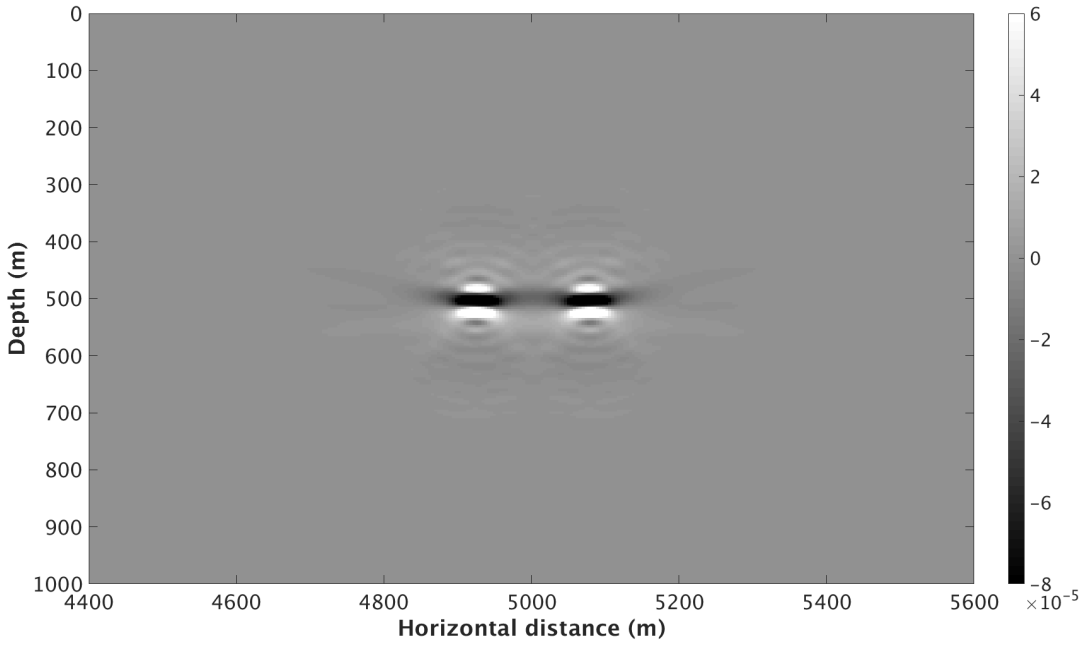

Figure 4.10: Migrated sections using $3000m$ migration aperture with all 200 shots.

The migration smiles are now removed as seen in figure 4.10. The use of smaller migration apertures in this section only served the purpose of illustrating fundamental limits with regards to resolution and migration effects (migration smiles). From here on, only the aperture of $3000m$ will be used to migrate data.

Chapter 5

Introducing a Moving Source Wavefield

Up until now, this work has only considered a stationary source, but motion will now be imposed on the source wavefield. The main problem related to motion and a continuous pressure wavefield (sweep) is that the wavefield experiences a time varying phase shift as it moves relative to a given point. This is because the distance the wave has to travel down to the diffractor and then back to the receiver is changing with time. To be able to correct for this motion, we need to consider the wave equation for a moving source.

5.1 Wave equation for a moving source

Let us consider a source moving along a horizontal line as showed in figure 5.1

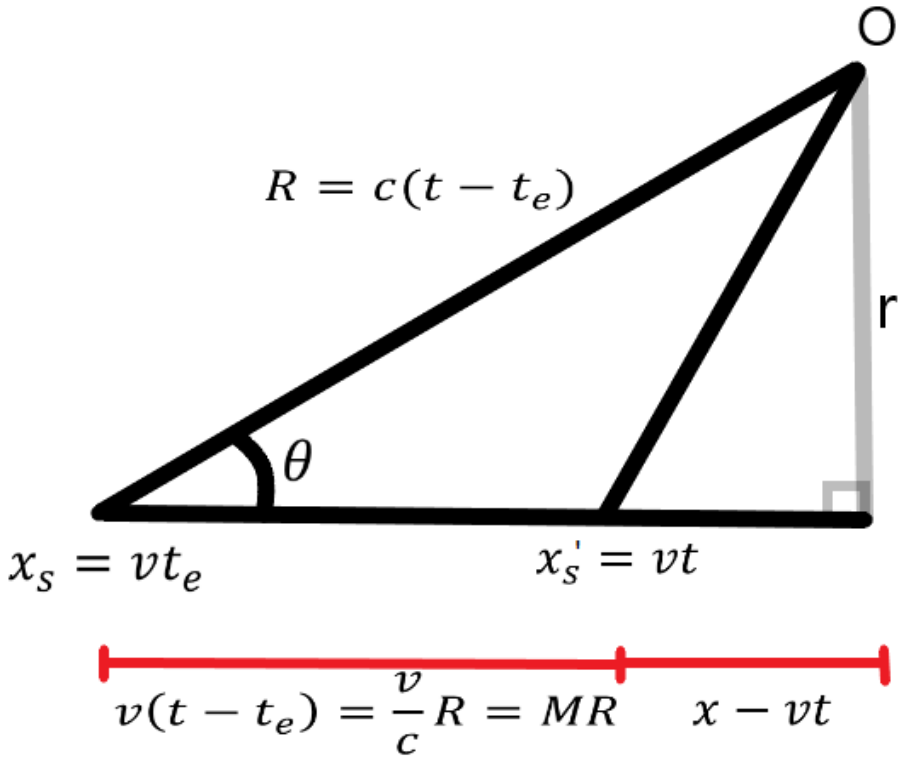

Figure 5.1: Sketch of a source initially emitting a sweep at time t_e followed by horizontal motion.

The source starts emitting a sweep at a time t_e in position $x_s = vt_e$ and the distance the pressure wave travels to a point O is called R(t). The distance R(t) changes with time as the source moves along the horizontal line and can therefore be described by $R(t) = c(t - t_e)$, where t is the time the source has been moving and c is the medium velocity. If the source travels at a velocity v over a time t, the source is positioned at a point $x_s' = vt$. Hence, the total distance traveled by the source is given by $vt - vt_e = v(t - t_e) = \frac{v}{c}R(t) = MR(t)$. Here M is the Mach number which in the subsonic case (seismic case) is much smaller than 1.

Any additional travel the source makes is then given by $x - vt$, where x is any position after x_s'. The total distance the source has traveled when point O is directly above the source is given by $(x - vt) + MR(t)$. If the vertical distance to point O is given by r, the distance from source to point O at any time is given by

$$R(t)^2 = [(x - vt) + MR(t)]^2 + r^2 \tag{5.1}$$

By rearranging equation 5.1, it can easily be solved as a second order polynomial

$$\begin{aligned} R(t)^2 &= (x-vt)^2 + 2MR(t)(x-vt) + M^2R(t)^2 + r^2 \\ \rightarrow R(t)^2(1-M^2) &- 2MR(t)(x-vt) - (x-vt)^2 - r^2 = 0 \end{aligned} \tag{5.2}$$

Equation 5.2 is then solved for R(t) to give

$$R(t) = \frac{M(x-vt) \pm \sqrt{(x-vt)^2 + (1-M^2)r^2}}{(1-M^2)} \tag{5.3}$$

In the following, a positive sign is considered since only this gives positive values for R(t) if the subsonic case is considered ($M < 1$). By defining $R_1(t) = \sqrt{(x-vt)^2 + (1-M^2)r^2}$, equation 5.3 becomes

$$R(t) = \frac{M(x-vt) + R_1(t)}{(1-M^2)} \tag{5.4}$$

It is also of interest to find R(t) as a function of angle θ (figure 5.1)

$$\begin{aligned} M(x-vt) &= M(x - vt + vt_e - vt_e) \\ &= M((x-vt_e) - v(t-t_e)) \\ &= MR(t)(cos(\theta) - M) \end{aligned} \tag{5.5}$$

Equations 5.4 and 5.5 allow for defining R_1 as

$$\begin{aligned} R_1(t) &= R(t)(1-M^2) - M(x-vt) \\ = R(t) - M^2R(t) &- MR(t)(cos(\theta) - M) \\ &= R(t)(1 - Mcos(\theta)) \end{aligned} \tag{5.6}$$

We will return to the result in equation 5.6 later. To see how this change in distance to point O affects the pressure wave field, the wave equation for a moving source along the x-axis should be investigated.

$$\bigtriangledown^2 p - \frac{1}{c^2}\frac{\partial^2 p}{\partial t^2} = s(t)\delta(x-vt)\delta(y)\delta(z) \tag{5.7}$$

where s(t) is the notional source signature (Morse & Ingard, 1968, A). Here, we only

assume motion in the x-direction and leave y and z to be constant.

Let us now introduce a frame of relative movement through a Lorentz coordinate transformation where the new coordinates are given by

$$x' = \gamma(x - vt) \tag{5.8}$$

$$y' = y \tag{5.9}$$

$$z' = z \tag{5.10}$$

$$t' = \gamma(t - \frac{v}{c^2}x) \tag{5.11}$$

where γ is the Lorentz factor which relates the actual time in the still frame to the relative time in the moving frame. When the frame of motion moves relative to the still frame, this factor is given by $\gamma = \frac{1}{\sqrt{1-\frac{v^2}{c^2}}}$ (Morse & Ingard, 1968, A). By substituting the coordinates for a moving frame (equations 5.8,5.9,5.10 and 5.11) into equation 5.7 one arrives at

$$\bigtriangledown'^2\, p - \frac{1}{c^2}\frac{\partial^2 p}{\partial t'^2} = s(\gamma(t' + \frac{x'v}{c^2}))\delta(\frac{x'}{\gamma})\delta(y')\delta(z') \tag{5.12}$$

Since the source is moving very slowly compared to the pressure wave field, the term $\frac{x'v}{c^2}$ can be neglected, implying that $t' + \frac{x'v}{c^2} = t' + \frac{x'M}{c} = t'$. By also applying the identity $\delta(\frac{u}{a}) = a\delta(u)$ (Arfken et.al, 2012, C), equation 5.12 is reduced to

$$\bigtriangledown'^2\, p - \frac{1}{c^2}\frac{\partial^2 p}{\partial t'^2} = \gamma s(\gamma t')\delta(x')\delta(y')\delta(z') \tag{5.13}$$

By introducing another coordinate transformation defined by $t'' = \gamma t'$,$x'' = \gamma x'$, $y'' = \gamma y'$ and $z'' = \gamma z'$ equation 5.13 becomes

$$\begin{aligned} \gamma^2 \bigtriangledown''^2\, p - \frac{1}{c^2}\frac{\partial^2 p}{\partial t''^2} &= \gamma s(t'')\delta(\frac{x''}{\gamma})\delta(\frac{y''}{\gamma})\delta(\frac{z''}{\gamma}) \\ \rightarrow \bigtriangledown''^2 p - \frac{1}{c^2}\frac{\partial^2 p}{\partial t''^2} &= \gamma^2 s(t'')\delta(x'')\delta(y'')\delta(z'') \end{aligned} \tag{5.14}$$

where $\bigtriangledown' = \gamma\bigtriangledown''$ has been used. Also, the identity $\delta(\frac{u}{a}) = a\delta(u)$ (Arfken et.al, 2012, C) has again been applied.

As suggested by Morse and Ingard, (1968, A), the solution to equation 5.14 is given by

$$p(r'', t'') = \gamma^2 \frac{s(t'' \pm \frac{r''}{c})}{4\pi r''} \tag{5.15}$$

where $r'' = \gamma r' = \gamma^2 R_1(t)$. Since the solution has now been found in the transformed system, it is only a matter of applying the inverse Lorentz transform to equation 5.15. To simplify the calculation, consider first

$$\begin{aligned} t'' \pm \frac{r''}{c} \\ = \gamma t' \pm \frac{\gamma r'}{c} \\ = \gamma(\frac{t}{\gamma} - \frac{vx'}{c^2}) \pm \frac{\gamma^2 R_1}{c} \\ = t - \frac{\gamma^2 v(x - vt)}{c^2} \pm \frac{\gamma^2}{c}\sqrt{(x - vt)^2 + (1 - M^2)r^2} \end{aligned} \tag{5.16}$$

where $t = \gamma(t' + \frac{vx'}{c^2}) \rightarrow t' = \frac{t}{\gamma} - \frac{\gamma v(x-vt)}{c^2}$ is the inverse Lorentz transform. Rearranging equation 5.16 yields (using $\gamma^2 = \frac{1}{(1-\frac{v}{c}^2)} = \frac{1}{(1-M^2)}$)

$$\begin{aligned} t - \frac{\gamma^2 M(x - vt)}{c} \pm \frac{\gamma^2}{c}\sqrt{(x - vt)^2 + (1 - M^2)r^2} \\ = t - \frac{M(x - vt) \pm \sqrt{(x - vt)^2 + (1 - M^2)r^2}}{c(1 - M^2)} \\ = t - \frac{R(t)}{c} \end{aligned} \tag{5.17}$$

It can be observed that equation 5.17 has an imaginary component in the supersonic case. However, only the subsonic case is of interest since the velocity of the vessel in a seismic survey is much lower than the speed of the wave. The entire Green's function solution can now be written as

$$\begin{aligned} p(r'', t'') = \gamma^2 \frac{s(t'' \pm \frac{r''}{c})}{4\pi r''} \\ \rightarrow p(r, t) = \gamma^2 \frac{s(t - \frac{R(t)}{c})}{4\pi\gamma^2 R_1(t)} \\ = \frac{s(t - \frac{R(t)}{c})}{4\pi R(t)(1 - Mcos(\theta))} \end{aligned} \tag{5.18}$$

where the definition of $R_1(t)$ is given in equation 5.6. Comparing equation 5.18 to equation

2.32 it is clear that they appear similar. What is different is that R(t) in equation 5.18 is time dependent as it moves with a velocity v. However, if the velocity of the source is set to 0 (stationary case), it can be observed that the two equations describe the same pressure wavefield

$$R(t) = \frac{0 + \sqrt{(x-0)^2 + (1-0)r^2}}{(1-0)} = R \tag{5.19}$$

Keep in mind that when v is 0, so is M since $M = \frac{v}{c}$. Thus in the limit of no motion, equation 5.18 takes the form

$$\begin{aligned} p(R,t) &= \frac{s(t - \frac{R}{c})}{4\pi R(1 - Mcos(\theta))} \\ &= \frac{s(t - \frac{R}{c})}{4\pi R(1 - 0 * cos(\theta))} \\ &= \frac{s(t - \frac{R}{c})}{4\pi R} \end{aligned} \tag{5.20}$$

5.2 Modeling a moving source

An equation describing a pressure wavefield emitted by a moving source has now been derived (equation 5.18), and it is time to generate synthetic data using the numerical implementation of that equation.

The simplest modeling case was considered when testing the implementation of a moving source which is the direct wave field. By simply taking a single source and a single receiver, the effects of motion can be isolated when compared to the stationary case. The data was generated using both the numerical implementation of the analytical solution given by equation 5.18, but also by finite difference modeling for quality control. A sketch of the general set up is shown in figure 5.2.

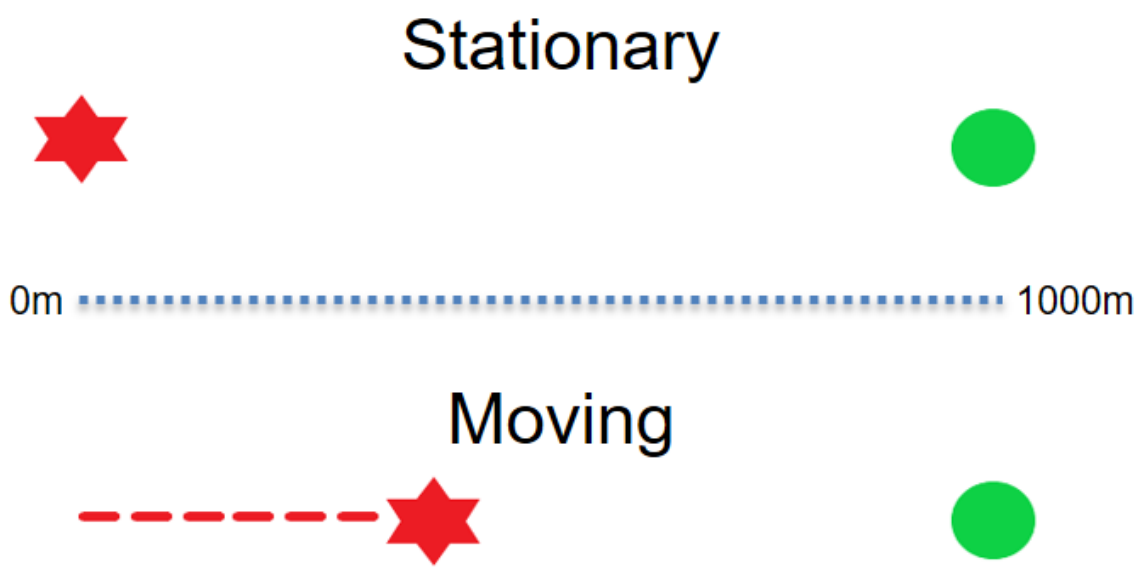

Figure 5.2: Sketch of the direct wavefield experiment. The top half of the figure shows a single stationary source (red) and a single stationary receiver (green). The bottom half of the figure shows a single moving source (red) relative to a single stationary receiver (green).

In the stationary reference experiment a single source is located $1000m$ away from a single receiver as shown in figure 5.2. In the moving source experiment, the source moves at a velocity of $50m/s$ towards the same receiver. The numerical implementation of the latter case involves solving equation 5.18 with the given velocity and initial distance parameters.

The source in the finite-difference modeling, however, simply emits the stationary sweep over a horizontal discretized distance given by the speed of the vessel times the sweep length $50m/s * 5s = 250m$. In this case, the total of $250m$ of motion was discretized into 127 steps. The emitted sweep as implemented in finite-difference is plotted in figure 5.3.

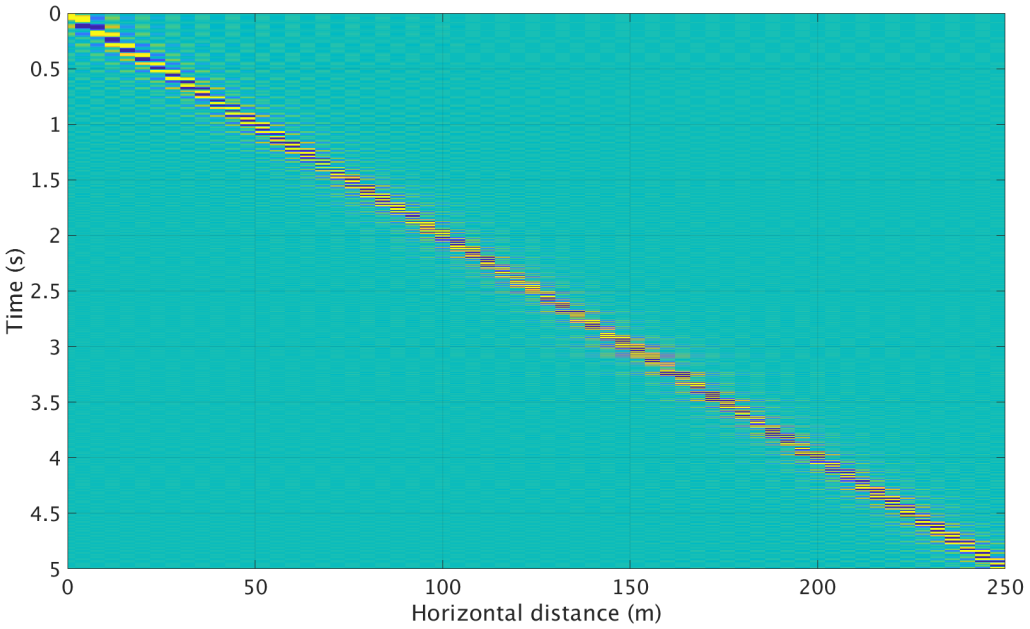

Figure 5.3: The moving source output in finite difference where the sweep is distributed over time and distance.

The velocity of the source has in this simplified case been exaggerated to $50m/s$ to see the effects of motion much more clearly. The result shown in figure 5.4 was obtained utilizing both the numerical implementation of equation 5.18 and by finite difference modeling.

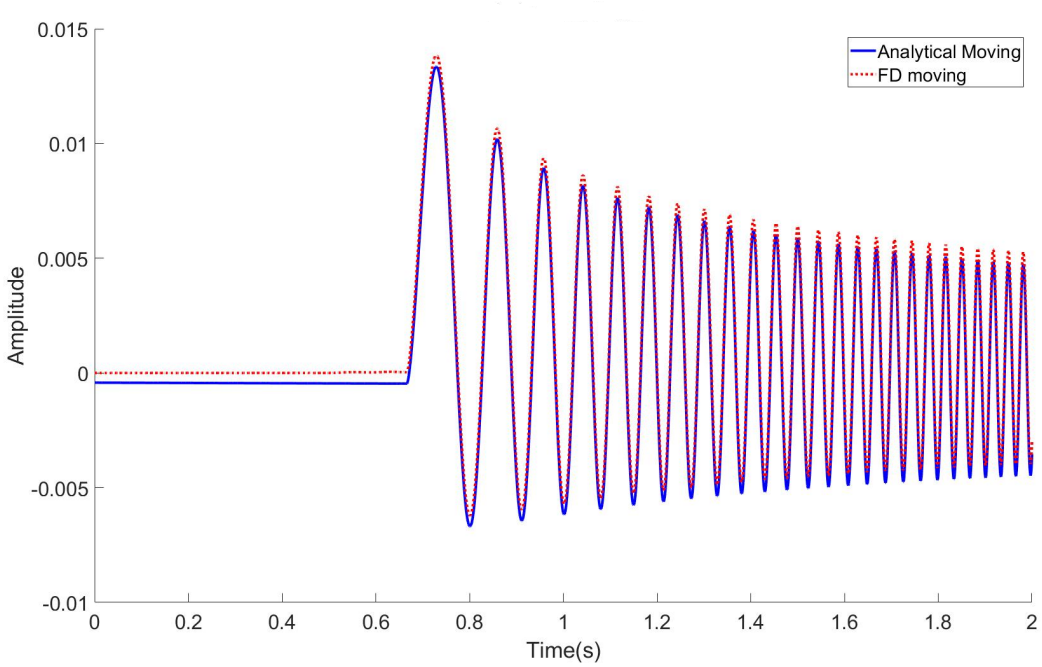

Figure 5.4: The first 2 seconds of the recorded direct wave field with a moving source for both the analytical solution (blue) and the finite difference modeled (red).

As can be observed in figure 5.4, the two approaches yields practically the same result. However, the analytical solution has a DC shift at the very first sample which comes as a consequence of the numerical implementation. This DC shift is not considered a problem since both the finite-difference and analytical data behave in the same manner as seen on figure 5.4.

As the numerical implementation of equation 5.18 and the finite-difference implementation yields practically the same result, it increases our confidence in the modeled source wavefield. It is now time to compare the data generated by a moving source (moving data) to the data generated by a stationary source (stationary data). Thus, we continue our direct wavefield experiment, this time implementing the stationary source as well.

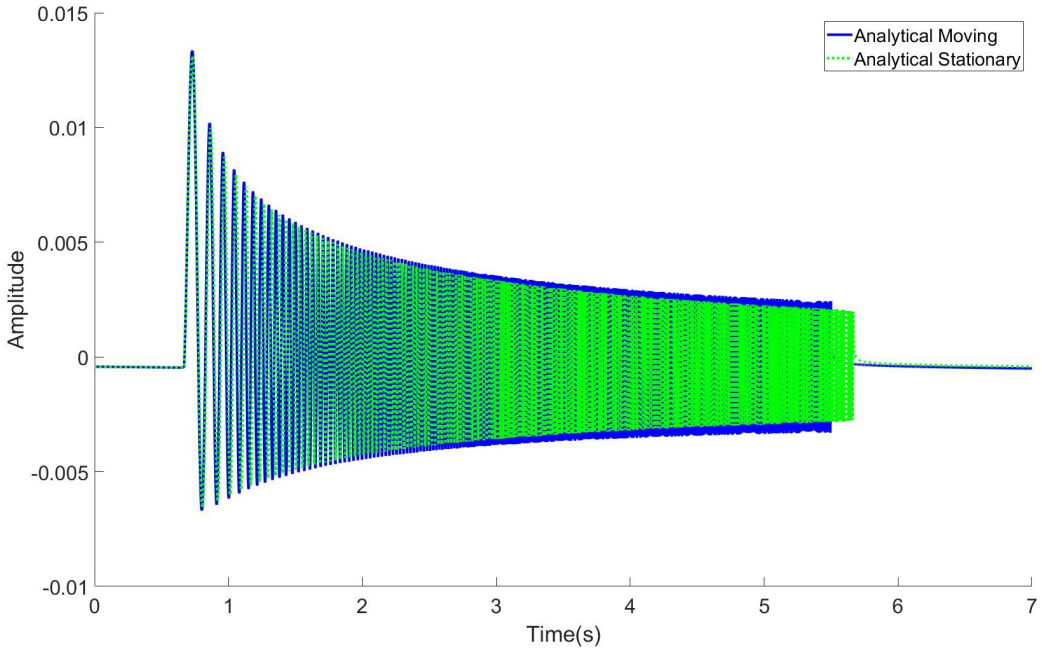

Figure 5.5: Recorded trace of direct wave field for a moving source (blue) and a stationary source (green).

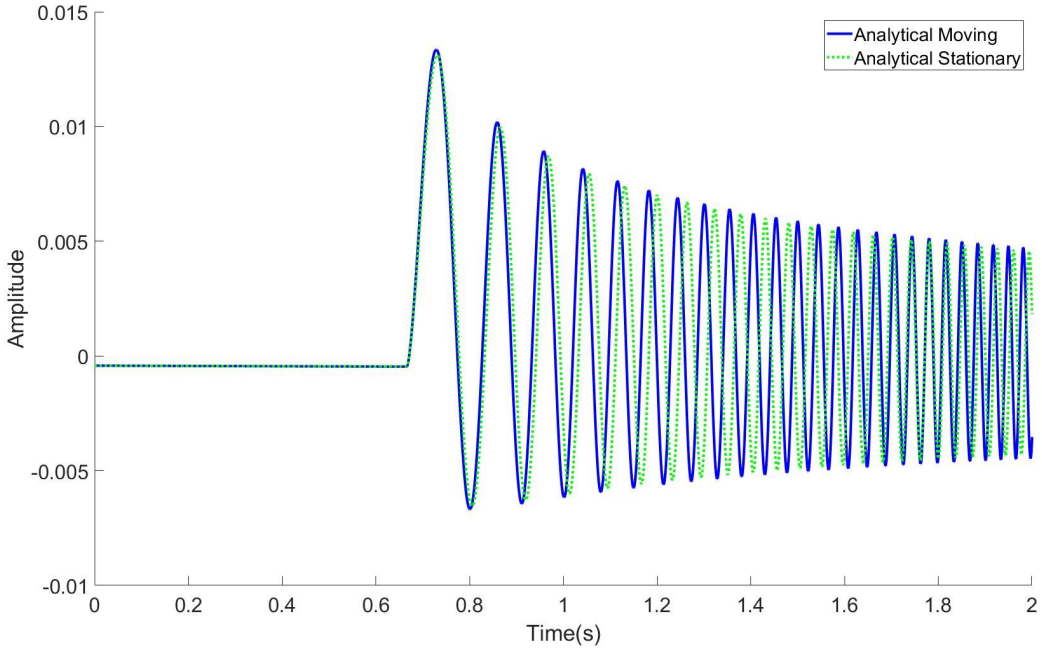

Figure 5.6: Beginning of the recorded trace of the direct wave field for a moving source (blue) and a stationary source (green).

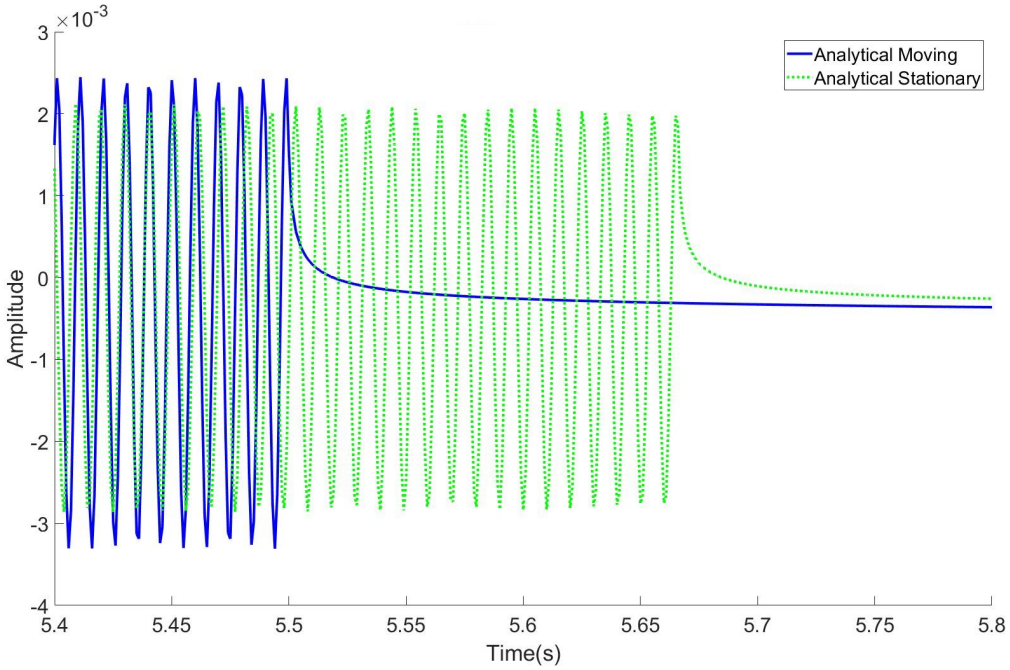

Figure 5.7: End of the recorded trace of the direct wave field for a moving source (blue) and a stationary source (green).

Figure 5.5 show the full recorded trace and figures 5.6 and 5.7 show the beginning and end of the recording respectively. It can be seen from figure 5.6 that the direct wavefields are initially recorded at the same time. This is because the start of the sweep for both the stationary and the moving sources are emitted at the exact same location. The traveltime of the initial output can easily be calculated to $\frac{distance}{velocity} = \frac{1000m}{1500m/s} = 0.667s$ which coincides with figure 5.6.

As the source moves towards the receiver, the two traces start to behave differently. There is a clear phase difference only after a few milliseconds which is a result of the moving source coming closer to the receiver. This can be verified by inspecting the wave equations for both the stationary (equation 2.32) and the moving (equation 5.18) case. The phase term in the frequency domain e^{ikr} when given two different distances would yield different angles of phase as seen on the phase spectrum of the recorded data in figure 5.8.

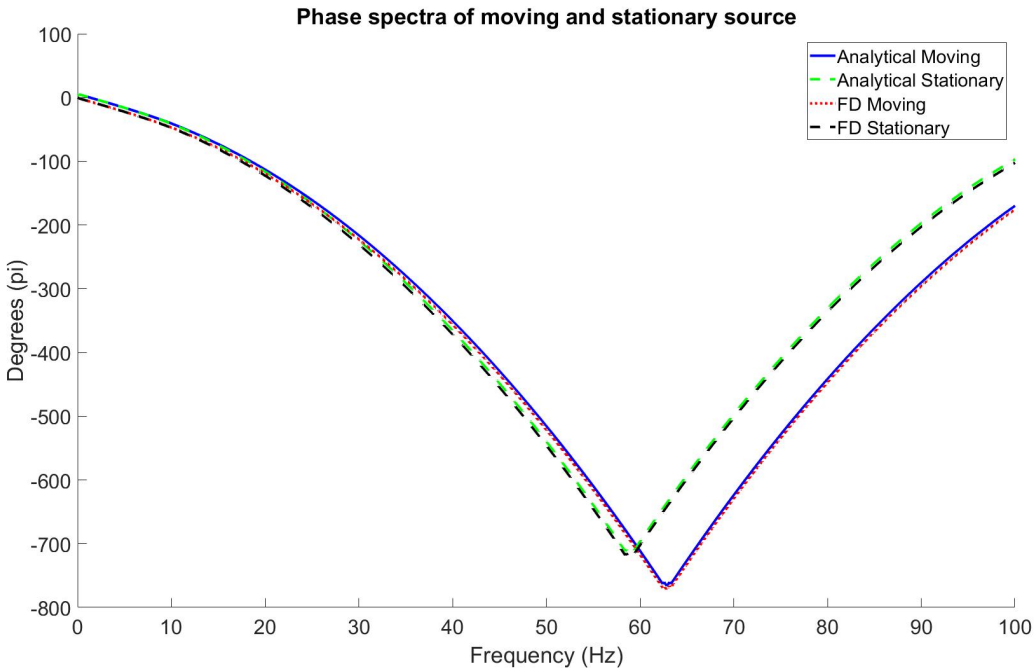

Figure 5.8: Phase spectra of the direct wave field for a stationary and a moving source. Both the FD and analytical approach have been plotted for quality control reasons.

As previously explained, there is little or no phase difference between the stationary and moving source at low frequencies as this corresponds to the beginning of the sweep (linear upsweep) when the moving source is still close to the stationary source. However, at higher frequencies (or additional time), the phases recorded from the stationary and moving source start to deviate. As mentioned, this is because the higher frequencies are emitted when the moving source is closer to the receiver.

It can also be observed from figure 5.7 that there is an amplitude difference between the stationary and moving sources towards the end of the traces. This difference is also due to the moving source getting closer to the receiver as a function of time and therefore has less space to decay.

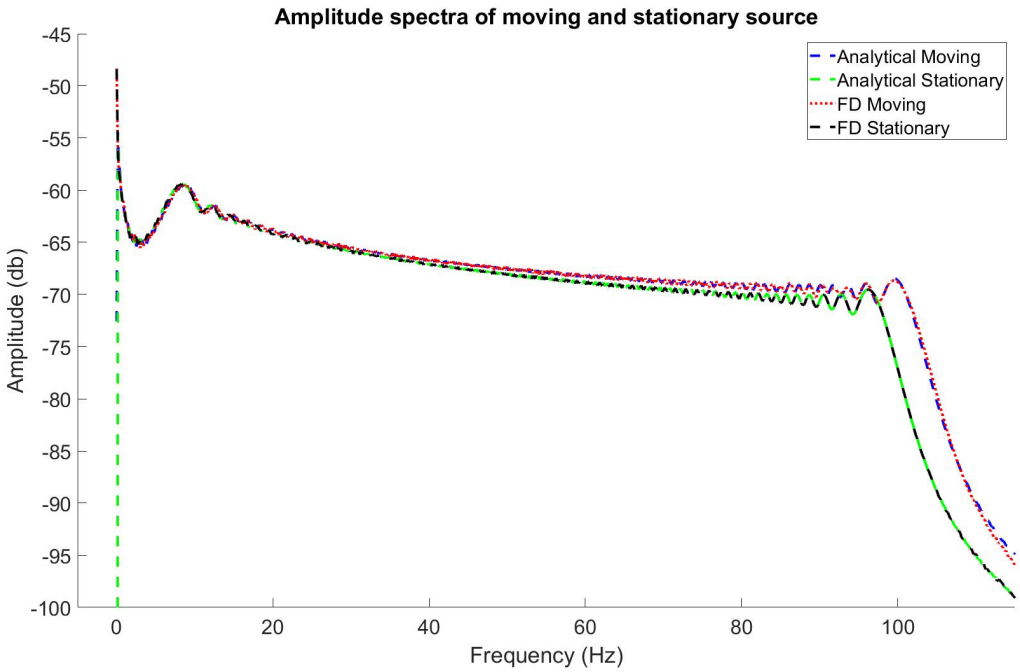

Figure 5.9: Amplitude spectra of the direct wave field for stationary and moving source. Both the FD and analytical approach have been plotted.

Similar to the phase spectrum, the amplitude spectrum (cf. figure 5.9) shows that the amplitudes are similar at low frequencies, but deviates at higher frequencies (later times in the sweep). However, this difference is minor compared to the difference in phase. Moreover, the moving source seems to emit higher frequencies. This is not because the sweeps are different, but because the wavefield is compressed in the direction of motion (and dialated in the opposite direction). When the source is moving towards the receiver at $50m/s$, the wave field compresses which generates higher frequencies. This is the Doppler frequency shift which can be calculated by the following equation (Morse & Ingard, 1968, B)

$$f' = f(\frac{1}{1 \pm \frac{\mathbf{v}}{c}}) \tag{5.21}$$

where plus or minus is chosen whether the motion is towards the receiver (-) or away from the receiver (+). Moreover, f is the original frequency contained within the wave, v is the speed of the source, c is the wave velocity of the medium and f' is the frequency generated by wave field compression or dialation which in our case is (taking $f = 100Hz$)

$$f' = 100Hz(\frac{1}{1 - \frac{50m/s}{1500m/s}}) = 103.45Hz \tag{5.22}$$

The frequency shift is not very large in this case. One would actually expect an even lower shift in reality, as the vessel usually moves at under $3m/s$. This would correspond to a frequency of $f' = 100Hz(\frac{1}{1-\frac{3m/s}{1500m/s}}) = 100.2Hz$. Having the vessel move at such traditional speeds would not give such significant change as in figures 5.8 and 5.9. Thus, the high vessel speed was only employed for the purpose of demonstration. However, from here on, a vessel speed of $2.67m/s$ will be used as this is considered more of a standard. Additionally, only the finite-difference method will be used as we now have increased confidence in the finite difference implementation.

5.3 Generating synthetic data with a moving source

The previous analysis characterized the effects of motion from a direct wavefield as well as introducing motion into the sweep wavelet. In this section, synthetic data is generated using such a sweep along with the same model containing two scatterers (figure 3.4) and the same survey configuration as shown in figure 3.5. However, the source will move towards the right as it is emitting the sweep. When the sweep has finished and the wavefield has been recorded, the next sweep will start to emit at the next shot point location. As previously mentioned, the source will now move at $2.67m/s$ which is considered a more realistic vessel speed.

The data was then processed the same way as with the stationary data (section 4.1) without any motion correction being applied. In fact, we want to test if the moving data can be processed and imaged without taking the motion into account. The processed data for the moving source was then migrated using all 200 shots and the full $3000m$ migration aperture and the result is shown in figure 5.10.

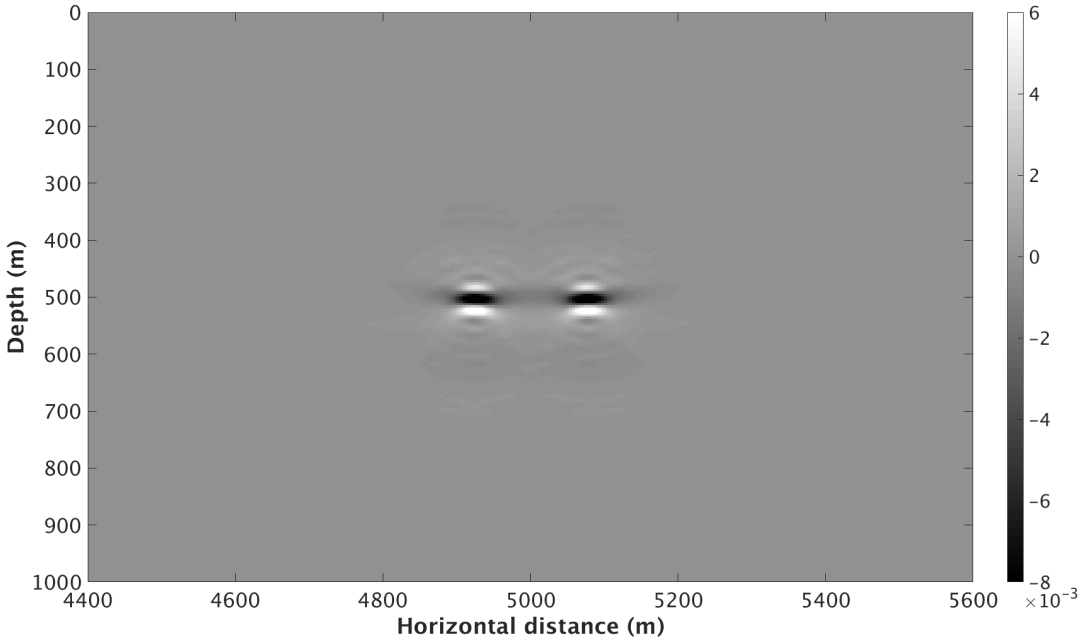

Figure 5.10: Migrated section of moving source data using $3000m$ migration aperture.

When comparing figure 4.10 to figure 5.10, it is hard tell if any differences exist. To obtain a better idea of the image quality, an image slice was again taken at the diffractor depth for both the moving and stationary case (cf. figure 5.11).

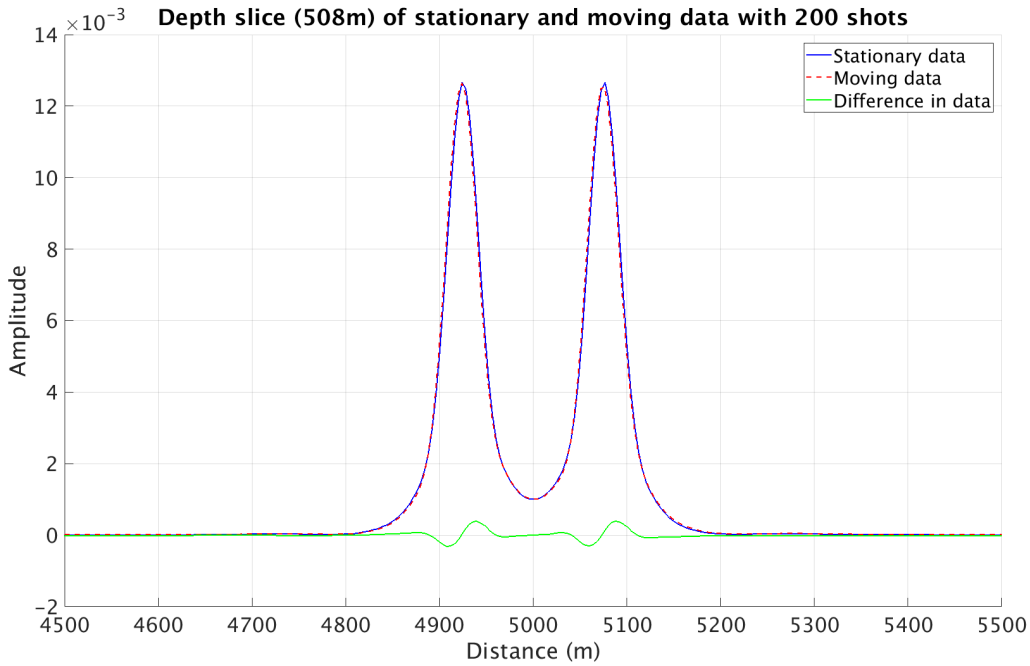

Figure 5.11: Depth slice taken of stationary data (blue) and moving data (red dotted) together with their difference (green) (residual).

Figure 5.11 shows that there is a slight difference in the two images which was calculated to be at most 3.15% with a normalized root mean square (NRMS) of 2.87%. Figures 5.8 and 5.9 provide some basic understanding of how this difference occurs, but this is investigated further in Appendix D.

Chapter 6

Comparing Vibrator and Airgun Data

Two migrated sections have now been obtained using both a moving (figure 5.10) and a stationary (figure 4.10) source emitting a continuous wavefield. To estimate the quality of these images, they will now be compared to the standard airgun case. The chosen airgun in this thesis is a standard PGS airgun array already implemented into Nucleus+. This particular gun array is called 4130G_ 080_ 2000_ 080 where 4130 refers to the volume of the gun given in cubic inches, 8 refers to the source depth and 2000 to the air pressure given in psi. However, the frequency band of this particular airgun is much wider than the vibrator (equation 1.2) so for this to be a fair comparison, the two types of sources have to emit a wavefield containing the same range of frequencies. To achieve this, the airgun was filtered down to only contain frequencies between 5 and 100Hz. Additionally, the airgun was scaled down to the amplitude level of the vibrator. The final airgun source farfield signature used can be seen in figure 6.1.

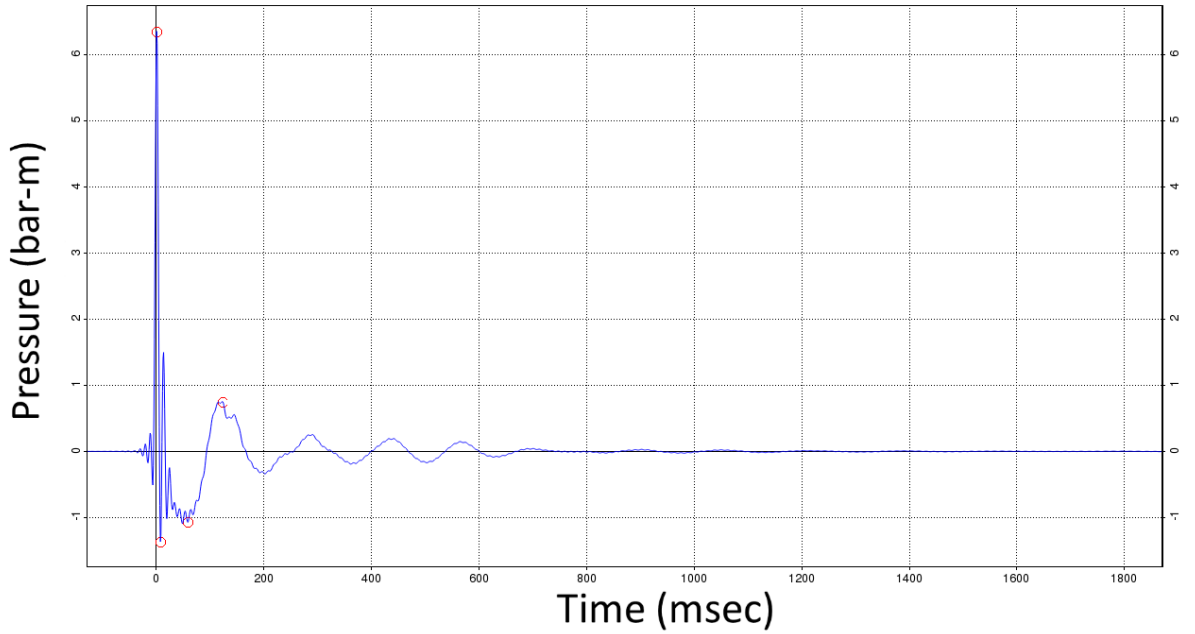

Figure 6.1: The farfield signature of an airgun array recorded $9000m$ away from the actual array.

The corresponding amplitude spectra of the vibrator source and the airgun are shown in figure 6.2.

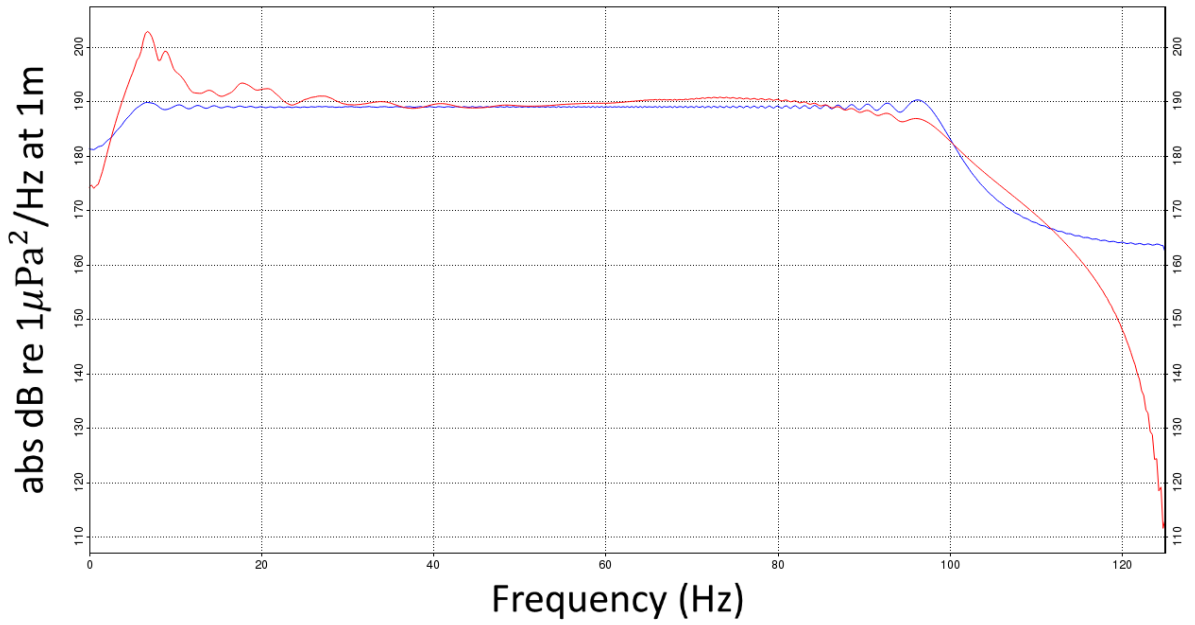

Figure 6.2: Comparison of the amplitude spectrum of the airgun (red) with that of the vibrator (blue).

It can be observed from figure 6.1 that the output from the airgun is not a perfect impulse (i.e. it contain the bubble pulse). However, we indent to preserve the inherent nature

of the airgun array signature. Thus, some of the bubble pulse still remains within the signature.

The farfield signature represents the propagation distance when the source signature starts to be stationary ($9000m$ in this case). In order to find the actual output, or the notional source signature, the farfield signature in figure 6.1 was propagated back to the position of the source thus compensating for geometrical spreading and phase. This notional signature was then used to generate synthetic data the same way as shown in section 3.2 with the same survey configuration (figure 3.5) and the same model (figure 3.4).

The data was then migrated using the same finite-difference depth migration as previously used and the result is shown in figure 6.3.

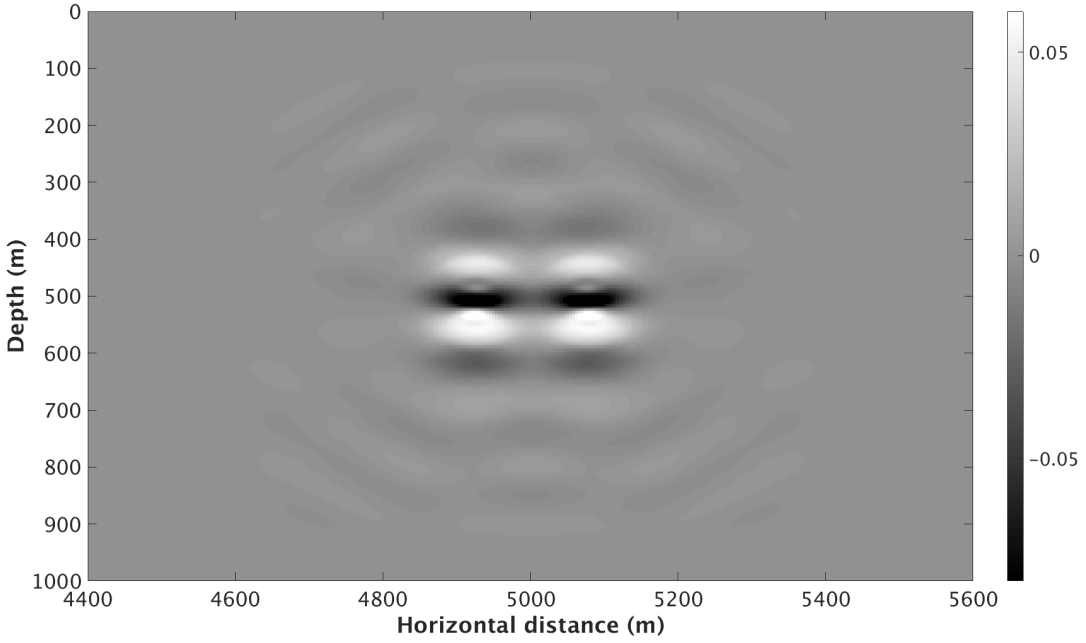

Figure 6.3: Migrated section of airgun data using $3000m$ migration aperture.

It can be observed from figure 6.3 that the image is blurry in comparison to the image produced using a marine vibrator (figures 4.10 and 5.10). However, the two diffractors are still properly resolved. To get a better comparison, an image slice at the diffractor location was taken and is displayed in figure 6.4 together with the results obtained in case of sweep data (both stationary and moving source).

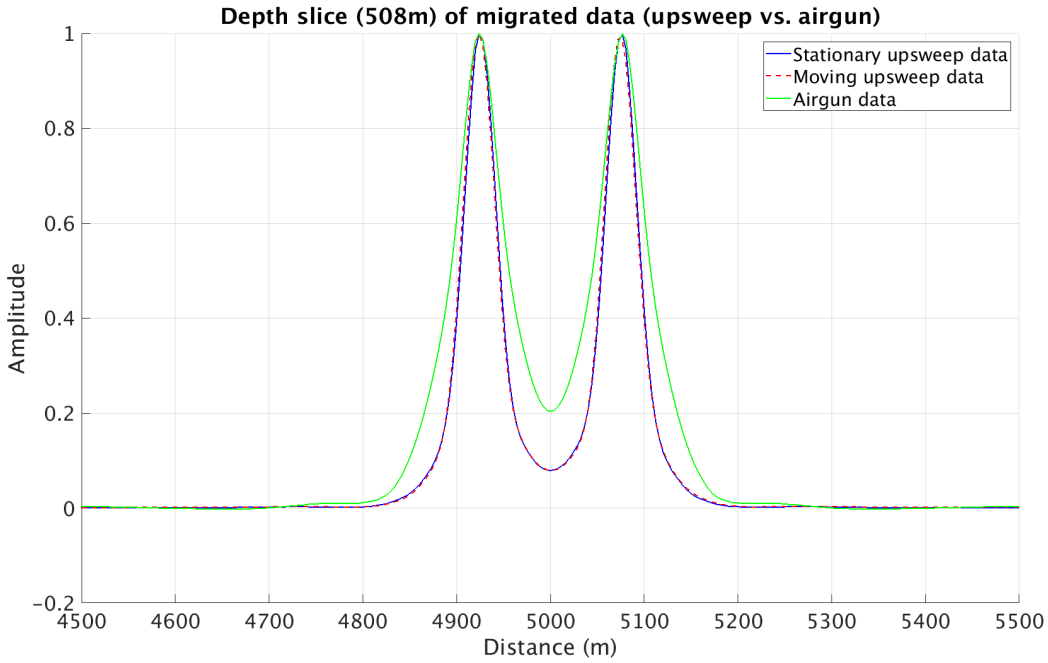

Figure 6.4: Normalized amplitude image slice taken of the migrated section in figure 6.3 at a depth of $508m$.

The amplitudes shown in figure 6.4 have been normalized in order to obtain a better comparison. It can be observed from figure 6.4 that the airgun data is not resolving the two diffractors as well as both the moving and stationary vibrator data. This may come as an effect of the low frequencies being the most dominant in the airgun signature (figure 6.2). A better comparison could be obtained by applying designature and including noise in the computed data. However, no designature or additional signature alterations will be considered in this work as the main point was to show that both source types are able to generate data with sufficient energy and frequency output in order to resolve the two diffractors.

Chapter 7

Discussion

7.1 Frequency dependent illumination

Only a single-source firing system has been considered in this work. In the stationary case, this single source emits frequencies that all originate from the same source location. Therefore, all frequencies illuminate the same areas of the subsurface. When motion is introduced however, different frequencies will illuminate different parts of the subsurface as the source changes its position with time. This is not a practical problem for the sweep length and vessel speed used in this thesis work. But, long sweep lengths and/or high vessel speeds will cause different points in the subsurface to be illuminated by different frequencies.

Assume now a single vibrating source emitting a linear upsweep which is recorded by a single receiver both located above a plane interface. The receiver is stationary while the source moves at $2.67 m/s$ towards the receiver emitting a sweep over 5 seconds. The largest difference in midpoints caused by the motion can then be shown to be 6.675 meters. In order for the midpoint to vary significantly at these vessel speeds, the sweep length have to be extremely long. If the same experiment were to be repeated with a sweep length of 20 seconds, the difference in midpoints on the plane interface would be 26.7 meters.

Large differences in midpoint location may introduce further problems when the wave propagates down into the subsurface beneath the plane interface. If the underlying layer includes strong lateral velocity variations, different frequencies will propagate with dif-

ferent wave velocities. This may imply that the traveltimes for different frequencies vary disproportionally to the propagation distance. More specifically, one frequency may propagate in a high velocity part of a layer while another frequency may propagate in a lower velocity part of the same layer. The underlying layer may therefore be illuminated by different frequencies giving the wrong impression of the extent of that layer. This may be critical when trying to locate typical thin layers like cap rocks. If the extent of the cap rock is underestimated due to different resolution in different parts of the section, a potential reservoir may go unnoticed. Furthermore, this effect may echo throughout the subsurface thus having data resolved partly by different frequencies.

Different propagation paths for different frequencies means they are recorded at different times disproportional to the propagation distance. The time difference in recording the lowest and highest frequencies (assuming linear upsweep) emitted by the vibrator is then given by the sweep length plus the additional traveltime caused by lateral velocity variations. This additional traveltime can either be negative or positive depending on the direction of the lateral velocity gradient and the direction of motion of the source.

A type of lateral velocity variations are dipping reflectors. The next section will discuss how such a dipping reflector affects the data with regards to the Doppler effect.

7.2 The Doppler effect and dipping reflectors

It has been shown in figure 5.11 in section 5.3 that the effects of motion on the source wavefield is minimal when moving at typical vessel speeds ($< 3m/s$). This is further explored in Appendix D where the amplitude ratio in common receiver domain (CRD) is shown to be very small as well. However, a phase difference of over 300 degrees between the stationary and moving data prior to cross-correlation at high frequencies and large offsets is shown in figure D-3. As described by Dragoset (1988), the Doppler effect arise from the compression or dilation of the wavefield thereby generating higher frequencies or lower frequencies respectively. Even a small frequency shift of less than 1Hz will cause a large phase distortion (Dragoset, 1988). Dragoset then proposed an equation to calculate the phase shift resulting from the Doppler effect:

$$\phi(f) = 360^{\circ}\delta T \frac{f^2}{(f_2 - f_1)} \tag{7.1}$$

where T is the sweep length, f is a given frequency within the frequency band, f_2 and f_1 is the highest and lowest frequency within that frequency band respectively and δ is the Doppler factor. This Doppler factor is the ratio of vessel speed and the velocity of the medium, but also contain angle information and is given as $\delta = \frac{v}{c}[sin(\alpha_r) - sin(\alpha_s)]$. Where α_r and α_s are the angles of incidence of the receiver and source respectively. From this equation it is observed that the Doppler factor is 0 when the angles of incidence are equal for both source and receiver. This only happens for the zero-offset trace on a common receiver gather when using the middle receiver with the model and survey configuration used in this thesis work. Therefore, it can be seen on figure D-3 in Appendix D that the zero offset trace has a zero degree phase shift. This is confirmed on figure D-1 in Appendix D where there is no difference between the stationary and moving datasets at zero offset. Furthermore, the difference between these two angles in our case increase as the shot point deviates from the receiver location meaning that higher offset would yield a higher Doppler factor and phase shift which is confirmed in figure D-3. The Doppler factor can be calculated to be ± 0.0017 for the largest offset using the survey configuration

and model in this work. Substituting the values used in this thesis work into equation 7.1 yields

$$\phi(f) = 360° * (\pm 0.0017) * 5s * \frac{100Hz^2}{(100Hz - 5Hz)} \approx \pm 322.1° \tag{7.2}$$

where $f_1 = 5Hz$, $f_2 = 100Hz$ and $f = 100Hz$ has been used. With the values for maximum offset and frequency used, this corresponds well to what is seen at the bottom left and right in figure D-3.

It can be observed from equation 7.1 that a stationary source yields a Doppler factor of zero meaning a zero degree phase shift. Even a small velocity such as the one used here ($2.67m/s$) will yield a phase shift of several hundred degrees. Additionally, a plane reflector will experience no Doppler phase shift as the angles of incidence are equal.

The two-diffractor model used in this work limits the ability to see the effects introduced by complex geology, but dipping reflectors will according to equation 7.1 cause the Doppler effect to increase as the difference in angles of incidence increase (Dragoset, 1988). However, the phase of the sweep will be removed from the dataset when cross-correlation is performed, thereby eliminating these Doppler phase shift effects.

It can be seen from equation 7.1 that increased sweep length will result in an increase of the Doppler phase shift. The next section will discuss the advantages and disadvantages of having a shorter sweep length.

7.3 Sweep length and deep targets

Short sweep lengths produce lower pressure output than longer sweeps. This is because the longer sweep would "dwell" longer on each frequency, creating more pressure output per frequency according to equations 2.31 and 3.4. This allows the pressure wave to propagate to deeper targets before being too attenuated. As previously discussed in section 7.1 however, long sweep length cause frequency dependent illumination of the subsurface. This means that only parts of the deeper subsurface will be illuminated as the higher frequencies will attenuate faster. Thus, long sweeps can only illuminate parts of the deep targets in areas where the low frequencies will propagate.

However, it is not of interest to obtain the highest pressure output possible, but to do so while under some given threshold which is set according to environmental regulations. While under this threshold, the pressure output should be maximized. According to MV-JIP (section 1.4), this threshold is set to $200dB$ re. $1\mu Pa/Hz$ @ $1m$ for $10-100Hz$ for a 5 second signal (Feltham et. al., 2018). This value means that each frequency in the band is only allowed to contain $200dB$ of pressure relative to reference level of 1 micro Pascal when measured 1 meter away from the source. Obtaining $200dB$ per frequency is in theory possible for both an airgun and a marine vibrator (figure 6.2). It is therefore important to see how the amplitudes are distributed in time. The amplitude and frequency content of the airgun is contained within a short period of time (see figure 6.1), while the marine vibrator is spreading this amplitude over a longer period of time. Therefore, the airgun is considered more dangerous to marine life as all of this energy is concentrated into a single wavefront (in the ideal case). In other words, the peak amplitude of the airgun is much higher than that of the marine vibrator.

It may be possible to increase the total pressure output from short sweeps by introducing a multi-vibrator system, thereby avoiding the disadvantages of having a longer sweep length. How several marine vibrators each emitting shorter sweeps can be utilized will be the topic of the next section.

7.4 Multi-vibrator systems

Until now, it has been discussed how short sweeps are preferred in order to avoid a section partly illuminated by different frequencies. However, these short sweeps have lower pressure output than the longer sweeps, making deep surface resolution impossible due to attenuation. This section will discuss how multiple vibrator sources emitting shorter sweeps may be utilized to obtain a higher pressure output while keeping a shorter sweep length. Additionally, having multiple vibrator shooting simultaneously lowers survey cost as more data can be collected.

When multiple sources are introduced into a survey, it increases the pressure output equal to the number of sources (in the ideal case). However, it is a challenge to separate the signals recorded by the receivers. The process of signal separation is called deblending and is well understood when it comes to airgun sources. However, deblending for marine vibrator sources are performed differently from what is done in the airgun case. Marine vibrator deblending takes advantage of knowing the output of the source as well as the ability to encode the sweep.

A coded sweep is a type of sweep that consists of smaller sequentially ordered sub-sweeps. The number of sweep types within a coded sweep are often referred to as code-members. A binary coded sweep consists of two code members which could be upsweeps and downsweeps (Bernhardt & Peacock, 1978). Phase encoded sweeps are often used for deblending purposes as well as increasing the signal to noise ratio which further act to suppress the noise associated with the cross-correlation process (Bernhardt & Peacock, 1978). Furthermore, it has been shown that a sub-sweep length of 1 second yields good results when suppressing such correlation noise (Edelmann & Werner, 1982). However, the longer the entire coded sweep (i.e. more sub-sweeps) the better the suppression of noise in the cross-correlation process. The sub-sweeps within a coded sweep can in theory be chosen freely such that the sub-sweeps all contain the same frequencies. Another options would be to have the sub-sweeps have different frequency bands, possibly with overlapping frequencies.

A method utilizing phase encoded sweeps for deblending purposes was proposed by Silverman (1979). This type of configuration aims to obtain two shot gathers from two different vibrators each emitting a phase encoded sweep of different polarities (Silverman, 1979). Due to the harmonic interference of the Silverman configuration, another configuration proposed by Ward et al. may be considered. This configuration expands upon the Silverman configuration by adding additional sub-sweeps, with a 45° phase shift between the sub-sweeps, to the coded sweeps for both vibrator sources, but with the direction of phase shift reversed for the second source. This configuration has proved to suppress all lower order harmonics up to the seventh harmonic (Ward et al., 1990).

Most marine vibrator deblending methods rely on a phase difference between the output from different vibrator sources, but some deblending methods does not rely on the sweep to be coded. These methods simply lets the initial phase of non-coded sweeps to vary from shot to shot. Halliday et al. (2017) proposed such a method where six shots with a 60° phase shift for each source is recorded, sorted into a common receiver gather (CRG) and then transformed to frequency-wavenumber domain. By utilizing this phase difference separation, the deblending yielded less cross-talk than using a simple time-dithered separation method (Halliday et al., 2017). This example shows how valuable the control of the source signature is when trying to deblend the data. Moreover, this means that it is possible to perform surveys using multiple sources which makes it possible to illuminate deeper targets as well as saving both time and money.

The Halliday deblending method does not imply that any specific type of sweep is needed and therefore opens up for different types of sweeps to be used within the same survey. This would imply that the benefits of several types of sweeps may be utilized in a multi-vibrator system. Moreover, high pressure output may not be necessary if the target area is shallow thereby eliminating the need for a multi-vibrator system. The next section will discuss how marine vibrators may be utilized in shallow waters.

7.5 The marine vibrator in shallow waters

Airgun sources in marine surveys are usually placed at some depth below the sea surface in order to minimize loss of energy. If the airgun source is placed at too shallow depth, most of the energy will simply disappear into the air above. However, even at an optimal depth, some of the energy will still propagate upwards and be reflected off the sea surface and create the source ghost. The deeper the airgun source is fired, the larger the difference in traveltimes between the primary reflection and the source ghost itself, thus loosing resolution.

The marine vibrator does not suffer to the same degree as the airgun when it comes to depth limitations. As described in section 1.6, the AquaVib marine vibrator by GeoMechanics can handle depths down to 1m below the sea surface, thereby making it possible to handle very shallow prospects. Smith et.al. have shown that the output from the Industrial Vehicles International marine vibrator is independent for depths between 8 and 1.5m. Shallower depths than 1.5m gave rise to amplitude loss on the scale of $3 - 6dB$ (Smith et. al., 1998). A test of a marine vibrator engineered by Total, Mobil and Geco-Prakla in 1994 showed that the marine vibrator was able to produce sufficient output down to 1m depth. However, it was also shown that the source ghost dominated the data for sources located closer to the sea surface (Walker et. al, 1996). Walker et. al. showed that a simple ghost filter could remove the effects of such a source ghost. Overall, it is safe to say that the marine vibrator can operate at shallower waters than the airgun making them a good alternative in such areas. This would make it possible to survey areas closer to the shore as these areas are often shallow.

It just so happens that the shallower waters tend to have the most sensitive marine life (Archer, 2017). The lower peak pressure output of the marine vibrator in combination with the ability to operate at shallower waters makes the marine vibrator a good candidate for the choice of source in these areas.

Chapter 8

Conclusion and Future Work

This work has shown that a term for the pressure output from a pair of vibrating plates within a homogeneous medium can be derived (equation 2.31). A term for the moving source wavefield was derived as well (equation 5.18). From these two equations it has been shown that the acceleration of the plates are directly related to the pressure output and can in theory be configured to emit any frequency band using any sweep length (Appendix C). However, the choice of sweep length must be chosen carefully as very long sweeps length will result in a section partly resolved by different frequencies at different depths.

The introduction of motion upon the vibrator source has been showed to cause small amplitude differences, but large phase shifts which is caused by a Doppler effect (figures D-2 and D-3). However, the process of cross-correlating the synthetic data with the stationary sweep wavelet has shown to be an effective procedure to remove the phase of the sweep thereby making the data interpretable. Moreover, is has been shown that the data generated using a moving source can be treated equally to a stationary source in the ideal case presented in this thesis work (figure 5.11).

As a result of the choice of background model used in this work (figure 3.4), we are not able to see the effects that complex geology and a non-impulsive source wavefield have on the data. Therefore, a new model containing more complex geology like dipping reflectors alongside other reflection events should be made in order to investigate further. If the data generated using a moving source can still be treated as a stationary case, it can be

concluded that the effect of motion is corrected for by the cross-correlation and migration process. Additionally, it may be possible to perform this cross-correlation in the migration itself by utilizing a cross-correlation imaging condition.

The limit of resolution for a marine vibrator has also been tested where the generated synthetic data for the stationary case has been cross-correlated and migrated using different migration apertures (figure 4.6). The results shown in figure 4.7 does not correlate with values in equation 4.7, however, it was demonstrated that a marine vibrator source was able to resolve two different points separately.

Finally, synthetic airgun data was generated using a filtered airgun source signature. The generated data was then migrated and the image was then compared to the marine vibrator image. The main difference between these two images was that the lower frequencies dominated the airgun image, thereby making it seem more blurry. However, both types of sources are able to generate an image that easily resolved the two nearby diffractors. What can be done further is to deconvolve the wavelet from the data which should give a closer resemblance to the true amplitude of the reflection events. This would make for a more complete comparison of the marine vibrator and the airgun than what is shown in chapter 6.

References

- Archer, J, 2017, *A safe alternative to the seismic airgun*, offshore technology, [Internet], Available from: https://www.offshore-technology.com/features/featurea-safe-alternative-to-the-seismic-airgun-5834997/

- Arfken, G., B., Weber, H., J., Harris, F., E., 2012, A, *Mathematical Methods for Physicists*, chapter 3, 7th edition, Academic Press: Elsevier Inc., pp 164, ISBN: 978-0-12-384654-9

- Arfken, G., B., Weber, H., J., Harris, F., E., 2012, B, *Mathematical Methods for Physicists*, chapter 10, 7th edition, Academic Press: Elsevier Inc., pp 448, ISBN: 978-0-12-384654-9

- Arfken, G., B., Weber, H., J., Harris, F., E., 2012, C, *Mathematical Methods for Physicists*, chapter 1, 7th edition, Academic Press: Elsevier Inc., pp 78, ISBN: 978-0-12-384654-9

- Berkhout, A.J., 1980, *Seismic Migration, imaging of acoustic energy by wave field extrapolation*, Appendix C: Wave Equation for Inhomogeneous Fluids, 355 Jan van Galenstraat: Elsevier Scientific Publishing Company, pp. 320-325

- Bernhardt T., Peacock J. H., 1978, *Encoding Techniques for the Vibroseis* System***, Geophysical Prospecting 26, pp. 184-193, DOI: https://doi.org/10.1111/j.1365-2478.1978.tb01585.x

- Dragoset, W., H., 1988, *Marine vibrators and the Doppler effect*, Geophysics, 1988, Vol.53(11), pp.1388-1398, DOI: 10.1190/1.1442418

- Edelmann, H., A., K., Werner, H., 1982, *Combined Sweep Signals for Correlation Noise Suppression**, Geophysical Prospecting, Vol.30(6), pp 786-812, DOI: 10.1111/j.1365-2478.1982.tb01339.x

- Emma Technologies, *Seismic*, [Internet], Available from: https://www.emma-technologies.com/products/seismic/

- Feltham A., Jernerson M., Henderson N., Girard M., Nechayuk V., Cozzens A., 2018, *Geophysical Testing of a Marine Vibrator Integrated Projector Node (MV-IPN) at Seneca Lake*, 80th EAGE Conference and Exhibition, DOI: 10.3997/2214-4609.201800996

- Halliday D. F., Laws R., Özbek A., Schlumberger Gould Research, 2017, *Phase sequencing, marine vibrators, and high-multiplicity simultaneous sources*, Society of Exploration Geophysicists, DOI: https://doi.org/10.1190/segam2017-17660035.1

- Hampson G., Jakubowicz H., 1995, *The effects of source and receiver motion on seismic data*, Geophysical Prospecting, Vol.43(2), pp.221-244, DOI: 10.1111/j.1365-2478.1995.tb00133.x

- Howell, K., B., 2001, A, *Principles of Fourier Analysis*, CRC Press; 1 edition (May 18, 2001), pp 755-756, ISBN: 0849382750

- Howell, K., B., 2001, B, *Principles of Fourier Analysis*, CRC Press; 1 edition (May 18, 2001), pp 395, ISBN: 0849382750

- Innoseis, 2018, *Seismic Surveys*, [Internet], Available from: http://www.innoseis.com/seismic-surveying/

- International Association of Geophysical Contractors, 2002, *Airgun Arrays and Marine Mammals*, 2550 North Loop West, Suite 104, Houston, Texas 77092 USA

- Kadry, S., 2014, *Mathematical Formulas for Industrial and Mechanical Engineering*, Elsevier Scientific Publishing Company, pp 60, ISBN: 978-0-12-420222-1

- Kallweit, R., S., Wood, L., C., 1982, *The limits of resolution of zero-phase wavelets*, GEOPHYSICS, Vol.47(7), pp 1035-1046, DOI: 10.1190/1.1441367

- Kramer, F. S., Peterson, R.A., Walter, W.C., 1969, *Seismic Energy Sources*, Offshore Technology Conference, 18-21 May, Houston, Texas, DOI: https://doi.org/10.4043/1119-MS

- Landrø, M., Amundsen, L., 2014, *Is it optimal to tow air guns shallow to enhance low frequencies?*, Geophysics, Vol.79(3), pp.13-18, DOI: 10.1190/GEO2013-0348.1

- Morse, P., M., Ingard, K., U., 1968, A, *Theoretical Acoustics*, New-York, McGraw-Hill Book Company , pp 717-724, ISBN: 0070433305

- Morse, P., M., Ingard, K., U., 1968, B, *Theoretical Acoustics*, New-York, McGraw-Hill Book Company, pp 699, ISBN: 0070433305

- Nguyen, D., L., 2017, *Seismic Wavefield Modelling From Marine Vibrator Sources*, Department of Geosciences, Faculty of Mathematics and Natural Sciences, University of Oslo

- Parkes, G., Hatton, L., 1986, *The marine seismic source*, Dordrecht, Springer Netherlands : Imprint: Springer, ISBN: 94-017-3385-6

- Peters, A., S., Stoker, J., J., 1954, *A uniqueness theorem and a new solution for Sommerfeld's and other diffraction problems*, Communications on Pure and Applied Mathematics, Vol.7(3), pp 565-585, DOI: https://doi-org.ezproxy.uio.no/10.1002/cpa.3160070307

- PGS, 2017, *Marine Vibrators Get Closer to Reality*, [Internet], Available from: `https://www.pgs.com/publications/feature-stories/marine-vibrators/`

- Rietsch E., 1977, *Computerized Analysis of Vibroseis Signal Similarity*, Geophysical Prospecting, Vol.25(3), pp 541-552, DOI: 10.1111/j.1365-2478.1977.tb01186.x

- Roy D., Brideau C., Lawry T., Ratliff C., Rekos R., 2018, *The Applied Physical Sciences Marine Vibrator: An Overview*, 80th EAGE Conference and Exhibition, DOI: 10.3997/2214-4609.201801625

- Salby, M., L., 2012, *Physics of the Atmosphere and Climate*, Cambridge University Press, Appendix D: Vector Identities, pp 620, DOI: https://doi-org.ezproxy.uio.no/10.1017/CBO9781139005265.024

- Silverman, D., 1979, *Method of Three Dimensional Seismic Prospecting*, United States Patent 4,159,463

- Smith, J., G., Jenkerson, M., R., Mobil Exploration, Producing Technical Center, 1998, *Acquiring and Processing Marine Vibrator Data in the Transition Zone*, Society of Exploration Geophysicists, DOI: http://dx.doi.org/10.1190/1.1820159

- Söllner, W., Orji, O., 2017, *Marine vibrator source acceleration and pressure*, US Patent Application, Pub. No. US2018/0052245 A1

- Todoeschuck, J., P., Jensen, O., G., 1989, *Scaling geology and seismic deconvolution*, Pure and applied geophysics: Volume 131, Issue 1-2, pp 273-287, DOI: 10.1007/BF00874491

- Walker, L., Potter, G., Jenkerson, M., Rodriguez, J., M., Total Research and Technology Center, 1996, *The acoustic output of a marine vibrator*, Society of Exploration Geophysicists, DOI: http://dx.doi.org/10.1190/1.1826485

- Ward, R. M., Brune, R.H., Ross, A., Kumamoto, L. H., 1990, *Phase encoding of Vibroseis signals for simultaneous multisource acquisition*, 60th Annual International Meeting, SEG, Expanded Abstracts, pp. 938-941

- Western Geco, 2010, Geo ExPro Vol. 7 No. 1, [Internet], Available from: https://www.geoexpro.com/magazine/vol-7-no-1

Appendixes

Appendix A: Derivation of Euler's equation of motion

Consider an infinitesimal fluid volume and let it interact with a propagating pressure field as shown in figure A-1.

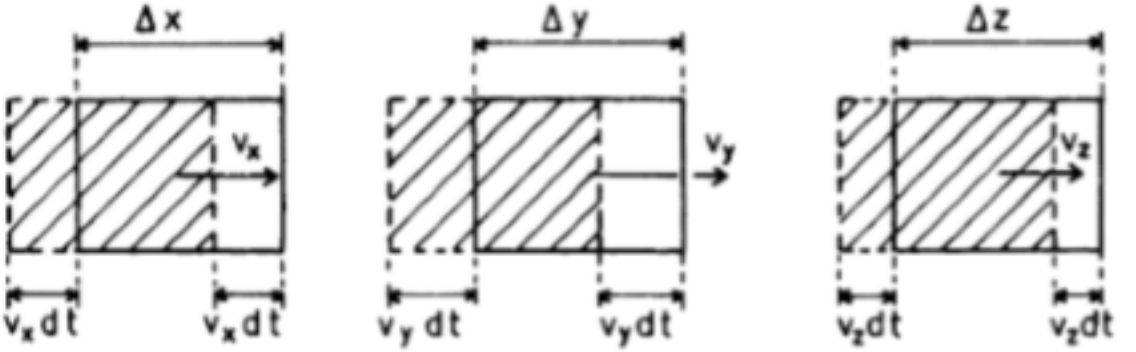

Figure C.2: At time t + dt the mass Δm is situated at (x + $v_x$dt; y + $v_y$dt; z + $v_z$dt).

Figure A-1: Translated infinitesimal fluid element (Berkhout, 1980).

This implies compression and expansion as well as translation of the fluid element. The acting forces can be written as:

$$\begin{aligned} F_x &= (\frac{\partial p}{\partial t}dt + \frac{\partial p}{\partial x}\Delta x)\Delta y\Delta z = \frac{\partial p}{\partial x}V \\ F_y &= (\frac{\partial p}{\partial t}dt + \frac{\partial p}{\partial y}\Delta y)\Delta x\Delta z = \frac{\partial p}{\partial y}V \\ F_z &= (\frac{\partial p}{\partial t}dt + \frac{\partial p}{\partial z}\Delta z)\Delta x\Delta y = \frac{\partial p}{\partial z}V \end{aligned} \tag{A-1}$$

or in vector form (assuming $dt \to 0$)

$$\mathbf{F} = V \bigtriangledown p \tag{A-2}$$

In equation A-1 Δx, Δy and Δz denote the three surface areas of the fluid element and V is the volume of the fluid element. Note that the observation time dt in equation A-1 is assumed so small that the pressure change over time can be neglected.

Considering the same fluid element, the acceleration term may also be decomposed into time and spatial components employing the total derivative $d\mathbf{v}$ ($\mathbf{v}$ being velocity):

$$\begin{aligned} d\mathbf{v} &= \frac{\partial \mathbf{v}}{\partial t}dt + \frac{\partial \mathbf{v}}{\partial x}\Delta x + \frac{\partial \mathbf{v}}{\partial y}\Delta y + \frac{\partial \mathbf{v}}{\partial z}\Delta z \\ \rightarrow \frac{d\mathbf{v}}{dt} &= \frac{\partial \mathbf{v}}{\partial t}\frac{dt}{dt} + \frac{\partial \mathbf{v}}{\partial x}\frac{\Delta x}{dt} + \frac{\partial \mathbf{v}}{\partial y}\frac{\Delta y}{dt} + \frac{\partial \mathbf{v}}{\partial z}\frac{\Delta z}{dt} \\ &= \frac{\partial \mathbf{v}}{\partial t} + \frac{\partial \mathbf{v}}{\partial x}v_x + \frac{\partial \mathbf{v}}{\partial y}v_y + \frac{\partial \mathbf{v}}{\partial z}v_z \\ &= \frac{\partial \mathbf{v}}{\partial t} + (\mathbf{v} \cdot \bigtriangledown)\mathbf{v} \end{aligned} \tag{A-3}$$

where $\mathbf{v} \cdot \bigtriangledown$ is called a convection term. Substituting equations A-2 and A-3 into Newton's second law gives the final result

$$\begin{aligned} V \bigtriangledown p &= m(\frac{\partial \mathbf{v}}{\partial t} + (\mathbf{v} \cdot \bigtriangledown)\mathbf{v}) \\ \rightarrow \bigtriangledown p &= \rho(\frac{\partial \mathbf{v}}{\partial t} + (\mathbf{v} \cdot \bigtriangledown)\mathbf{v}) \end{aligned} \tag{A-4}$$

In Appendix B it is demonstrated that the convection term in equation A-4 can be neglected in the seismic case.

Appendix B: Linearization of the equation of motion and the constitutive law for a plane wave

The equation of motion and the constitutive law describe the motions of the isotropic, non-viscous medium when a pressure wave propagates through. The plane-wave assumption will allow these equations to be linearized.

A linear relation between pressure and velocity for a plane-wave is written as (in 1D)

$$p = (\rho c)v \tag{B-1}$$

The term $\frac{v}{c}$ is the unitless Mach Number and gives the relation between the wave velocity and the particle velocity of the medium. Solving equation B-1 for the Mach Number yields

$$\frac{v}{c} = \frac{p}{\rho c^2} \tag{B-2}$$

In this paper, water is the medium of interest and by substituting in values for density and medium velocity of water, the equation becomes

$$\frac{v}{c} = (0.4p)10^{-9} \tag{B-3}$$

where $c = 1500m/s$ and $\rho = 1000kg/m^3$. In the seismic case, the pressure p typically $< 10^3 Pa$, making the Mach Number close to

$$\frac{v}{c} = (0.4)10^{-6} \tag{B-4}$$

which is much less than 1 (Berkhout, 1980). The fact that the Mach Number is so small makes it possible to neglect the convection term in both the equation of motion and the constitutive law. Consider first the equation of motion, and introduce the approximation

$$
\begin{aligned}
|(\mathbf{v}\cdot\bigtriangledown)\mathbf{v}| &= |v_x\frac{\partial v}{\partial x}| + |v_y\frac{\partial v}{\partial y}| + |v_z\frac{\partial v}{\partial z}| \\
&= |\frac{v_x}{c}\frac{\partial v}{\partial t}| + |\frac{v_y}{c}\frac{\partial v}{\partial t}| + |\frac{v_z}{c}\frac{\partial v}{\partial t}| << |\frac{\partial v}{\partial t}|
\end{aligned}
\tag{B-5}
$$

where the absolute value is taken since only the magnitude of the derivative is of interest. Thus, by use of equation B-5, equation A-4 in Appendix A simplifies to

$$
\bigtriangledown p = \rho\frac{\partial \mathbf{v}}{\partial t} \tag{B-6}
$$

The same analysis can also be applied to the constitutive law (equation 2.9 in the main text)

$$
\begin{aligned}
|(\mathbf{v}\cdot\bigtriangledown)p| &= |v_x\frac{\partial p}{\partial x}| + |v_y\frac{\partial p}{\partial y}| + |v_z\frac{\partial p}{\partial z}| \\
&= |\frac{v_x}{c}\frac{\partial p}{\partial t}| + |\frac{v_y}{c}\frac{\partial p}{\partial t}| + |\frac{v_z}{c}\frac{\partial p}{\partial t}| << |\frac{\partial p}{\partial t}|
\end{aligned}
\tag{B-7}
$$

simplifying equation 2.9 to

$$
\frac{\partial p}{\partial t} = -K\bigtriangledown\cdot\mathbf{v} - KQ \tag{B-8}
$$

Which is the same as equation 2.10 in the main text.

Appendix C: Sweep design and acceleration response

We start by considering a phase dependent sweep signal of the form

$$s(t) = A(t)cos[2\pi(\phi(t) + \phi_0)] \tag{C-1}$$

where $A(t)$ is the time dependent amplitude, ϕ_0 is the initial phase and $\phi(t)$ is the time dependent phase function given by (linear sweep)

$$\phi(t) = f_0 t + \frac{(f_1 - f_0)t^2}{2T} \tag{C-2}$$

where f_0 and f_1 are respectively the lowest and highest frequency of the sweep and T is the total duration for one sweep (sweep length). The signal $s(t)$ in the frequency domain can be obtained through the Fourier transform resulting in

$$S(\omega) = \int_0^T s(t)e^{(-i\omega t)}dt = \int_0^T A(t)cos[2\pi(\phi(t) + \phi_0)][cos(\omega t) - isin(\omega t)]dt \tag{C-3}$$

Through the identities $cos(a+b)cos(c) = \frac{1}{2}[cos(a+b-c) + cos(a+b+c)]$ and $-cos(a+b)sin(c) = \frac{1}{2}[sin(a+b-c) - sin(a+b+c)]$ (Kadry, 2014) equation C-3 becomes

$$\begin{aligned} S(\omega) = \int_0^T A(t)\frac{1}{2}\{&cos[2\pi(\phi(t) + \phi_0) - \omega t] + cos[2\pi(\phi(t) + \phi_0) + \omega t] + \\ &isin[2\pi(\phi(t) + \phi_0) - \omega t] - isin[2\pi(\phi(t) + \phi_0) + \omega t]\}dt \\ &= \frac{1}{2}\int_0^T A(t)[e^{i[2\pi(\phi(t)+\phi_0)-\omega t]} + e^{-i[2\pi(\phi(t)+\phi_0)+\omega t]}]dt \end{aligned} \tag{C-4}$$

With phase spectrum

$$\Phi(\omega, t) = 2\pi(\phi(t) + \phi_0) - \omega t \tag{C-5}$$

being introduced such that equation C-4 becomes

$$S(\omega) = \frac{1}{2}\int_0^T A(t)[e^{i\Phi(\omega,t)} + e^{-i\Phi(-\omega,t)}]dt \tag{C-6}$$

The original signal $s(t)$ is a real signal which means that the following relation holds $S(\omega) = S^*(-\omega)$ (Rietsch, 1977). Therefore, the signal $S(\omega)$ can be defined by positive frequencies only

$$S(\omega) = \frac{1}{2}\int_0^T A(t)e^{i\Phi(\omega,t)}dt \tag{C-7}$$

The phase function $\Phi(\omega, t)$ oscillates so rapidly compared to the amplitude function $A(t)$ that only the vicinity around its stationary points contribute to the actual signal. All other points cancel out in the integration. The stationary points are found by setting the time-derivative of the phase spectrum $\Phi(\omega, t)$ equal to 0

$$\begin{aligned} \frac{d\Phi}{dt} &= 2\pi\frac{d\phi(t)}{dt} - \omega = 0 \\ \rightarrow 2\pi(f_0 + \frac{(f_1 - f_0)t}{T}) - \omega &= 0 \end{aligned} \tag{C-8}$$

where the phase function in C-2 has been substituted in. Solving equation C-8 for t yields the stationary points t_w

$$t_w = (\frac{\omega}{2\pi} - f_0)\frac{T}{(f_1 - f_0)} \tag{C-9}$$

By substituting t_w (from equation C-9) into the phase function $\phi(t)$ gives the contributing parts of the phase:

$$\begin{aligned} \phi(t_w) &= f_0 t_w + \frac{(f_1 - f_0)t_w^2}{2T} \\ = \frac{f_0 T}{(f_1 - f_0)}(\frac{\omega}{2\pi} - f_0) + \frac{(f_1 - f_0)}{2T}[\frac{T}{(f_1 - f_0)}(\frac{\omega}{2\pi} - f_0)]^2 \\ = \frac{f_0 T}{(f_1 - f_0)}(\frac{\omega}{2\pi} - f_0) + \frac{T}{2(f_1 - f_0)}(\frac{\omega}{2\pi} - f_0)^2 \end{aligned} \tag{C-10}$$

and correspondingly for the phase spectrum (equation C-5) while assuming no initial phase ϕ_0 yields

$$\begin{aligned}\Phi(\omega,t_w) &= 2\pi\phi(t_w) - \omega t_w \\ = 2\pi[\frac{f_0T}{(f_1-f_0)}(\frac{\omega}{2\pi}-f_0) + \frac{T}{2(f_1-f_0)}(\frac{\omega}{2\pi}-f_0)^2] - \frac{\omega T}{(f_1-f_0)}(\frac{\omega}{2\pi}-f_0) \\ = \frac{\omega_0 T}{(f_1-f_0)}(\frac{\omega}{2\pi}-f_0) + \frac{T\pi}{(f_1-f_0)}(\frac{\omega}{2\pi}-f_0)^2 - \frac{\omega T}{(f_1-f_0)}(\frac{\omega}{2\pi}-f_0)\end{aligned} \tag{C-11}$$

Keep in mind that for a linear sweep, the angular frequency ω can be expressed as a linear equation $\omega = \omega_0 + \frac{(\omega_1-\omega_0)t_w}{T}$. Substitution of this expression in the last term in equation C-11 gives

$$\begin{aligned}\Phi(\omega,t_w) = \frac{\omega_0 T}{(f_1-f_0)}(\frac{\omega}{2\pi}-f_0) + \frac{T\pi}{(f_1-f_0)}(\frac{\omega}{2\pi}-f_0)^2 \\ -\frac{\omega_0 T}{(f_1-f_0)}(\frac{\omega}{2\pi}-f_0) - \frac{(\omega_1-\omega_0)t_w T}{(f_1-f_0)T}(\frac{\omega}{2\pi}-f_0) \\ = \frac{T\pi}{(f_1-f_0)}(\frac{\omega}{2\pi}-f_0)^2 - 2\pi t_w(\frac{\omega}{2\pi}-f_0) \\ = \frac{T\pi}{(f_1-f_0)}(\frac{\omega}{2\pi}-f_0)^2 - \frac{2\pi T}{(f_1-f_0)}(\frac{\omega}{2\pi}-f_0)^2 \\ = -\frac{\pi T}{(f_1-f_0)}(\frac{\omega}{2\pi}-f_0)^2\end{aligned} \tag{C-12}$$

The stationary phase solution to equation C-7 is now given as (Rietsch, 1977)

$$S(\omega) = \frac{A(t_w)}{2\sqrt{\mid \Phi''(\omega,t_w) \mid}} e^{i[2\pi(\phi(t_w)+\phi_0)-\omega t+\pi/4]} \tag{C-13}$$

where Φ'' means taking the second derivative with respect to time. Assume now that the sweep signal in equation C-1 represents the velocity of the vibrating plates. From equation C-13 it follows that the amplitude spectrum of the velocity is given as

$$\mid V(\omega) \mid = \frac{A(t_w)}{2\sqrt{\mid \Phi''(\omega,t_w) \mid}} \tag{C-14}$$

The corresponding amplitude spectrum of the acceleration is obtained by multiplication with instantaneous frequency $\omega(t)$ in equation C-14 (and a factor of i in the phase):

$$\mid a(\omega) \mid = \frac{A(t_w)\omega(t)}{2\sqrt{\mid \Phi''(\omega,t_w) \mid}} \tag{C-15}$$

A good design criterion will be to ensure a flat amplitude spectrum of the acceleration. This implies that we introduce the following constraint in equation C-15 (D being a constant)

$$\begin{aligned} D &= \frac{A(t_w)\omega(t)}{2\sqrt{\mid \Phi''(\omega,t_w) \mid}} \\ \Rightarrow \Phi''(\omega,t) &= \frac{A^2(t_w)\omega(t)^2}{4D^2} = \frac{d\omega(t)}{dt} \\ \rightarrow \frac{1}{\omega(t)^2}d\omega(t) &= \frac{A^2(t_w)}{4D^2}dt \end{aligned} \tag{C-16}$$

where the relationship $\Phi(\omega,t) = 2\pi(\phi(t)+\phi_0) - \omega t$, $\frac{d\Phi}{dt} = \frac{d}{dt}(2\pi\phi(t)) - \omega = \omega(t) - \omega$ and $\frac{d^2\Phi}{dt^2} = \frac{d\omega(t)}{dt}$ has been applied. This is a first order differential equation with solution

$$\begin{aligned} \int \frac{1}{\omega(t)^2}d\omega(t) &= \int \frac{A^2(t_w)}{4D^2}dt \\ \rightarrow -\frac{1}{\omega(t)} &= \frac{A^2(t_w)t}{4D^2} + C \end{aligned} \tag{C-17}$$

where C is the integration constant. This integral can be evaluated between two times $t = 0$ with corresponding frequency ω_1 and $t = T$ with corresponding frequency ω_2, where T is the length of the sweep. In a sweep, the frequency changes with time such that $\omega_1 \neq \omega_2$

$$\begin{aligned} -\frac{1}{\omega_1} &= C, t = 0 \\ -\frac{1}{\omega_2} = \frac{A^2(t_w)T}{4D^2} + C &= \frac{A^2(t_w)T}{4D^2} - \frac{1}{\omega_1}, t = T \\ \rightarrow \frac{A^2(t_w)}{4D^2} &= \frac{1}{T\omega_1} - \frac{1}{T\omega_2} \end{aligned} \tag{C-18}$$

Substituting $\frac{A^2(t_w)}{4D^2}$ and C into equation C-17 yields

$$\begin{aligned} -\frac{1}{\omega(t)} &= t(\frac{1}{T\omega_1} - \frac{1}{T\omega_2}) - \frac{1}{\omega_1} \\ = \frac{t(\omega_2-\omega_1)}{T\omega_1\omega_2} - \frac{T\omega_2}{T\omega_1\omega_2} &= \frac{t(\omega_2-\omega_1) - T\omega_2}{T\omega_1\omega_2} \\ \Rightarrow \omega(t) &= \frac{T\omega_1\omega_2}{T\omega_2 - t(\omega_2-\omega_1)} \end{aligned} \tag{C-19}$$

Equation C-19 describes how frequency changes with time between ω_1 and ω_2. When $t = 0$, the equation reduces to ω_1 and when $t = T$, the equation reduces to ω_2. To find

the phase function, the relation $\omega(t) = \frac{d(2\pi\phi(t))}{dt}$ can be used

$$\begin{aligned} \phi(t) &= \phi(0) + \frac{1}{2\pi}\int_0^T \omega(t)dt \\ &= \phi(0) + [\frac{T\omega_1\omega_2}{(\omega_1-\omega_2)} ln(1 + \frac{t(\omega_1-\omega_2)}{T\omega_2})]\frac{1}{2\pi} \end{aligned} \tag{C-20}$$

where $\phi(0)$ denotes the initial phase at $t = 0$ and the second term denotes how the phase will change over time. If we set $\phi(0) = 0$ and introduce a Taylor expansion of the logarithmic function to 2nd order, the phase function in equation C-20 is equal to that in equation C-2. If we again let equation C-1 represent the velocity of the vibrating plates, the phase term can be written as

$$\mathbf{v}(t) = cos(2\pi\phi(t)) \tag{C-21}$$

Substituting the expression for the phase from equation C-20 into equation C-21 yields

$$\mathbf{v}(t) = cos(2\pi\phi(0) + \frac{T\omega_1\omega_2}{(\omega_1-\omega_2)} ln(1 + \frac{t(\omega_1-\omega_2)}{T\omega_2})) \tag{C-22}$$

Taking the time derivative of equation C-22 yields the particle acceleration caused by a vibrating plate

$$\mathbf{a}(t) = \frac{d\mathbf{v}(t)}{dt} = \frac{dcos(u)}{du}\frac{du}{dt} \tag{C-23}$$

if we set $u = 2\pi\phi(0) + \frac{T\omega_1\omega_2}{(\omega_1-\omega_2)} ln(1 + \frac{t(\omega_1-\omega_2)}{T\omega_2})$ then

$$\begin{aligned} &= -sin(u)\frac{d}{dt}(2\pi\phi(0) + \frac{T\omega_1\omega_2}{(\omega_1-\omega_2)} ln(1 + \frac{t(\omega_1-\omega_2)}{T\omega_2})) \\ &= -sin(u)[\frac{T\omega_1\omega_2}{(\omega_1-\omega_2)}\frac{1}{(1+t(\omega_1-\omega_2))}(\frac{\omega_1-\omega_2}{T\omega_2})] \\ &= -sin(u)(\frac{T\omega_1\omega_2}{T\omega_2 + t(\omega_1-\omega_2)}) \\ = -sin(2\pi\phi(0) + \frac{T\omega_1\omega_2}{(\omega_1-\omega_2)} ln(1 + \frac{(\omega_1-\omega_2)t}{\omega_2 T}))&\frac{T\omega_1\omega_2}{T\omega_2 - (\omega_2-\omega_1)t} \end{aligned} \tag{C-24}$$

The acceleration obtained here (equation C-23) can be used to calculate the pressure wave field in equation 2.31 in the main text. In the same manner, the displacement caused by

a vibrating plate can be found by integrating equation C-22.

Appendix D: Difference between moving and stationary sweep data

To further investigate the difference between the stationary and moving sweep data sets, these data were subtracted from each other. For simplicity, only the middle receiver was chosen and plotted by source number (cf figure D-1).

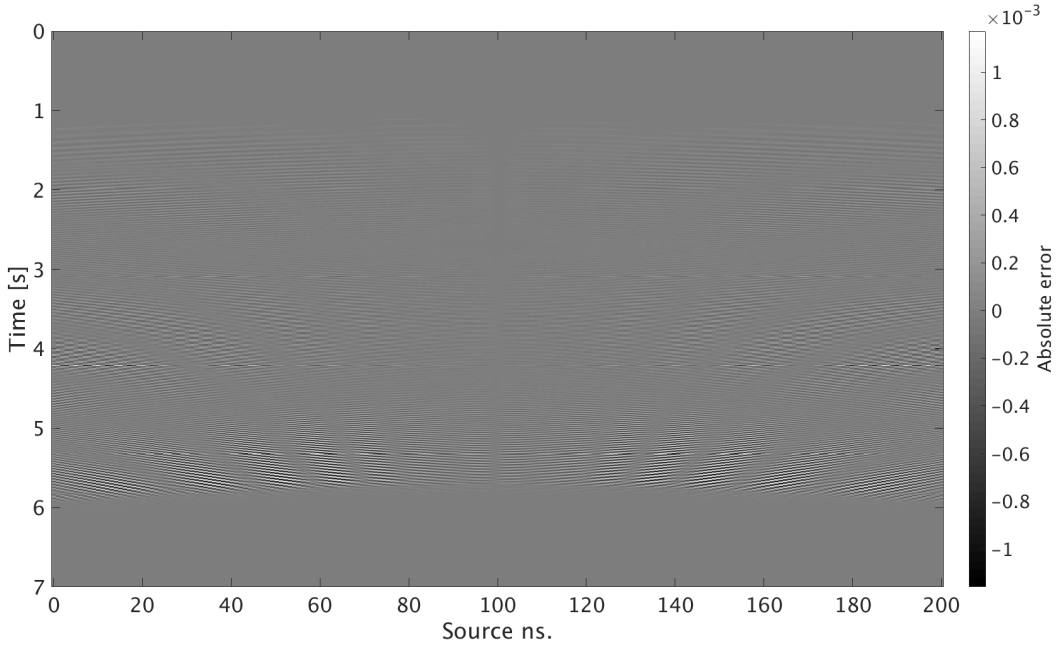

Figure D-1: Mid-receiver section of difference between moving and stationary data.

It can be observed from figure D-1 that there is a difference in data across all source numbers (except for source number 100). Since the middle receiver was chosen, the shortest propagation distance is is represented by source number 100 as this is the shot directly positioned above the diffractors. The propagation distance increases as the shot number increases or decrease away from shot number 100.

To obtain a more accurate representation of the differences in data, two Fourier transforms were applied to the data. The first one from time to frequency and the second one from space to horizontal wavenumber k_x (from TX-domain to FK-domain). Then, the ratio of amplitudes spectra between the two data sets were plotted as shown in figure D-2.

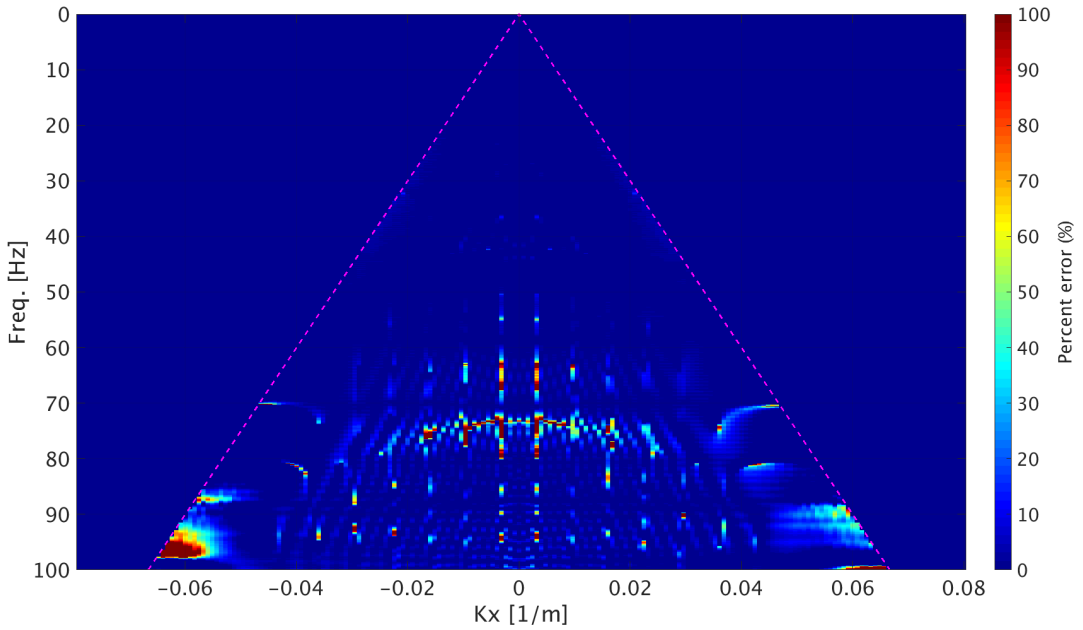

Figure D-2: Ratio in amplitude spectra between moving and stationary data sets in the FK-domain. The horizontal axis represents the horizontal wavenumber.

It can be observed from figure D-2 that there are no amplitude difference below $60Hz$, but some differences above $60Hz$ at large horizontal wavenumber (large offsets). It can be observed that some numerical errors have occurred in the process, especially in the middle of the plot. The corresponding phase spectrum of the differences in the two data sets is given in figure D-3.

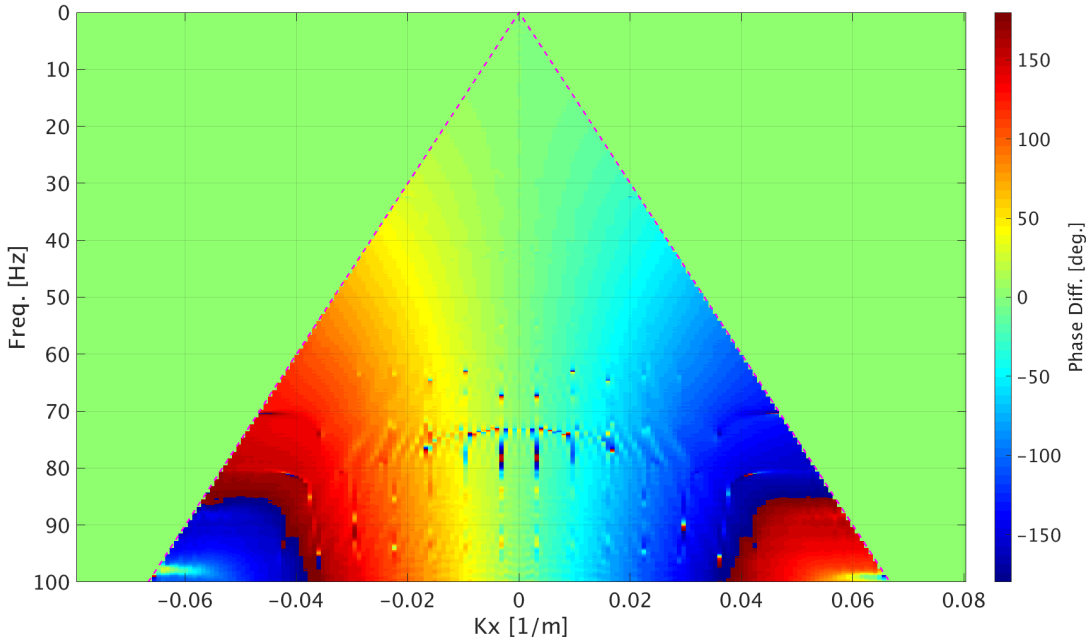

Figure D-3: Difference in phase between moving and stationary data sets in the FK-domain. The horizontal axis represents the horizontal wavenumber.

The phase spectrum in figure D-3 shows a more dramatic change than the amplitude spectrum. There is basically no phase difference at zero-offset ($k_x = 0$), but it increases with increasing k_x at the higher frequencies. Hence, the phase difference increases drastically with offset. Furthermore, figure D-3 shows that the problem with a moving source is essentially a phase correction problem which applies particularly to the large offsets. However, even if the phase errors may be significant, the corresponding amplitude errors are very low. Thus the overall effect of motion is fairly negligible in case of a standard vessel speed except for the high frequencies (above $60.70Hz$) at large offsets.

Appendix E: Accepted article to SEG2019

Marine Vibrator: Source Wavefield Modeling

Sander W. Losnedahl(PGS/UIO), Okwudili C. Orji (PGS), Leiv J. Gelius (UIO), Walter Söllner (PGS)*

Summary

Traditional marine seismic sources are facing increasingly strict regulation due to their non-negligible environmental foot print. However, marine vibrators are easy to control, are more efficient and have lower environmental foot print. Here we demonstrate source wavefield modeling for marine vibrators, discuss the source signature requirements and important processing and imaging steps.

Introduction

The marine geophysical community proactively seeks to be environmentally responsible. Low environmental footprint in terms of Sound Pressure Level (SPL) and Sound Exposure Level (SEL) especially in locations marked as "sensitive areas" is a major goal for the industry. In addition, though conventional air-gun sources can deliver low frequencies that may be used in some specialized processing (e.g. full waveform inversion), such procedures would work even better if the low frequencies could be further enhanced, which could be achieved using marine vibrators. As a result, several alternatives to conventional air-gun sources have been developed. Tenghamn and Long (2006) present a marine vibrator with a flextensional shell. Dellinger et al. (2016) present a marine vibrator that generates low frequencies. Roy et al. (2018) present a marine vibrator source capable of emitting energy from 10-100Hz.

One common feature of these sources is that the output pressure is based on the oscillation of their plates.

In this work, we present a method for modeling the output pressure wavefield for a marine vibrator that is based on stacks of oscillating plates. An example of the measured amplitude spectrum of a marine vibrator source which generates acoustic wavefield by actuating a vibrator surface to produce a volume change in the surrounding water is shown in Figure 1 (Oscarsson et al., 2019). The basic element of the source consists of two parallel plates actuated towards and away from each other. When a multitude of these elements are arranged in proximity to each other, they form a modular projector system. The full system is divided into Low Frequency (LF) and High Frequency (HF) modules. The LF module is specially designed to drive a large radiating area at small displacements and was operated from 1-45Hz while the HF module was operated from 35-100Hz for 30s. The equivalence of 5s notional was computed based on Rietsch (1977).

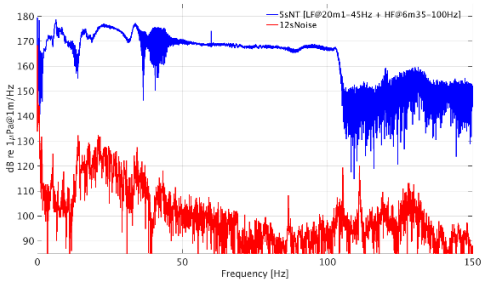

Figure 1: Amplitude spectra of the measured LF and HF sources.

Since marine vibrators are non-impulsive and are in motion during data acquisition, synthetic data was computed and imaged for stationary and moving sources in order to investigate the performance of these types of sources with respect to data acquisition, processing and imaging.

Theory

The modeling method is based on the reciprocity theorem and relates the acceleration of the plates directly to the output pressure. Hence, the required plate motion can be computed. The building element of the marine vibrator source is composed of an oscillating pair of plates in water, which enclose a volume of air under pressure. The seismic wavefield everywhere outside this volume may be derived from the motion of the vibrator plates, which leads to increasing and decreasing of the enclosed volume (see Figure 2). Inside the plates the acoustic laws may fail and this volume will be removed from the model.

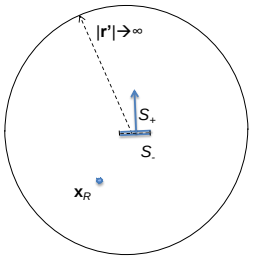

Figure 2: Single vibrator: Plate surface with normal vector across the inner surface

We start from the acoustic representation theorem. The pressure wavefield inside the model enclosed by the spherical surface as outer border and an idealized surface surrounding the oscillating plates, as inner border, is expressed for a model free of body forces by surface integrals of the free space Green's function g, the pressure p, and the gradients of these wavefields on the outer and

inner surfaces (Morse and Feshbach, 1953). By letting the outer surface go to infinity and applying Sommerfeld's radiation condition (Sommerfeld, 1949), the pressure may be written as a surface integral enclosing the plate volume:

$$p(\boldsymbol{x}_R,t) = \int_{S_+ + S_-}(g(\boldsymbol{x},\boldsymbol{x_R},t) * \nabla p\,(\boldsymbol{x},t) - \nabla g(\boldsymbol{x},\boldsymbol{x_R},t) * p(\boldsymbol{x},t))d\boldsymbol{x} \quad (1)$$

In equation 1 we have assumed that the surface surrounding the total volume that is removed is given solely by the plate surfaces S_+ and S_- (i.e., the distance between the plates is much smaller than the plate size). Defining the direction of the normal vector to point from S_- to S_+ (as indicated in Figure 1), the integral over the entire surface may be expressed as:

$$p(\boldsymbol{x}_R,t) = \int_{S_+}(g(\boldsymbol{x},\boldsymbol{x_R},t) * \nabla p\,(\boldsymbol{x},t) - \nabla g(\boldsymbol{x},\boldsymbol{x_R},t) * p(\boldsymbol{x},t))d\boldsymbol{x} - \int_{S_-}(g(\boldsymbol{x},\boldsymbol{x_R},t) * \nabla p\,(\boldsymbol{x},t) - \nabla g(\boldsymbol{x},\boldsymbol{x_R},t) * p(\boldsymbol{x},t))d\boldsymbol{x}. \quad (2)$$

So far no assumptions are made about Green's functions or wavefields on the plate surfaces. If we now assume continuity of the pressure fields across the surfaces, which is a valid assumption for thin synchronously oscillating plates separated by a very small distance, and we also impose continuity for the Green's functions and their derivatives we obtain:

$$p(\boldsymbol{x}_R,t) = \int_{S_+} g(\boldsymbol{x},\boldsymbol{x_R},t) * [\nabla p\,(\boldsymbol{x},t)]d\boldsymbol{x}. \quad (3)$$

The bracket [.] in equation 3 denotes the difference of values, in this case of the gradients of the pressure wavefield across the plate surfaces. Since an accurate measurement of the pressure gradients at the plate surfaces might be difficult, we replace the pressure gradients by particle accelerations from the equation of motion:

$$p(\boldsymbol{x}_R,t) = \rho \int_{S_+} g(\boldsymbol{x},\boldsymbol{x_R},t) * [\boldsymbol{a}\,(\boldsymbol{x},t)]d\boldsymbol{x}. \quad (4)$$

Equation 4 is our final expression for calculating the emitted pressure wavefield from a surface integral of the free space Green's function and the particle acceleration difference across the surfaces of one pair of synchronously oscillating plates. By using the continuity of the normal particle velocity at the plate water contact, the particle acceleration is obtained from the induced plate oscillation (Söllner and Orji, 2018). As a consequence of equation 4 the derived pressure wavefield everywhere in the model will be in phase with the acceleration of the plate oscillation.If we aim for a flat spectral farfield pressure emitted by the source, the time function of the plate motion needs to be designed such that the acceleration becomes a flat function in the frequency domain. If instead plate motion with a flat spectral behavior were generated, this would automatically lead to an emitted pressure wavefield with strongly suppressed low frequencies.

Marine Vibrator Source Wavefield

Using equation 4, the source wavefield was computed for a pair of circular vibrating plates with 0.5m radius. The source wavefield was modeled for 1-20 Hz 4s long sweeps. The output was computed for a receiver located 100m from the center of the oscillating plates. The condition of flat amplitude spectrum of the acceleration was imposed. Figure 3 show the time plot of plate motion (left panel), the plate acceleration (middle panel) and computed pressure (right panel). Figure 4 and 5 show the corresponding amplitude and phase spectra respectively. Observe that, as equation 4 suggests, the amplitude spectrum of the plate motion is proportional to $1/f^2$ since the amplitude spectrum of the plate acceleration is flat (see Figure 4). Note also from Figure 5 (top panel), that the plate motion and the acceleration are 180 degrees out of phase while the pressure and acceleration are in phase (lower panel).

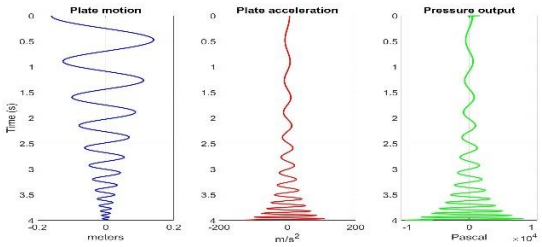

Figure 3: Time plots of the modeled source wavefield.

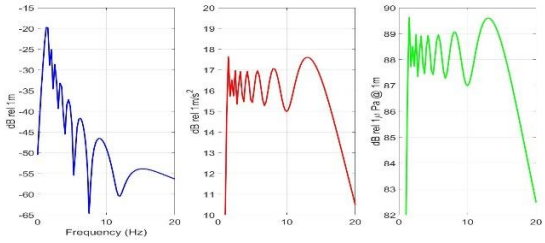

Figure 4: Amplitude spectra of the modeled source wavefield.

Source Wavefield Modeling

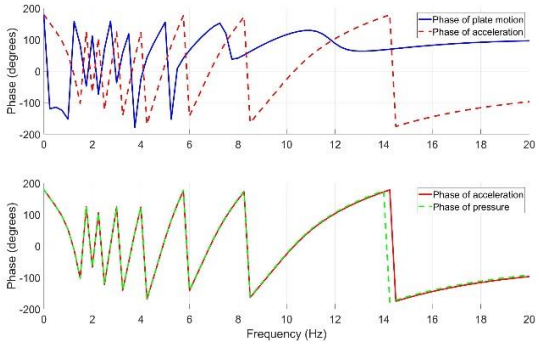

Figure 5: Phase spectra of the modeled source wavefield.

As Figure 4 suggests, much more work is needed to generate the low frequencies in comparison to higher frequencies. Hence, in order to achieve a desired constant pressure output over the entire frequency band, the source could be divided into low frequency (LF) and high frequency (HF) modules (see Figure 1).

Synthetic Data Generation and Imaging

In order to generate enough output, marine vibrator source signatures are inherently long. Unlike air-gun sources, marine vibrators are moving while generating their wavefields. Hence, the wavefields have motion effects. In order to demonstrate the effect of this motion on imaged targets, synthetic data was generated for stationary and moving sources using on 2D Finite Difference modeling (2DFD).

The data was computed using a homogenous background model consisting of water with two diffractors that are 150m apart and located at a depth of 1000m. Data was computed for a total of 200 shots for 960 receivers that were placed 490m away from the sea surface in a split-spread configuration. The source was placed 480m from the sea surface and both the shot and receiver intervals were 6.25m. The modeled source wavelet was a 5-100Hz 5s linear sweep. Two data sets were computed for a stationary source and a source moving at 2.67m/s (5.19 knots) while the receivers were stationary. To reduce artefacts from 2DFD modeling, a Perfectly Matched Layers, PML, absorbing boundary was used and the sea surface reflection was turned off.

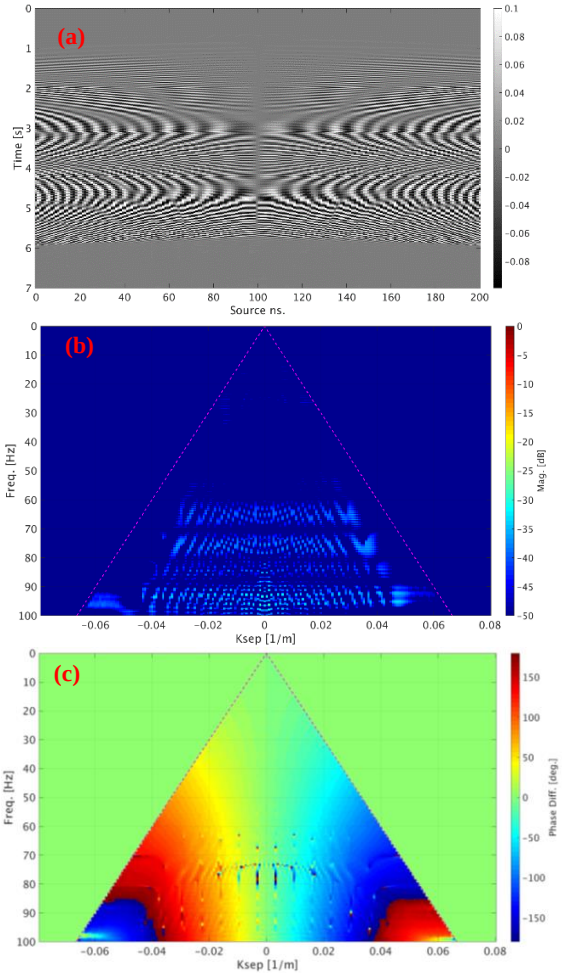

Figure 6: Common receiver gather of moving and stationary datasets scaled by 10 for visualization in TX domain (a), the amplitude ratio in FK-domain (b) and the phase difference in FK-domain (c).

Figure 6a shows a common receiver gather of the difference between the moving and the stationary source data in time and space. The amplitude ratio as shown in Figure 6b is negligible (less than about -35dB). Figure 6c shows the spectrum of the phase difference between moving and stationary sources. The plots show that the problem of a moving source is essentially a phase correction problem. Observe also that since the source is moving from left to right and passing through the top of the diffractors, when the source is located vertically above the diffractors, there is zero net difference in phase and amplitude between the two data sets (see Figure 6a & 6c) which is as expected according to Doppler effects. Moreover, there is a polarity reversal as the source passes the diffractors' locations (Figure 6a and

6c) Figure 6c shows that the phase difference increases with propagation angle which implies that the difference in the time series (Figure 6a) increases with offset. Moreover the difference in amplitude increase from lower time to higher times which is an indication that a linear up sweep was used.

In order to analyse the effect of motion in the final image, the computed data sets were cross-correlated using the pilot trace (that is the modeled source wavefield for a stationary source). This is correct for a stationary source but will introduce errors for the moving source data set (see Figure 6). Subsequently the data sets were migrated using 2D Full Finite Difference Migration, 2DFFDMIG with correlation imaging condition (Schleicher et al., 2008). Figure 7 shows depth slices of the imaged output at the target location for both data sets. The differences obtained from the two images shown in green (see Figure 7) shows that the percentage amplitude difference is at most 3.15% (or normalized root mean square (NRMS) of 2.85% NRMS). One may argue that this type of difference may be significant in the context of 4D processing. In such cases, motion could be corrected for by utilizing deconvolution techniques (Hampson and Jakubowicz, 1995; Asgedom et.al., 2019). Nevertheless, the simplified model used in the synthetic data computation and the acquistion configuration may be limitations to a broad interpretation of the results.

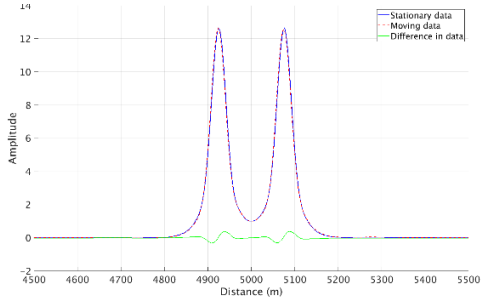

Figure 7: Imaged results for data computed for stationary source (blue), a source moving at speed of 2.67m/s (5.19 knots) (red) and the difference (green).

Discussion and Conclusions

The theory of reciprocity was used to derive an equation (equation 4) describing a continuous wavefield emitted from a point source. Such a sweep was in this case designed to have a flat amplitude spectrum (Figure 4) which is advantageous for many aspects of seismic data processing. However, the plate motion must behave in a specific manner to sustain such an amplitude spectrum across all frequencies. This causes the phase of the plate motion to be 180 degrees out of phase with the plate acceleration as seen in Figure 5. The linear sweep was used both as a stationary and moving source in finite difference modeling of a simple homogeneous model containing two diffractors. To see the effects of motion on the generated data, the stationary data set was subtracted from the moving data set. The results are shown in Figures 6a-6c. From these figures it can be seen that the amplitude differences are minor, but the phase can vary by up to 180 degrees. This phase change is due to the source moving relative to the diffractors, in contrast to a stationary source. The direction of motion of the source can be inferred from the data - with increasing shot number, the source moves closer to the diffractors and passes directly above them, then moves away from the diffractors' location. This is important as the direction of motion relative to the target determines if the pressure wavefield is compressed or dilated. Compressing the wavefield will generate higher frequencies, while dilation will generate lower frequencies. However, given the very low source speeds in marine seismic acquisition, any shift towards new frequencies by compression and dilation may not be visible as Figure 7 shows.

Significant phase differences were observed between the receiver gather of the stationary and the moving sources. Moreover, the source motion was not taken into account during processing and imaging. However, the net difference between the two migrated data sets is at most 3.15%. Nevertheless, a simplified geological model was used in this study, a further study with a more complex geology is ongoing.

Acknowledgements

The authors would like to thank PGS for permission to publish this work. A special thanks to the University of Oslo for their support.

Asgedom, E., Orji, O.C. and Söllner W., 2019, Marine Vibrator Sources: Motion Correction, Deghosting and Designature: 81st Conference and Exhibition, Extended Abstracts

Dellinger, J., Ross, A., Meaux, D., Brenders, A., Gesoff, G. and Etgen, J., 2016, Wolfspar®, an "FWI-friendly" ultralow-frequency marine seismic source: 86th Annual International Meeting, SEG, Expanded Abstracts, p. 4891 – 4895.

Hampson, G. and Jakubowicz, H., 1995, The effects of source and receiver motion on seismic data: Geophysical Prospecting, 43, p. 221-244.

Morse, P.M. and Feshbach, H., 1953, Methods of Theoretical Physics: McGraw-Hill Book Comp., Inc.

Oscarsson-Nagel, C., Söllner W., Trætten, Ø., Armstrong, B., Nams, D. and Yeatman, P., 2019, Marine Vibrator Source: Modular system with folded oscillating surface: 81th Conference and Exhibition, Extended Abstracts.

Rietsch, E., 1977, Computerized Analysis of Vibroseis Signal Similarity: Geophysical Prospecting, 25, p. 541-552.

Roy, D., Brideau C., Lawry, T., Ratliff, C. and Rekos, R., 2018, A Marine Vibrator to Meet the Joint Industry Project Specification: 88th SEG Technical Program, Expanded Abstracts, 97-101.

Schleicher, J., Costa C. J. and Novais, A., 2008, A comparison of imaging condition for wave-equation shot-profile migration: Geophysics, Vol. 73, No. 6, p. S129-S227.

Sommerfeld, A., 1949, Partial differential equations in physics: Academic Press Inc.

Söllner W. and Orji O.C., 2018, Marine vibrator source acceleration and pressure. US Patent Application Publication, Pub. No. US2018/0052245 A1

Tenghamn, R. and Long, A., 2006, PGS shows off electrical marine vibrator to capture 'alternative' seismic source market: First Break, 24, 33-36.